

Copyright
by
Swarnal Borthakur
2005

**The Dissertation Committee for Swarnal Borthakur Certifies that this is the
approved version of the following dissertation:**

**The Effects of Post-Ash Cleaning and Chemical Treatments on
the Dielectric Properties and Reliability of Cu/low- κ Interconnect
Structures**

Committee:

Paul S. Ho, Supervisor

Jack C. Lee

Arumugam Manthiram

Llewellyn K. Rabenberg

Jeffrey T. Wetzel

**The Effects of Post-Ash Cleaning and Chemical Treatments on
the Dielectric Properties and Reliability of Cu/low- κ Interconnect
Structures**

by

Swarnal Borthakur, B.E.; M.S.E.

Dissertation

Presented to the Faculty of the Graduate School of

The University of Texas at Austin

in Partial Fulfillment

of the Requirements

for the Degree of

Doctor of Philosophy

The University of Texas at Austin

August, 2005

Dedication

To my parents

Acknowledgements

I would like to acknowledge my research advisor Professor Paul S. Ho. I want to thank him for giving me the opportunity to work under his guidance and also for his advice, encouragement and support.

I would also like to thank Dr. Jeff Wetzel for his support and guidance and for providing me with samples by which I could complete my research. This work would not have been completed without his support. I would also like to thank him for agreeing to serve as a member of my dissertation committee.

I would like to thank Dr. Jack C. Lee, Dr. Arumugam Manthiram and Dr. Llewellyn Rabenberg for agreeing to serve as a member of my dissertation committee.

I would like to thank Dr. Greg Book for allowing me the opportunity to work as an intern in Sematech and would also like to thank him for his advice and friendship. I would like to thank Dr. Andreas Knorr for allowing me to continue my internship in Sematech and also for his help, advice and support.

I would like to thank Dr. Sri Satyanarayana for her help and support with samples and fruitful discussions. I would also like to thank Dr. Bernd Kastenmeier, Dr. Youfan Liu and Dr. Sanjit Das for the many interesting discussions and helpful guidance.

I would also like to thank Dr. Dorel Toma at Tokyo Electron Limited and Mr. Scott Cummings at Dow Chemical for their support in providing samples.

I would like to thank Dr. Chadwin Young, Kenneth Matthews, Glen Ross and Shashikant Patel for their help and friendship.

I would also like to thank all my colleagues at our research lab for their friendship and help. A special thanks to Joann Smith, R. Scott Smith and Matthias Kraatz.

Finally, I would like to thank my parents, brother and sister for their understanding, support and encouragement.

The Effects of Post-Ash Cleaning and Chemical Treatments on the Dielectric Properties and Reliability of Cu/low- κ Interconnect Structures

Publication No. _____

Swarnal Borthakur, Ph.D.

The University of Texas at Austin, 2005

Supervisor: Paul S. Ho

As IC devices continue to shrink, the interconnect delay dominates over the gate delay in the circuit. This has been the primary motivating factor for the industry's move towards copper and low- κ interconnects. One of the obstacles in implementing a porous low- κ material in a dual damascene structure is the degradation in its dielectric properties due to etching and ashing processes. These processes deplete the carbon from the trench interfaces and increase the hydroxyl content in the dielectric. As a result, the dielectric constant increases and the leakage and reliability characteristics degrade. The electrical characteristics and reliability of a low- κ dielectric with different pore-size and distribution was studied. Due to the difference in pore size and distribution, the interfacial roughness is higher for the material with larger pore-size. This leads to higher

defect density which causes higher leakage and degraded reliability characteristics. A low- κ material with smaller pore size and tighter distribution of pores will give better reliability characteristics. FTIR analysis of blanket MSQ-type low- κ films shows that etching and ashing processes change the molecular structure by breaking the cage configuration of the Si-O molecules and forming more network Si-O bonds. The etching and ashing processes also increase the hydroxyl content of the dielectric and consequently make the surface more hydrophilic. The analysis shows that a chemical treatment with hexamethyldisilazane (HMDS) vapor restores the carbon content of the film to an extent and reduces the hydroxyl content. This repair of the damage and partial restoration of the κ value leads to better reliability characteristics. Post-ash thermo-chemical treatments were performed in Damascene Cu/low- κ structures. An HMDS vapor treatment, followed by an annealing, was found to recover the carbon content and reduce the hydroxyl content. Such a post-ash thermo-chemical treatment also improves the breakdown and reliability characteristics. HMDS followed by an anneal treatment successfully reduces the capacitance, and as a result the effective κ , by about 3%. This decrease will become more significant as κ values continue to be lowered. The trench side-wall interfacial defect density is reduced by a factor of about 5 and the reliability lifetime is improved by a factor of about 9. Post ash chemical treatments are a useful process step that can improve the reliability of the Cu/low- κ structure and also help in achieving the effective κ target.

Table of Contents

Acknowledgements	v
Table of Contents	ix
List of Tables	xii
List of Figures	xiii
Chapter 1: Introduction	1
Chapter 2: Dielectric Leakage and Breakdown	4
2.1 Dielectric Material	4
2.2 Dielectric Breakdown	7
2.3 Dielectric Leakage	8
2.4 Time-Dependent-Dielectric-Breakdown	13
2.5 Weibull Statistics	17
2.6 Cu/Low- κ Dual Damascene Structure	18
2.7 Low- κ Leakage and Reliability	20
Chapter 3: Conduction Mechanisms of Low- κ Dielectrics	23
3.1 Samples and Experimental setup	23
3.2 Silicon Dioxide	24
3.3 Polymeric Dielectric (SiLK TM)	28
3.4 MSQ type Dielectric (JSR)	32
3.5 Ramp Voltage Breakdown	36
3.6 Discussion	40
Chapter 4: Effect of Pore Size and Distribution on Electrical Characteristics of Blanket low- κ Films	50
4.1 Samples and Experimental setup	50
4.2 Electrical Characteristics	53
4.2.1 Dielectric Constant	53

4.2.2 Ramp Voltage Breakdown	53
4.2.3 Conduction Mechanism.....	55
4.2.4 Time dependent dielectric breakdown	57
4.3 Spectral Analysis.....	66
4.4 Cross-sectional SEM.....	67
4.5 Atomic Force Microscopy.....	70
4.6 Estimation of Roughness and Defect Density.....	73
4.7 Discussion	80
Chapter 5: Processing Effects on Blanket Low- κ Films	83
5.1 Samples and Experimental setup.....	83
5.2 Electrical Characterization	86
5.3 FTIR Analysis	89
5.4 Effect of Moisture	95
5.5 Discussion	102
Chapter 6: Processing Effects on Damascene Cu/low- κ Structure	104
6.1 Single and Dual Damascene Test Structures.....	104
6.2 Cleaning Processes.....	108
6.2.1 Liquid Cleaning.....	108
6.2.2 Super Critical CO ₂ Cleaning	110
6.3 Post Ash Processes.....	116
6.3.1 Chemical Treatments.....	116
6.3.2 Low Temperature Reliability	125
6.3.3 High Temperature Reliability.....	129
6.3.4 Estimation of Interfacial Defect Density.....	138
6.3.5 Analysis of the Charge-to-Breakdown.....	140
6.3.6 Failure Analysis.....	145
6.3.7 Discussion	147

Chapter 7: Conclusions and Suggestions for Future Work.....	149
References	151
Vita	157

List of Tables

Table 3.1	Tunneling barrier height and effective mass at 25°C as reported in the literature for SiO ₂	28
Table 3.2	Electron mobility in polymers at RT from literature.....	35
Table 3.3	A summary of barrier heights shows that the Schottky barrier height is similar for the low-κ dielectrics.....	38
Table 4.1	Dielectric constant values of SiLK™ films	53
Table 4.2	Ohmic activation energies and Frenkel-Poole barrier heights for SiLK™ films shows that the energies and barrier heights are similar for all the porous versions, which indicates that the conduction mechanism is similar irrespective of the pore-size or distribution	56
Table 4.3	Field acceleration parameters for all four films	65
Table 4.4	Activation energies for all four films	65
Table 4.5	AFM surface roughness in Å for SiLK™ films shows that SiLK™ V.9 is twice as rougher than the other porous films	70
Table 5.1	Experimental split of thermo-chemical processes.....	85
Table 6.1	Split information of different liquid cleans	109
Table 6.2	Split information for the SCCO2 experiment	111
Table 6.3	Activation energies and field acceleration parameters for all three splits are similar, which shows that the breakdown mechanism is similar	134

List of Figures

Figure 1.1	Effective κ value rapidly increases with decreasing line-widths assuming a constant side-wall damage of 10nm	2
Figure 2.1	Frequency dependence of dielectric constant shows the drop in κ value at high gigahertz frequencies	6
Figure 2.2	Schottky emission schematic shows the barrier height (ϕ_B) for electron emission	9
Figure 2.3	Frenkel-Poole emission schematic shows the barrier height (ϕ_B) for emission from an interfacial trap state	10
Figure 2.4	Direct and Fowler-Nordheim tunneling schematic shows electrons tunneling through the dielectric at high electric fields	11
Figure 2.5	Current versus time plot shows an initial decrease in current followed by a steady state and final breakdown	14
Figure 2.6	Bathtub curve of lifetime shows the early failure, useful life and the wear-out stage	18
Figure 2.7	Schematic diagram of the via-first Dual Damascene process	19
Figure 3.1	Schematic of test structure used for electrical measurements	24
Figure 3.2	JE plot for oxide shows tunneling at high fields and Schottky at high temperatures	25
Figure 3.3	Schottky conduction mechanism fit for oxide	26
Figure 3.4	Tunneling conduction mechanism fit for oxide	26

Figure 3.5	Barrier height calculated from tunneling fit shows that the barrier height is independent of temperatures except at high temperatures when Schottky emission contributes to the total current.....	27
Figure 3.6	Barrier height calculated from tunneling and Schottky fit shows that the barrier height decreases with increasing effective mass for the tunneling leakage.....	27
Figure 3.7	JE plot for p-SiLK TM shows Frenkel-Poole leakage at low temperatures and high fields and Schottky leakage at high temperatures	29
Figure 3.8	Schottky fit for p-SiLK TM	30
Figure 3.9	Frenkel-Poole fit for p-SiLK TM	30
Figure 3.10	Barrier height calculated from Schottky and Frenkel-Poole fit shows that the Frenkel-Poole barrier height is lower than the Schottky barrier height	31
Figure 3.11	Barrier height calculated from Schottky fit shows that the barrier height is independent of the effective mass	31
Figure 3.12	JE plot for JSR shows Ohmic leakage at low temperatures and low fields and SCL leakage at low temperature and high fields. There is also Schottky leakage at high temperatures and current saturation at higher electric fields	33
Figure 3.13	Space-charge-limited fit for JSR	34
Figure 3.14	Schottky fit for JSR	34

Figure 3.15	Electron mobility versus $1000/T$ calculated from SCL fit for JSR shows an exponential dependence except for 295°C where there is Schottky contribution to the total leakage	35
Figure 3.16	Temperature dependence of RVB for oxide shows lower breakdown field at higher temperatures	36
Figure 3.17	Temperature dependence of RVB for p-SiLK TM shows lower breakdown field at higher temperatures	37
Figure 3.18	Temperature dependence of RVB for JSR shows lower breakdown field at higher temperatures	37
Figure 3.19	Temperature dependence of RVB shows lower breakdown field at higher temperatures for the three dielectrics and breakdown fields is higher for oxide than JSR which is higher than p-SiLK TM	38
Figure 3.20	Schematic of postulated chemical bonds at the interface of JSR and SiO ₂	43
Figure 3.21	Chemical structure of p-SiLK TM shows a cross-linked polyphenylene system	44
Figure 3.22	Bond strengths versus the dielectric stack shows the possible interfacial bonds for the three dielectrics	44
Figure 3.23	Leakage current in a damascene structure is fitted to a Frenkel-Poole conduction mechanism.....	46

Figure 3.24	Breakdown field versus the bond strength shows that the carbon depleted interfaces of Damascene structures cause weak bonds which reduces the breakdown fields	47
Figure 3.25	Lifetime of JSR and p-SiLK™ for a Damascene structure of 0.5μm pitch shows that the lifetime of JSR is about 100 times more than p-SiLK™	48
Figure 3.26	Leakage current for three different low-κ materials in a Damascene structure shows the conduction behavior of different dielectrics	49
Figure 4.1	Pore size and distribution of porous SiLK™ resins shows that SiLK™-Y has the smallest pore-size and tightest distribution and SiLK™ -V.9 has the largest pore-size and widest distribution.....	51
Figure 4.2	Schematic of test structure used for electrical tests.....	52
Figure 4.3	Representative current versus time plot showing hard breakdown..	52
Figure 4.4	JE plot for SiLK™ films shows that there is Frenkel-Poole leakage at high fields.....	54
Figure 4.5	RVB for SiLK™ films shows that SiLK™-Y has a higher breakdown field compared to the other porous films.....	54
Figure 4.6	Frenkel-Poole fit at RT for SiLK™ films	57
Figure 4.7	Weibull distribution of lifetime for SiLK™-D shows higher lifetime for lower electric fields	60
Figure 4.8	Weibull distribution of lifetime for SiLK™-V.9 shows higher lifetime for lower electric fields	60

Figure 4.9	Weibull distribution of lifetime for SiLK TM -U shows higher lifetime for lower electric fields	61
Figure 4.10	Weibull distribution of lifetime for SiLK TM -Y shows higher lifetime for lower electric fields	61
Figure 4.11	Time-to-fail versus electric field at 300°C for all four films shows that SiLK TM -Y has a higher lifetime compared to the other porous films.....	62
Figure 4.12	Time-to-fail versus 1000/T at 3.3MV/cm for all four films shows that SiLK TM -Y has a higher lifetime compared to the other porous films.....	62
Figure 4.13	Time-to-fail versus electric field for SiLK TM -D shows that higher temperatures gives lower lifetimes.....	63
Figure 4.14	Time-to-fail versus electric field for SiLK TM -Y shows that higher temperatures gives lower lifetimes.....	63
Figure 4.15	Activation energy versus electric field for all four films shows that SiLK TM -Y has slightly higher activation energies compared to the other porous films.....	64
Figure 4.16	Field acceleration parameter versus 1000/T for all four films shows that SiLK TM -V.9 has slightly lower acceleration parameters compared to the other porous films	64
Figure 4.17	FTIR absorbance spectra for SiLK TM films shows the typical benzene ring as well as other organic bond signatures	67
Figure 4.18	SEM micrograph of SiLK TM -D shows a dense film	68

Figure 4.19	SEM micrograph of SiLK TM -V.9 shows a film with interfacial roughness and pores of large sizes	68
Figure 4.20	SEM micrograph of SiLK TM -U does not show any large pores.....	69
Figure 4.21	SEM micrograph of SiLK TM -Y does not show any large pores.....	69
Figure 4.22	AFM micrograph of SiLK TM -D.....	71
Figure 4.23	AFM micrograph of SiLK TM -U.....	71
Figure 4.24	AFM micrograph of SiLK TM -Y.....	72
Figure 4.25	AFM micrograph of SiLK TM -V.9.....	72
Figure 4.26	Schematic of interfacial roughness showing the intensified electric field (E') due to the rough interface	73
Figure 4.27	Time-to-fail versus the measured roughness for the SiLK TM films shows that the lifetime is lower for higher roughness.....	74
Figure 4.28	Measured roughness versus the calculated roughness shows that the roughness will have to be about 100 times greater than the calculated value to increase the electric field to a value large enough to explain the difference in lifetimes	75
Figure 4.29	Percentile plot of Qbd for SiLK TM films shows that the SiLK TM -V.9 films have a lower Qbd compared to the other porous films	77
Figure 4.30	Qbd versus tbd for SiLK TM films shows that the SiLK TM -V.9 film has lower Qbd and lower tbd compared to the other porous SiLK TM films	77
Figure 4.31	Defect density and roughness for SiLK TM films shows that the defect density increases for a rougher film	79

Figure 5.1	Schematic of test structure for electrical tests	84
Figure 5.2	Dielectric constant of the different treatments shows the increase in κ value due to etching and ashing and the recovery of κ value by the various surface treatments	86
Figure 5.3	Typical leakage currents for the different treatments shows the increase in leakage due to the etching and ashing and the recovery of the leakage by the surface treatments	87
Figure 5.4	Leakage current at 0.1MV/cm for different treatments shows the increase in leakage due to the etching and ashing and the recovery of the leakage by the surface treatments	88
Figure 5.5	Leakage current at 1.0MV/cm for different treatments shows the increase in leakage due to the etching and ashing and the recovery of the leakage by the surface treatments	88
Figure 5.6	Schematic of Si-O-Si bond angle shows the bond angle between Si-O-Si could range from 120° to 180°	89
Figure 5.7	Gaussian peak analysis of unetched samples shows the cage, network and sub-oxide peak areas	91
Figure 5.8	Gaussian peak analysis of etched sample shows the cage, network and sub-oxide peak areas. There is a higher percentage of network peaks compared to the unetched samples	92

Figure 5.9	Deconvoluted peak areas versus the κ value shows that the cage and sub-oxide decreases and the network increases after the initial etching of the samples. The chemical treatment increases the sub-oxide peak.....	93
Figure 5.10	Deconvoluted peak areas versus the treatment of the films shows that the etching and ashing decreases the cage and increases the network area. The chemical treatments increases the sub-oxide and Si-CH ₃ area to an extent	94
Figure 5.11	Deconvoluted hydroxyl peak areas and κ values versus the treatment of the films shows that the κ value follows the hydroxyl content trend	95
Figure 5.12	Percent change in κ value versus the percent change in hydroxyl bonds shows that the etching and ashing increased the κ value and the hydroxyl content and the chemical treatments reduce the hydroxyl content and recover the κ value to an extent.....	96
Figure 5.13	Schematic of postulated hydroxyl bonding at the low- κ surface	97
Figure 5.14	Schematic of a capacitance modeling shows the effective hydroxyl thickness at the surface	98
Figure 5.15	Effective OH thickness versus the κ value shows that a chemical treatment reduces the amount of hydroxyl bonds	99
Figure 5.16	Concentration of hydroxyl bonds versus κ value shows that the κ value can be co-related to the concentration of hydroxyl bonds in the dielectric	101

Figure 5.17	Fractional change in κ and hydroxyl bonds with respect to the etched sample shows that a chemical treatment recovers the κ value to an extent.....	102
Figure 6.1	Schematic of a single Damascene test structure process.....	106
Figure 6.2	Schematic diagram of post-ash chemical treatment on a metal 1 trench and blanket low- κ dielectric film shows the sidewall damage layer	107
Figure 6.3	Breakdown and capacitance values for different cleans shows that the various cleans increase the capacitance slightly and decreases the breakdown field.....	109
Figure 6.4	Capacitance and breakdown field versus the cleaning treatments shows the improvement due to SCCO ₂ cleaning.....	112
Figure 6.5	Weibull distribution of the TTF at 1.8MV/cm shows that the SCCO ₂ processes, with the exception of EtOH, improve the lifetime slightly	113
Figure 6.6	Lifetime versus the electric field for the various splits shows that the SCCO ₂ processes improve the lifetime slightly.....	115
Figure 6.7	TEM/EELS without post-ash treatment shows the carbon depletion	118
Figure 6.8	TEM/EELS after post-ash treatment shows the carbon recovery ..	118
Figure 6.9	Effective κ value rapidly increases with decreasing line-widths assuming a constant side-wall damage of 10nm	119

Figure 6.10	Distribution of capacitance for all treatments shows that the HMDS followed by an anneal treatment decreases by capacitance by about 3%	121
Figure 6.11	Capacitance and breakdown fields for all treatments shows that the thermo-chemical treatments decrease the capacitance and increase the breakdown field.....	121
Figure 6.12	Pitch dependence of breakdown fields shows that the breakdown field decreases for smaller pitches	122
Figure 6.13	Schematic of capacitance modeling shows the effective side-wall damage layers.....	123
Figure 6.14	Plot of $1/C$ versus $(S-2t)$ for the untreated control sample.....	124
Figure 6.15	Plot of $1/C$ versus $(S-2t)$ for the HMDS followed by an anneal treatment shows that the sidewall capacitance has decreased ($1/C$ increases).....	124
Figure 6.16	Breakdown field for all three treatments versus the capacitor area shows that the breakdown field is smaller for larger areas and it is higher for the HMDS followed by an anneal treatment	126
Figure 6.17	Weibull fit for the control sample shows that higher fields gives lower lifetimes.....	127
Figure 6.18	Weibull fit for the HMDS post ash treatment shows that higher fields gives lower lifetimes	127
Figure 6.19	Weibull fit for the HMDS followed by an anneal post ash treatment shows that higher fields gives lower lifetimes	128

Figure 6.20	Lifetime at 63% Weibull fit versus the electric field shows that the HMDS followed by an anneal treatment gives higher lifetimes	129
Figure 6.21	Breakdown field for all three splits shows that the breakdown field is smaller for larger areas and it is higher for the HMDS followed by an anneal treatment	130
Figure 6.22	Weibull fits for the control sample at three temperatures shows that lifetimes decrease with increasing temperatures	131
Figure 6.23	Weibull plots for the HMDS treated sample at three temperatures shows that lifetimes decrease with increasing temperatures	132
Figure 6.24	Weibull plots for the HMDS followed by an anneal sample for three temperatures shows that lifetimes decrease with increasing temperatures	133
Figure 6.25	Lifetimes are plotted versus the electric field to obtain the field acceleration parameters	135
Figure 6.26	Lifetimes are plotted versus $1000/T$ to determine the activation energies of the three splits	136
Figure 6.27	Lifetimes are compared among the three splits for all the three temperatures. The HMDS followed by an anneal treatment has higher lifetimes	137
Figure 6.28	Delta function fit shows a poor fit for the control sample	139

Figure 6.29	Exponential function fit shows a good fit for both samples and shows that the HMDS followed by an anneal treatment reduces the defect density by a factor of about 5	140
Figure 6.30	10x10 grid representing a trench dielectric with percolation from one side to the other	142
Figure 6.31	Distribution of the additional cells required for percolation shows that the additional cells required for percolation decreases with increasing initial defects.....	142
Figure 6.32	Qbd versus TTF for all three splits shows that the HMDS followed by an anneal treatment has higher lifetimes and higher Qbd.....	143
Figure 6.33	Qbd and TTF versus the electric field show that both Qbd and TTF decrease with increasing electric field but TTF has an exponential dependence whereas Qbd does not.....	144
Figure 6.34	Cross-sectional SEM of TDDB failure site show delamination and copper penetration at the interface	145

Chapter 1: Introduction

As IC devices continue to shrink, the interconnect delay dominates over the gate delay in the circuit. This has been the primary motivating factor for the industry's move towards copper interconnects with low dielectric constant (low κ) materials. The implementation of copper and low- κ interconnects reduces the RC delay, power dissipation, cross-talk noise and the number of metal levels. According to ITRS roadmap an effective κ between 2.3 and 2.7 will be required for the 65 nm node by 2007. In that case, the bulk κ value of the material must be below 2.1. Hence there is an urgency to qualify a porous low- κ material. One of the obstacles in implementing a porous low- κ material in a dual damascene scheme is the degradation in its dielectric properties due to etching and ashing processes. Etching and ashing processes damage the trench sidewall. Various studies have shown that this leads to higher k-value. Mor (2002), Clark (2003) and Colburn (2004) showed that an etching and ashing increases the silanol content in the low- κ dielectric and makes it more hydrophilic, which leads to higher k-value. The authors have suggested that chemical treatments be used to restore the hydrophobicity of the dielectric, which will also reduce the k-value. As line widths continue to shrink, the trench sidewall damage layer remains the same because the etching and ashing processes are directional. Thus, the damaging effect becomes more critical as line widths shrink. Fig 1.1 illustrates this effect. Iacopi (2004) showed that the sidewall damage is responsible for the degradation of leakage and breakdown as the line widths become smaller.

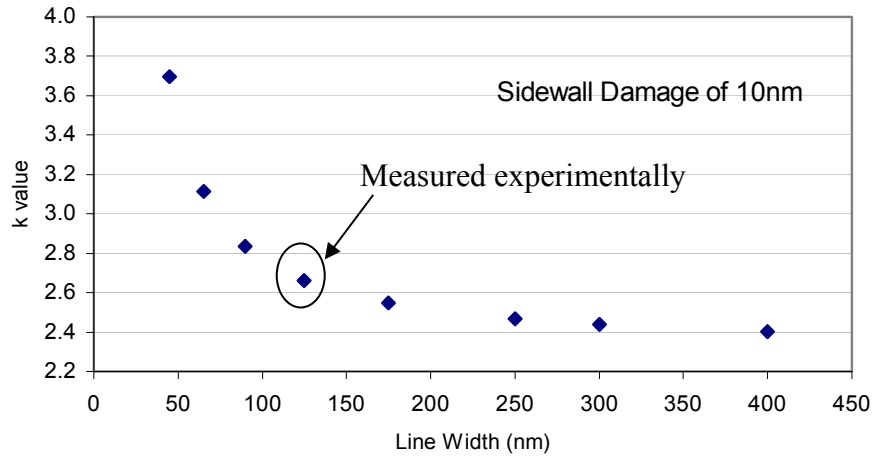


Figure 1.1 Effective κ value rapidly increases with decreasing line-widths assuming a constant side-wall damage of 10 nm

The purpose of this study is threefold: first, to understand the conduction mechanism in different porous low- κ films and how that will affect the reliability, second, to understand the effect of pore size and distribution on the reliability characteristics of porous low- κ blanket films and third, to evaluate and understand the correlation of compositional changes in the low- κ dielectric material, due to post-ash cleaning and chemical treatments, to the dielectric properties and reliability of Cu/low- κ damascene structures. A proper understanding of the effects of composition on the dielectric properties and reliability of Cu/low- κ structures will be beneficial for future reliability improvement and k-value recovery processes. To accomplish these tasks, electrical characterization and reliability tests were performed on porous low- κ blanket films as well as Cu/low- κ damascene structures.

This manuscript is divided into five main parts. In Chapter 2, conduction mechanism and theories of dielectric breakdown will be presented. A review of current research activities will also be presented. In Chapter 3, the conduction mechanisms of SiO₂, methyl-silsesquioxane (MSQ) type and polymeric type of low- κ materials will be analyzed. In Chapter 4, the effects of pore size and distribution on the dielectric properties and reliability of a porous low- κ material will be analyzed. In Chapter 5, the effects of post-ash processing on the chemical structure of porous low- κ blanket films will be analyzed by FTIR spectroscopy. In Chapter 6, the effects of post-ash cleaning and chemical treatments will be analyzed, in terms of dielectric properties and reliability, for Cu/low- κ damascene structures. Finally, conclusions and suggestions for future work will be given in Chapter 7.

Chapter 2: Dielectric Leakage and Breakdown

In this chapter dielectric breakdown theories and conduction mechanisms will be discussed. A literature survey will be presented regarding leakage, reliability of Cu/low- κ structures and the effects of processing on the electrical and material characteristics of low- κ materials.

2.1 DIELECTRIC MATERIAL

Energy bands of any given material are empty, partially filled or completely filled. The electrons in the outermost shell (valence electrons) are of primary significance because they are loosely bound and can contribute to electrical conduction. There are three types of materials in terms of the position of their energy bands; they are insulators, semiconductors and conductors.

When an electric field is applied to a conductor, electrons can easily jump to adjacent unoccupied states creating an electric current. The overlapping bands in the case of a conductor create favorable conditions for electrons to jump from an occupied state to an unoccupied state. In an insulator there are forbidden bands and the energy band gap prevents conduction in the presence of an electric field. The band gap in a semiconductor is not as large as that of an insulator. Hence it can conduct current when it obtains an appropriate amount of energy.

An insulator material that becomes electrically polarized in the presence of an electric field is known as a dielectric material. Dielectric materials can store energy and are used in capacitors. The polarization may be caused due to induced dipole moments or due to permanent dipoles aligning themselves parallel to the

electric field. The dipoles are created by the electrons involved in the chemical bonds. The polarization per unit volume is given by,

$$P = (\epsilon_r - 1) \epsilon_0 E$$

Where P is the polarization, E is the electric field, ϵ_r is the relative permittivity or κ value and ϵ_0 is the permittivity of free space which is 8.854×10^{-12} F/m.

The energy of the electrostatic field per unit volume is given by,

$$W = \epsilon_0 \epsilon_r E^2 / 2$$

Where W is the energy, E is the electric field, ϵ_r is the relative permittivity or κ value and ϵ_0 is the permittivity of free space which is 8.854×10^{-12} C/m².

There are four types of polarization, electronic, ionic, orientational and space charge. The total polarization is a sum of all the different types of polarization. The dielectric constant depends upon the polarization. The dielectric constant also depends upon the frequency. The frequency dependence arises because the polarization response of the material is not instantaneous. Fig 2.1 shows the frequency dependence of a material. Generally, dipoles can respond to frequencies up to the microwave range. At high frequencies, there can only be electronic vibrations. Between microwave and visible frequencies there are atomic vibrations. The dielectric constant of water molecules decreases from 78 to 60 from 1 to 10 GHz [Kaatze (1981)]. The microprocessors in use today run in the lower GHz range. At this range, water molecules can cause a substantial increase in the effective dielectric constant of a Cu/low- κ structure. In later sections, the dielectric constant is experimentally measured at 100 kHz due to instrumental

limitations. A comparison of κ values at 100 kHz is acceptable because the κ value does not change drastically until high gigahertz range.

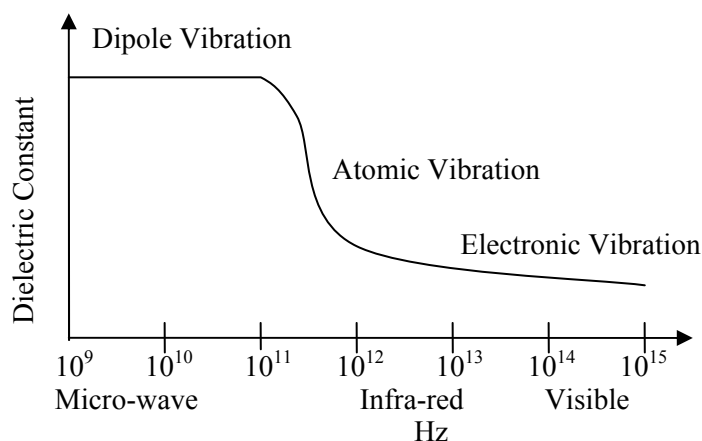


Figure 2.1 Frequency dependence of dielectric constant shows the drop in κ value at high gigahertz frequencies

The primary approach to obtaining a low- κ dielectric is to optimize the molecular structure by minimizing the polarization. This is done by synthesizing materials with low polarizability bonds, like C-C, C-H or C-F. The incorporation of low polarizability bonds must take into account the mechanical properties of the material. The glass transition temperatures (T_g), coefficient of thermal expansion (CTE), Young's Modulus, thermal conductivity and other mechanical parameters must be considered while lowering the κ value. Generally, incorporation of carbon and hydrogen bonds has a negative effect on the mechanical properties.

One approach to obtain a low- κ material is to incorporate hydro-carbon groups into the SiO_2 structure. The advantage of this method is that the SiO_2 is the backbone. Hence the strength of the material does not deteriorate too much. Hydrogen-silsesquioxane (HSQ) and methyl-silsesquioxane (MSQ) types of low- κ materials are based on the silicon dioxide structure. However, pores must be incorporated into the structure to obtain κ values of <2.5 .

Another approach is to use a completely organic material. The primary consideration for an organic material is the T_g . The T_g is the temperature above which the material becomes rubbery and no longer retains its rigidity. A high T_g and high thermal stability is a must for any low- κ material. Low moisture absorption is also a necessary requirement. SiLKTM (SiLK is a trademark of The Dow Chemical Company) is a cross-linked polyphenylene polymer, which is completely organic. Cross-linking increases the strength of the dielectric and unsaturated carbon bonds increases the thermal stability. Pores can also be incorporated in organic type of low- κ materials to reduce the κ value further.

2.2 DIELECTRIC BREAKDOWN

Even though a dielectric should not conduct current, in reality there is always a small current flowing through it. This current is a function of extrinsic parameters such as temperature and electric field and intrinsic defects and traps. Dielectric breakdown is defined as a temporary or permanent loss of dielectric properties. Temporary breakdown is also known as soft breakdown and a permanent breakdown is also known as hard breakdown. A soft breakdown occurs when there is a temporary surge in electrical current. The current returns to its

original or slightly higher stage. If the electric field is removed at this stage and reapplied, the current returns to its original or slightly higher value. However there is no permanent short. A hard breakdown is said to occur when the surge in current completely destroys the dielectric. When the electric field is removed and applied again, a permanent short is observed. All dielectrics will ultimately have a hard breakdown when a sufficiently high electric field is applied. Another type of breakdown is thermal breakdown. Thermal breakdown occurs when there is a sudden surge of carriers through the dielectric. Although breakdown may be accompanied by local heating, the mechanism of thermal breakdown is different from electrical breakdown. Thermal breakdown occurs due to joule heating and the inability of the surrounding to efficiently conduct the heat away from the dielectric. Electrical breakdown occurs due to impact ionization and avalanche breakdown.

2.3 DIELECTRIC LEAKAGE

In an ideal insulator, conductance should be zero. However, in real cases there is always a current flowing through an insulator when an external voltage is applied. The current carrying mechanism depends upon extrinsic parameters like temperature and electric field and intrinsic parameters like interfacial roughness, doping density, mobility etc. The basic conduction mechanisms in insulators are Schottky Emission, Frenkel-Poole Emission, Tunnel or Field Emission, Space-Charge-Limited, Ohmic Conduction and Ionic Conduction [Bashara (1964), Blatt (1968), O'Dwyer (1973), Sze (1981), Hamann (1988)].

In Schottky emission, current is carried by thermally excited electrons. The Schottky emission is given by the following equation,

$$J = A^* T^2 \exp \left[\frac{-q (\phi_B - \sqrt{q E / 4 \pi \epsilon})}{kT} \right]$$

Where, J is the current density, A^* is the effective Richardson's constant which is $120 \text{ A.K}^{-2}\text{cm}^{-2}$ for $m^*=m_0$, T is the temperature in K, ϕ_B is the barrier height which is the work function of the cathode, E is the electric field, ϵ is $\epsilon_0\epsilon_i$ which is the dielectric constant.

When a voltage V is applied (Fig 2.2), the Schottky barrier lowering is given by the term, $\sqrt{q E / 4 \pi \epsilon}$. A plot of $\ln(J/T^2)$ vs. \sqrt{E} gives a straight line from which the barrier height, ϕ_B can be calculated.

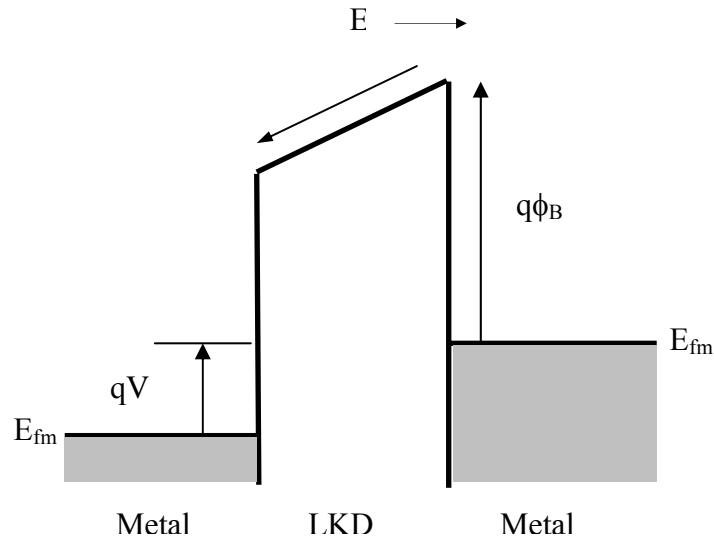


Figure 2.2 Schottky emission schematic shows the barrier height (ϕ_B) for electron emission

In Frenkel-Poole emission, current is carried by field enhanced thermally excited trapped electrons. Fig 2.3 shows a schematic of the Frenkel-Poole emission. The energy barrier for the trap level is indicated by ϕ_B . The Frenkel-Poole emission is given by the following equation,

$$J \sim E \exp [(-q(\phi_B - \sqrt{qE/\pi\epsilon}) / kT)]$$

Where, J is the current density, T is the temperature in K, ϕ_B is the barrier height which is the energy barrier for trap states, E is the electric field, ϵ is $\epsilon_0\epsilon_i$ which is the dielectric constant. The Frenkel-Poole barrier lowering is given by the term, $\sqrt{qE/\pi\epsilon}$. A plot of $\ln(J/E)$ vs. \sqrt{E} gives a straight line from which the barrier height, ϕ_B can be calculated.

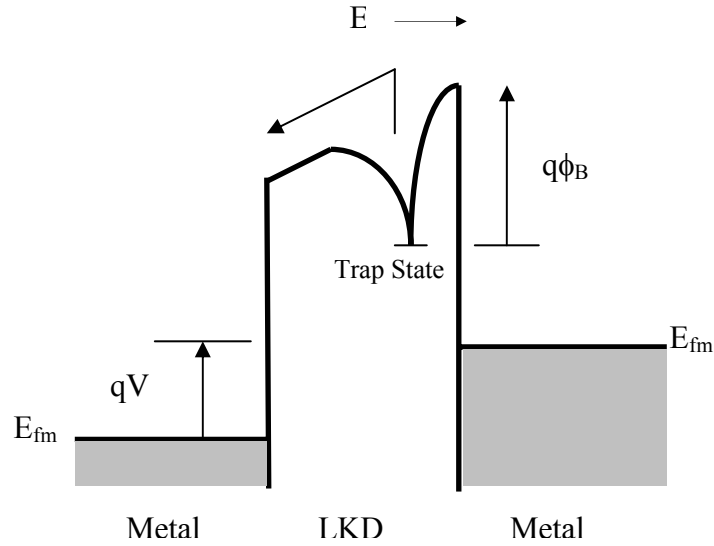


Figure 2.3 Frenkel-Poole emission schematic shows the barrier height (ϕ_B) for emission from an interfacial trap state

Tunneling or field type of emission takes place due to tunneling of electrons into the insulator conduction band. Fowler-Nordheim Tunneling emission is tunneling through the triangular barrier as shown in Fig 2.4. The tunnel or field emission is given by the following equation,

$$J = A^* E^2 \exp \left[- \frac{(4\sqrt{2m^* (q\phi_B)^{3/2}})}{(3qE (h/2\pi))} \right]$$

Where,

J is the current density, A^* is the effective Richardson's constant which is $120 \text{ A.K}^{-2}\text{cm}^{-2}$ for $m^*=m_0$, ϕ_B is the barrier height, E is the electric field, m^* is the effective mass, h is Planck's constant. A plot of $\ln(J/E^2)$ vs. $1/E$ gives a straight line from which the barrier height, ϕ_B can be calculated.

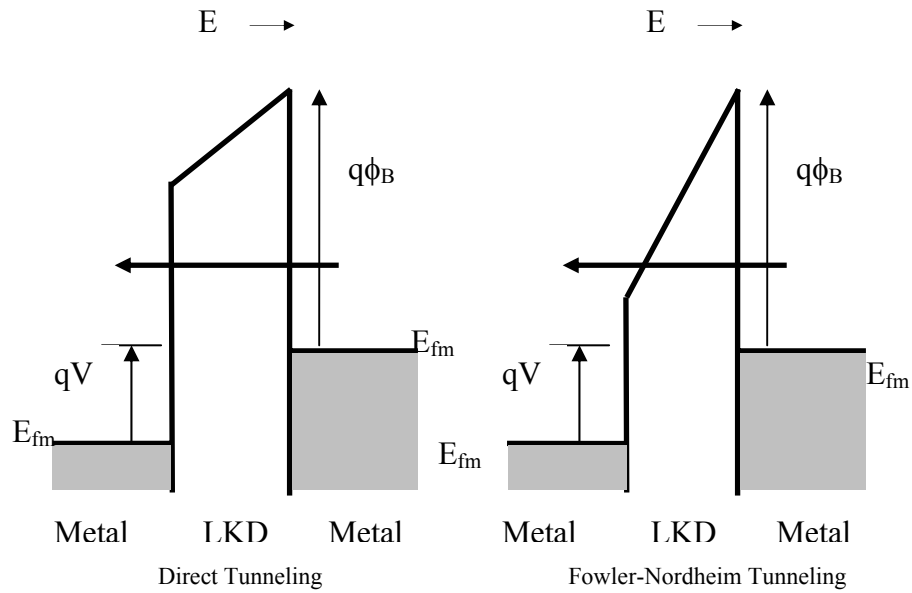


Figure 2.4 Direct and Fowler-Nordheim tunneling schematic shows electrons tunneling through the dielectric at high electric fields

Tunneling leakage occurs at high fields and is independent of temperature. Direct tunneling occurs when electrons tunnel through the dielectric directly from the cathode to the anode. Direct tunneling is affected by the thickness of the dielectric. It increases exponentially as the thickness decreases. Fowler-Nordheim type of tunneling takes place when electrons tunnel through the triangular barrier. FN tunneling depends upon the voltage across the dielectric and increases exponentially with applied voltage. Trap-assisted-tunneling occurs when electrons tunnel into traps that are present inside the dielectric and from there they tunnel into the cathode. Such type of tunneling depends upon the density of traps and the electric field.

Space-charge-limited leakage [Rose (1955), Zeller (1987), Grinberg (1989), Hare (1991)] occurs when charge is injected into the insulator where there is no compensating charge present. Space-charge-limited (SCL) leakage is bulk limited.

This type of leakage phenomenon gives the current a voltage squared dependence. The space-charge-limited leakage is given by the following equation,

$$J = (9 \epsilon \mu V^2) / (8 d^3)$$

Where, J is the current density, V is the applied voltage, ϵ is $\epsilon_0\epsilon_i$ which is the dielectric constant, d is the insulator thickness, μ is the electron mobility which is given by $\mu = \mu^* \exp [-\Delta/kT] \exp [\gamma\sqrt{E}]$. A plot of J versus V^2 will give a straight line from which mobility can be calculated. The zero-field mobility thermal activation energy can be calculated by plotting $\ln(\mu)$ vs. $1/T$.

Ohmic leakage occurs when thermally excited electrons hop from one isolated state to another. The current is exponentially dependent on temperature. Ohmic conduction is given by the equation,

$$J \sim E \exp [-\Delta E_{ae} / kT]$$

Where, J is the current density, E is the electric field, ΔE_{ae} is the activation energy for Ohmic conduction. A plot of $\ln(J/E)$ vs. $1/T$ will yield a straight line from which the activation energy for Ohmic conduction can be calculated. The difference between Frenkel-Poole and Ohmic is that F-P is electrode limited and is determined by permanent trap states while Ohmic is bulk limited and is determined by filled/unfilled electronically isolated states (vacancies, interstitials, impurities, defects) within the dielectric.

Ionic leakage occurs when thermally excited ions diffuse through the insulator. The current is exponentially dependent on temperature. Ionic conduction is given by the equation,

$$J \sim (E/T) \exp [-\Delta E_{ai} / kT]$$

Where, J is the current density, E is the electric field, ΔE_{ai} is the activation energy for ionic conduction.

2.4 TIME-DEPENDENT-DIELECTRIC-BREAKDOWN

Any dielectric will degrade and finally fail when an electric field is applied for a long enough time. The reliability of the dielectric is determined by time-dependent-dielectric-breakdown (TDDB) tests. When these tests are made at high temperatures they are also known as bias-temperature-stress (BTS) tests. The

breakdown mechanism can be intrinsic or extrinsic. The intrinsic reliability is the reliability of the dielectric in the absence of defects. Extrinsic reliability is due to extrinsic factors like processing defects. Extrinsic failures occur early and will show up as a bimodal type of failure distribution.

The reliability test consists of the application of a constant voltage stress across the dielectric and the current is monitored over time. This type of reliability test is known as time-dependent-dielectric-breakdown (TDDB). Fig 2.5 shows a typical current vs. time plot in a TDDB test. After a slight decrease, the current stabilizes to a steady state. This steady stage continues until the current starts increasing again and ultimately the dielectric breaks down.

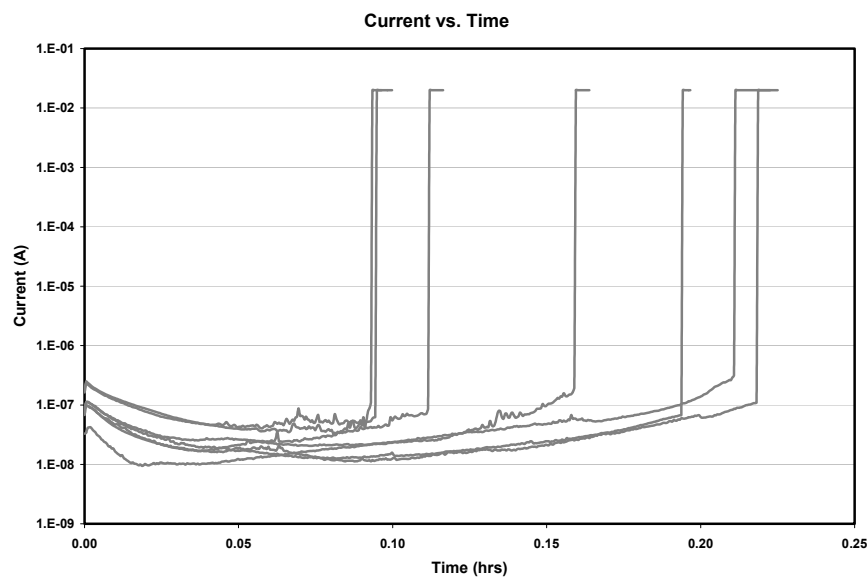


Figure 2.5 Current versus time plot shows an initial decrease in current followed by a steady state and final breakdown

TDDDB has been extensively used to study SiO₂ reliability. The failure in SiO₂ is mainly charge build-up and finally electrical and thermal runaway. The charge build-up occurs due to injection of charge as well as degradation of the oxide. The charge build-up occurs in localized areas of defects and traps. As a result, the electrical field is enhanced at a localized area, which leads to more charge build-up. This creates a feedback loop. Ultimately the electric field will exceed the breakdown field of the oxide in some localized areas. This will lead to more current flow, which will lead to electrical and thermal runaway and ultimately failure of the dielectric.

There have been various theories put forward to explain the physics of intrinsic dielectric breakdown for thin SiO₂. The two major theories are anode-hole injection (1/E model) and Thermochemical E (TCE) model.

The anode-hole injection model [Schuegraf (1994)] assumes that even though there should be no current flowing through a dielectric, in reality a tunneling current always exists. It was postulated that a fraction of the electrons entering the anode have enough energy to create a 'hot' hole, through impact ionization, that can then tunnel back into the dielectric. Most of these holes will reach the cathode but some of them will be trapped by weak or broken bonds. Such hole capture will tend to weaken the already weak bond. Therefore a positive feedback loop is created which ultimately will lead to the breakdown of the dielectric. Various modifications have been suggested to this model and there has been a great deal of literature devoted to the explanation, modification and

substantiation of this theory [Chen (1985, 1988), Lee (1988) and Schuegraf (1994)].

McPherson (1985, 2001) postulated the thermochemical E model (TCE). This model assumes that defects are generated uniformly inside the dielectric when an electric field is applied. The lattice constraint prevents the dipoles to flip simultaneously when an electric field is applied. Instead there is a time dependency to the bond breakage. The bond breakage is initiated at defects and vacancies. The strength of the bonds depends upon the ambient temperature. Since the bonds are weaker at higher temperatures, the time-to-fail (TTF) will be lower. The following equations are derived from this theory.

$$\text{TTF} = A \exp [\Delta H_o^*/kT] \exp [-\gamma(T)E]$$

$$E = \Delta H_o^* - k_B E$$

$$\gamma = (a + b/T)$$

Where, TTF is the time-to-fail (sec), ΔH_o^* or E_a is the bond strength, k_B is the Boltzmann constant, T is the temperature in Kelvin, γ is the field acceleration parameter, E is the electric field across dielectric and A , a and b are constants.

This theory can explain the breakdown both at low and high fields. However, at high fields the $1/E$ model fits the experimental data better. Therefore this theory was further modified to include the effects of hole injection at high fields. The hole trapping can act as a catalyst and accelerate the weakening of the bonds and ultimately lead to breakdown. This complementary model combines the $1/E$ and an E model into one model and tries to show that at different electric

field ranges, one of the two models will dominate. The domination depends upon the reaction rate and the slowest reaction rate ultimately will determine the TTF's dependency on the electric field.

2.5 WEIBULL STATISTICS

Electronic product lifetimes are evaluated using Weibull analysis. The failure data set is fitted to a cumulative distribution function (CDF). The CDF is given by the following equation

$$F(t) = 1 - \exp [-(TTF / \alpha)^\beta]$$

Where, α is the scale parameter, β is the shape parameter and TTF is the time-to-fail.

The slope of a plot of $\ln(-\ln(1-F(t)))$ versus $\ln(TTF)$ will give the shape parameter. The shape parameter indicates whether the failure rate is increasing, constant or decreasing [Fink (1981)]. The “bathtub curve” (Fig 2.6) can be predicted from the shape parameter. When β is less than 1.0, the product has a decreasing failure rate. This is typical of early failures. When β is equal to 1, the product has a constant failure rate. This means the device is in its normal mode of operation and should last for its lifetime. When β is greater than 1.0, the product has an increasing failure rate. This means that the device is in its final stage of lifetime and it is failing due to wear-out.

The scale parameter α is the TTF at 63% failures. This is because when $\ln(-\ln(1-F(t)))$ is equated to 0, $F(t)$ is 63%. Hence, for the Weibull distribution, the lifetimes at 63% are used to compare different materials or processes.

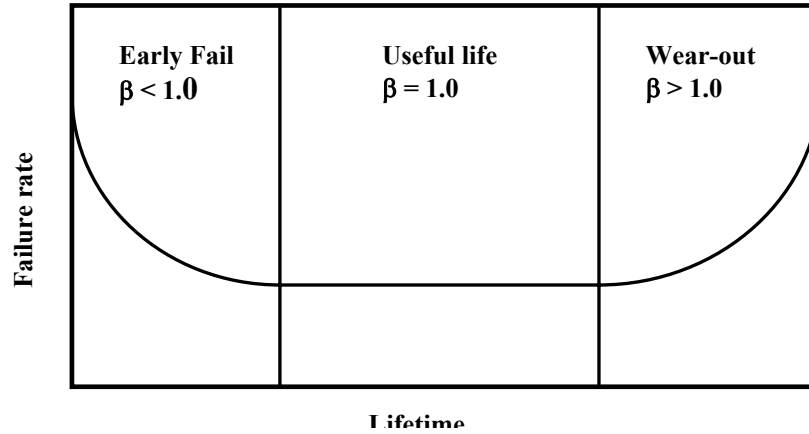


Figure 2.6 Bathtub curve of lifetime shows the early failure, useful life and the wear-out stage.

2.6 CU/LOW-K DUAL DAMASCENE STRUCTURE

The Cu/low- κ interconnect structures are built by a process known as damascene. In this process, metal lines and vias are etched in the dielectric and then filled with copper. The copper is then polished back by a process known as chemical mechanical polishing (CMP).

Cu/low- κ interconnects can be made by a single damascene process or dual damascene process. In single damascene the via-level dielectric is deposited first then it is patterned and etched. Next the metal-level dielectric is deposited, patterned and etched. In the dual damascene scheme, the dielectric is deposited for both via and metal level. The dual damascene is favored because of fewer process steps. In the dual damascene scheme, the trench may be etched first or the via may be etched first. The via-first is favored over the trench-first because in the trench-first approach there may be resist pooling at the trench. It is difficult to

form fine lines with thick resist at the trench. In the via-first approach the only pooling that occurs is at the bottom of the via which can actually help in preventing over-etching during the trench etch.

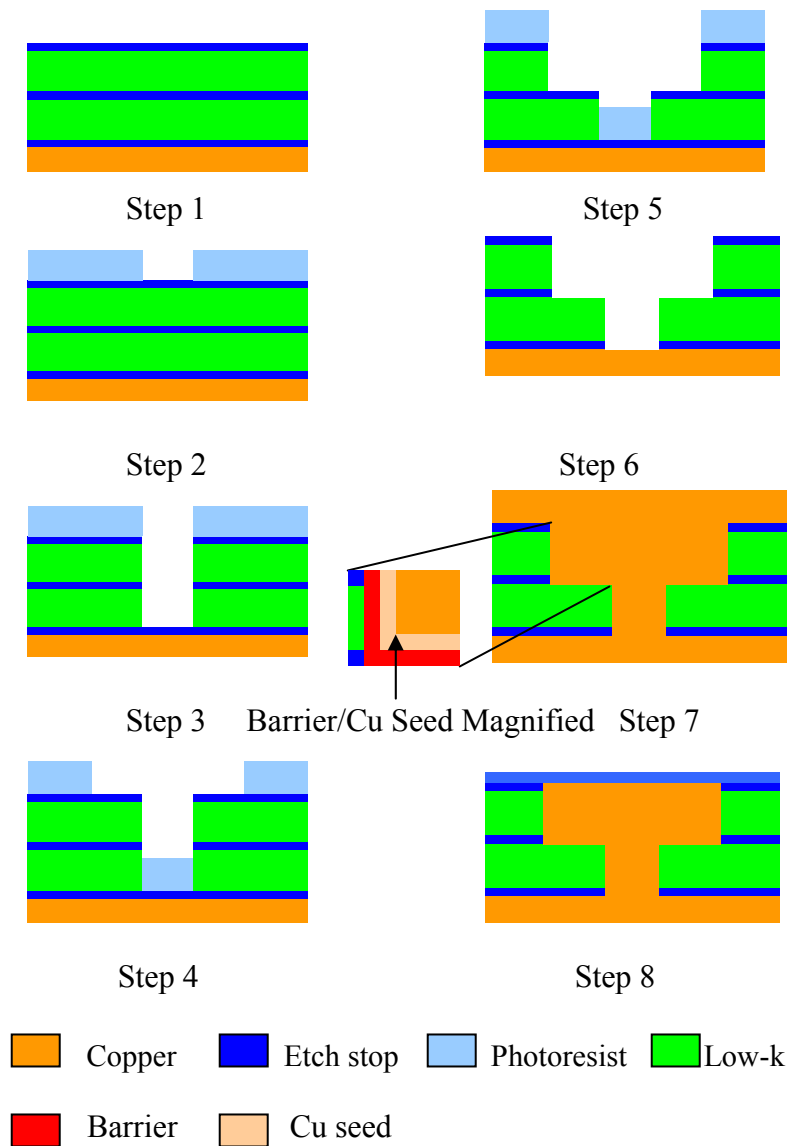


Figure 2.7 Schematic diagram of the via-first Dual Damascene process

Fig 2.7 shows the various steps in the dual damascene process. In the first step the etch-stop layers and hard mask and low- κ layers are deposited. In step 2 the photoresist is coated and lithographically patterned. In step 3 the via is etched in plasma. Plasma etching is directional. The etching agents are a combination of fluorocarbons, hydrogen, oxygen and nitrogen. The etch products are volatile products of carbon and silicon. After the etching the resist has to be removed by a process step known as ashing. The ashing gases are a combination of nitrogen, hydrogen and oxygen. In step 4 the photoresist is coated for the trench and lithographically patterned. In step 5 the trench is etched and the photoresist is removed. In step 6 the via bottom barrier is removed. In step 7 the tantalum barrier is deposited, followed by a copper seed layer deposition, which is followed by copper deposition by electrolysis. In the last step, the excess copper is removed by CMP and a capping layer is deposited.

2.7 LOW-K LEAKAGE AND RELIABILITY

The leakage and reliability of low- κ dielectrics in the dual damascene structure is becoming more important as line-width continue to shrink. There has been many papers published [Shi (1996), Solis (1997), Kondoh (1998), Gao (1999), Lee (2000), Hu (2000), Lin (2001), Mosig (2001), Cho (2001), Lamy (2002), Peters (2002), Braun (2002), Liu (2002)] on the deleterious effects of etching and ashing and various solutions have been suggested to optimize the processing conditions to obtain better trench contours and lower the capacitance values.

Loke (1998) shows that the interfacial leakage dominates over bulk leakage. Various authors [Wu (2001) Yiang (2003), Allers (2003), Chiang (2004)] have shown that in Cu/low- κ structures Frenkel-Poole leakage mechanism dominates. This type of conduction mechanism suggests that defects and traps dominate the conduction process in Cu/low- κ structures. Nakamura (2002) shows that the leakage current is sensitive to ashing condition.

Wu (2000) describes a physical model for TTDB failure based on copper ionization and injection and drift of copper ions. Tsai (2000) have also indicated that the top interface is the region of final failure. Noguchi (2001) shows that the TDDB reliability failure was at the top interface due to the enhancement of the electric field at the top corners. He also shows that the TDDB characteristics could be improved by optimizing the CMP conditions. Chiang (2004, 2003) also shows that the field enhancement at the top interface is responsible for the dielectric failure. Tada (2003) shows that the leakage current path is at the interface and not in the bulk dielectric. They show that using the same material as the hard mask and capping layers could improve the reliability. Jow (2003) and Alers (2004) shows that the dielectric failure mechanism is at the top interface due to mechanical delamination caused by the electrostatic force between the interdigitated comb test structures. Ogawa (2003) analyzed the TDDB failure on the basis of percolation. They show that porosity degraded the breakdown and TDDB performance.

The processing effects on the Cu/low- κ structures have been analyzed in terms of the degradation in the k -value. Mor (2002), Clark (2003) and Colburn

(2004) show that an etching and ashing increases the silanol content in the low- κ dielectric. The silanol cause the material to become hydrophilic and degrades the electrical properties. They also show that a post-ash chemical treatment by hexamethyldisilazane (HMDS) vapor reduced the silanol concentration and as a result reduced the k -value of the dielectric and restored the hydrophobicity of the film. Iacopi (2004) suggests a method for quantification of the etching and ashing damage on the dielectric. They considered the intra-level dielectric as a series of capacitors with the κ value changing at the side-wall interface due to the processing damages. They show that it is possible to infer a damage layer thickness by plotting reciprocal of capacitance versus the spacing. They also show that the sidewall damage is responsible for the degradation of leakage and breakdown as the line width becomes smaller.

However there has not been a comprehensive study of the electrical and reliability properties of the Cu/low- κ structures after post ash cleaning and chemical treatments. In this study the effect of post-ash cleaning and chemical treatments will be analyzed in terms of k -value, leakage, breakdown and reliability. The electrical performance of different cleans and treatments will be compared and the compositional changes in the dielectric films will be analyzed. The objective of this study is to determine and understand the effects of compositional changes at the low- κ trench interface on the dielectric properties and reliability of Cu/low- κ structures.

Chapter 3: Conduction Mechanisms of Low- κ Dielectrics

In this chapter the electrical characteristics of silicon dioxide, methyl-silsesquioxane (MSQ) type of low- κ material and polymeric type of low- κ material will be discussed. First the test structure will be described. Then the κ value, leakage current conduction mechanism and breakdown of the three films will be determined and compared. Finally, the implication of the conduction mechanism on reliability testing will be discussed.

3.1 SAMPLES AND EXPERIMENTAL SETUP

Fig 3.1 shows a schematic of the test structure used to perform the electrical tests. The structure is an MIS capacitor. The capacitors were defined using subtractive aluminum etch.

Three films were tested. Silicon dioxide (SiO_2), methyl-silsesquioxane type of low- κ material (JSR) and polymeric type of low- κ material (SiLK^{TM}) were investigated. The oxide thickness was 0.2 μm . The JSR thickness was 0.4 μm and the p- SiLK^{TM} thickness was 0.3 μm . The JSR and p- SiLK^{TM} films had a 500 Å thick silicon nitride (SiN) layer above the blanket films.

The dielectric constant was calculated from capacitance measurements. In subsequent calculation of barrier heights, the dielectric constants are taken to be 3.90, 2.29 and 2.04 for oxide, p- SiLK^{TM} and JSR respectively. Capacitance was measured at 100 kHz with an HP4284 LCR meter. The κ value depends upon the frequency. Although actual operating frequencies are in the low gigahertz range, the experimental values are measured in kilohertz range because of instrumental limitations. However, the dielectric constant does not change drastically up to

high gigahertz range. Hence comparison of the κ values at 100 kHz is acceptable. The capacitance at -3 V was used to calculate the κ -value. Leakage current was measured with an HP4156 Semiconductor Parametric Analyzer. The voltage was ramped at a constant ramp rate of 3 V/s for the ramp voltage breakdown measurements. All measurements were made on 2mm^2 area capacitors and measurements were made at temperatures ranging from 25°C to 300°C.

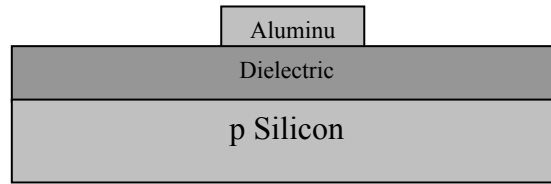


Figure 3.1 Schematic of test structure used for electrical measurements

3.2 SILICON DIOXIDE

Fig 3.2 shows the current versus electric field plot for SiO_2 . The curves were fit to Schottky mechanism from 3-6MV/cm. The current at 250°C and 295°C fit the Schottky mechanism with a κ value of 3.9. Fig 3.3 shows the Schottky fit. Above 7MV/cm the curves were fit with the tunneling mechanism. Fig 3.4 shows the tunneling fit. The barrier height ϕ_B is calculated from the Schottky fit and the Tunneling fit. Fig 3.5 shows the dependence of the barrier height on temperature as calculated from the Tunneling fit. The barrier height should be independent of temperature for purely tunneling leakage. The barrier height is also calculated

from the Schottky fit and the data from both fits is plotted versus effective mass in Fig 3.6.

The current vs. field curves for oxide shows a typical tunneling mechanism above 6MV/cm. The effective mass as reported in the literature is shown in Table 3.1. Assuming a value of $0.42m_e$ we get a barrier height of $3.02 \pm 0.02 \text{ eV}$ at 25°C . Above 200°C , thermionic emission takes place at electric fields lower than 6MV/cm and both Schottky and tunneling occurs at higher fields. As a result a plot of barrier height vs. temperature shows a drop above 200°C . The barrier height, as calculated from the Schottky fit at 295°C and $m^*=m_e$, is $2.05 \pm 0.03 \text{ eV}$. The barrier height for Schottky emission represents the minimum energy required for injecting thermally excited electrons into the conduction band. Table 3.1 lists the SiO_2 barrier heights from the literature.

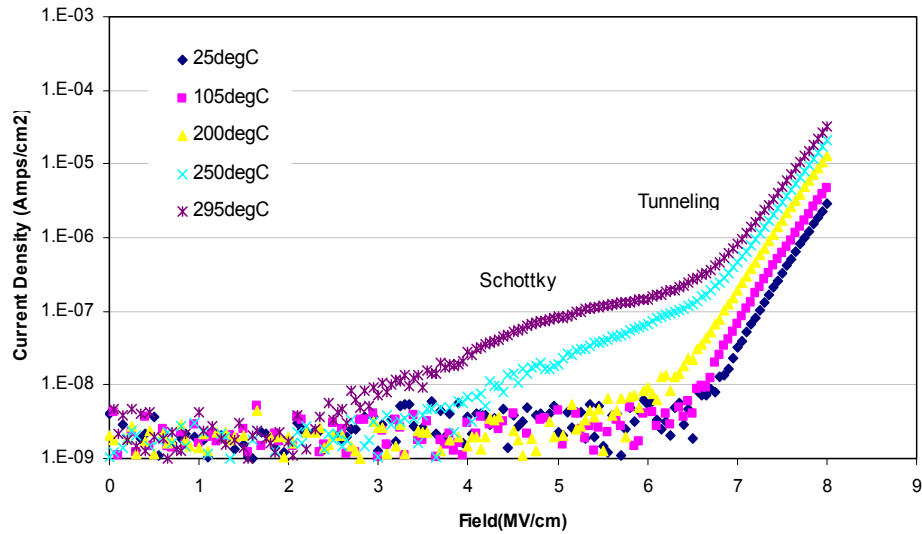


Figure 3.2 JE plot for oxide shows tunneling at high fields and Schottky at high temperatures

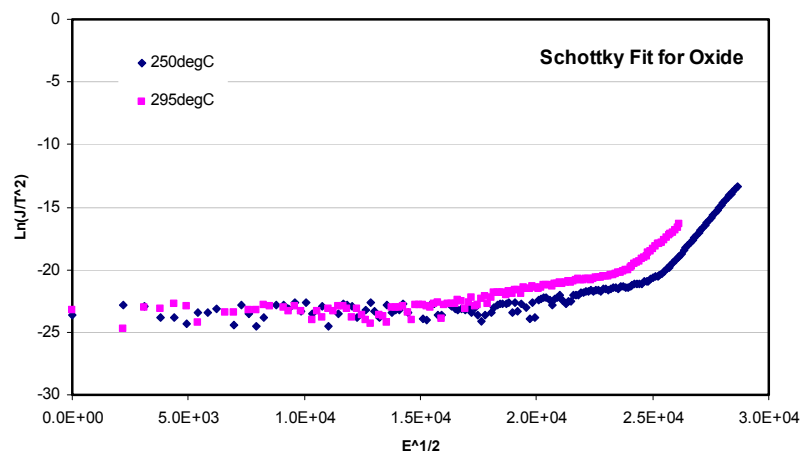


Figure 3.3 Schottky conduction mechanism fit for oxide

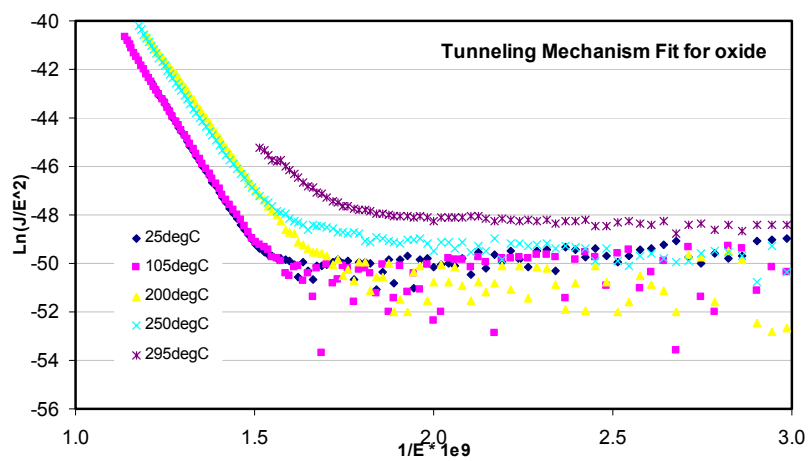


Figure 3.4 Tunneling conduction mechanism fit for oxide

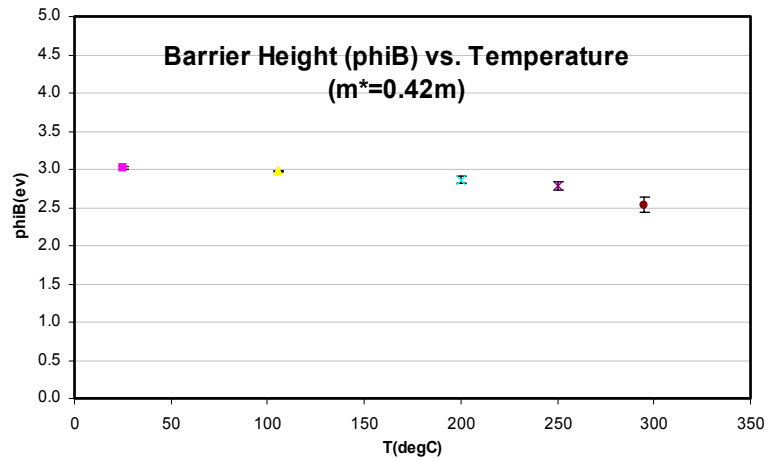


Figure 3.5 Barrier height calculated from tunneling fit shows that the barrier height is independent of temperatures except at high temperatures when Schottky emission contributes to the total current

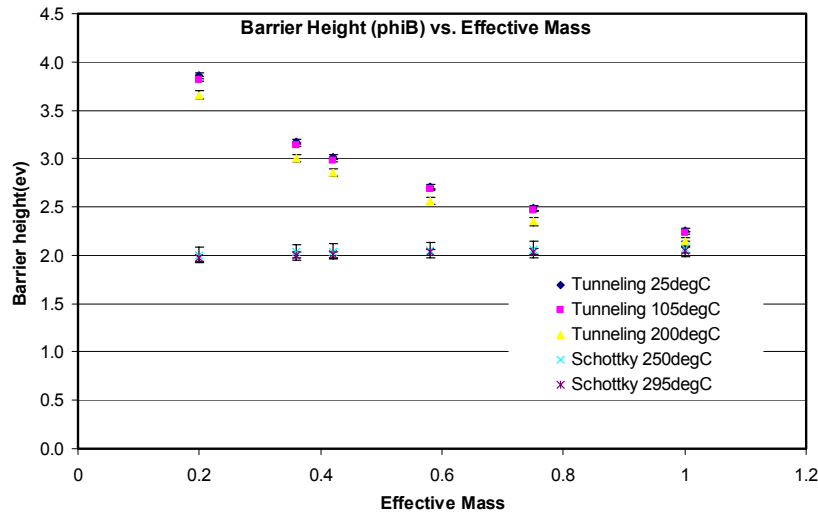


Figure 3.6 Barrier height calculated from tunneling and Schottky fit shows that the barrier height decreases with increasing effective mass for the tunneling leakage.

Source	Electrode	Barrier Height (ev)	Effective Mass (m^* / m_e)
Lenzlinger (1969)	Si	3.06	0.42
Weinberg (1977)	Si	2.90	0.50
Krieger (1981)	Si	2.89	0.36
Av-Ron (1981)	Al	3.18	0.64
Brar (1996)	Al	3.17	0.42
Nagano (1994)	Si	3.34	0.36
This Study	Si	3.02	0.42

Table 3.1 Tunneling barrier height and effective mass at 25°C as reported in the literature for SiO₂

3.3 POLYMERIC DIELECTRIC (SiLK™)

Fig 3.7 shows the current vs. electric field plot for p-SiLK™. The curves were fit to Schottky mechanism for temperature above 200°C with a κ value of 2.29. Fig 3.8 shows the Schottky fit. Below 200°C and above 4 MV/cm the curves were fit with the Frenkel-Poole mechanism with a κ value of 2.29. Fig 3.9 shows the Frenkel-Poole fit. The barrier height ϕ_B for both Schottky and Frenkel-Poole emission is calculated from the Schottky fit and the Frenkel-Poole fit. Fig 3.10 shows the dependence of the calculated barrier heights on temperature. Fig 3.11 shows the dependence of the barrier height on effective mass.

The current versus field curves for p-SiLK™ shows two distinct conduction mechanisms. Below 200°C and above 4 MV/cm there is Frenkel-Poole leakage but above 200°C there is Schottky leakage throughout the entire electric field range. The Frenkel-Poole barrier height is 1.37 ± 0.11 ev at 25°C and

above 4MV/cm. The Schottky barrier height is $1.96 \pm 0.02 \text{ eV}$ at 295°C and $m^* = m_e$. The Frenkel-Poole leakage is a field enhanced thermal excitation of electrons from trapped states into the conduction band.

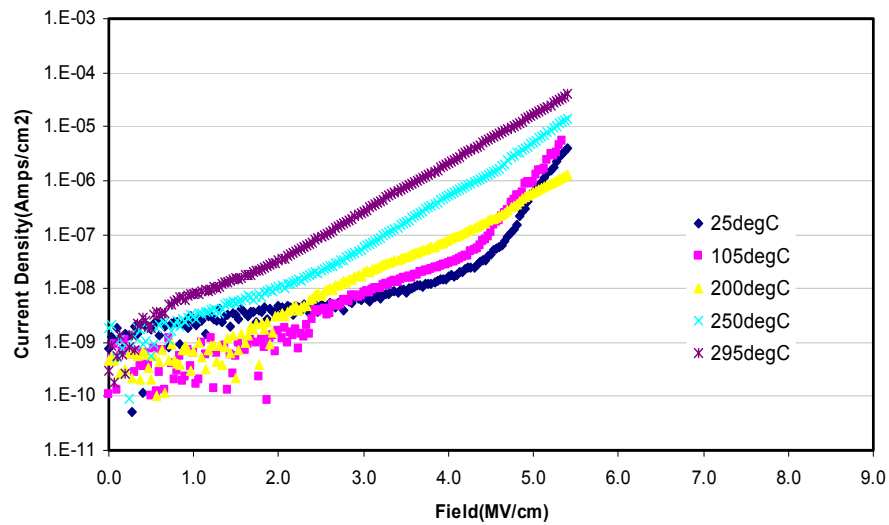


Figure 3.7 JE plot for p-SiLK™ shows Frenkel-Poole leakage at low temperatures and high fields and Schottky leakage at high temperatures

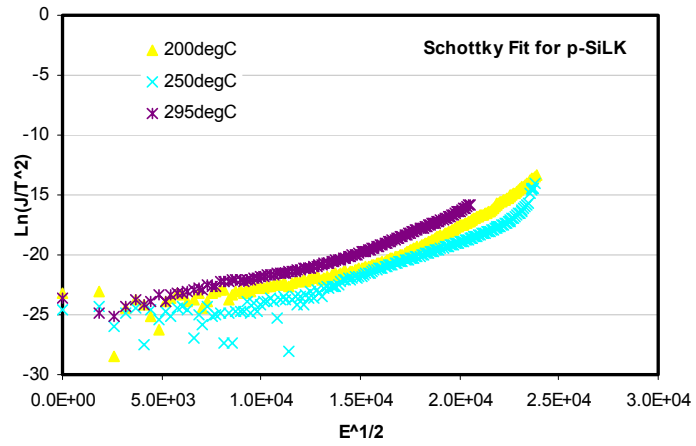


Figure 3.8 Schottky fit for p-SiLKTM

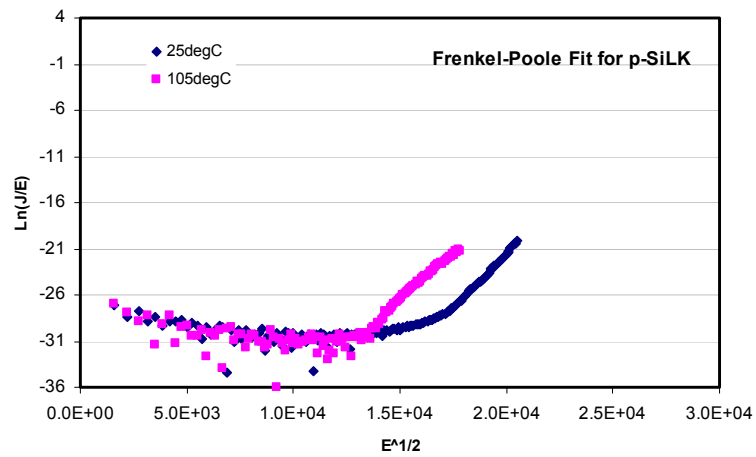


Figure 3.9 Frenkel-Poole fit for p-SiLKTM

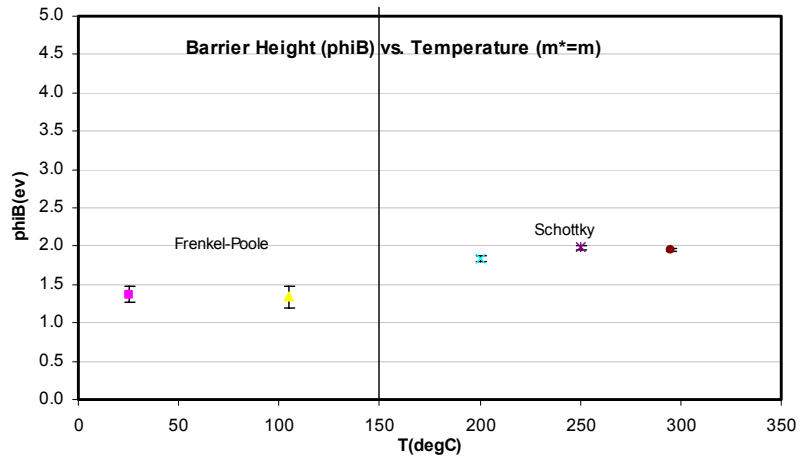


Figure 3.10 Barrier height calculated from Schottky and Frenkel-Poole fit shows that the Frenkel-Poole barrier height is lower than the Schottky barrier height

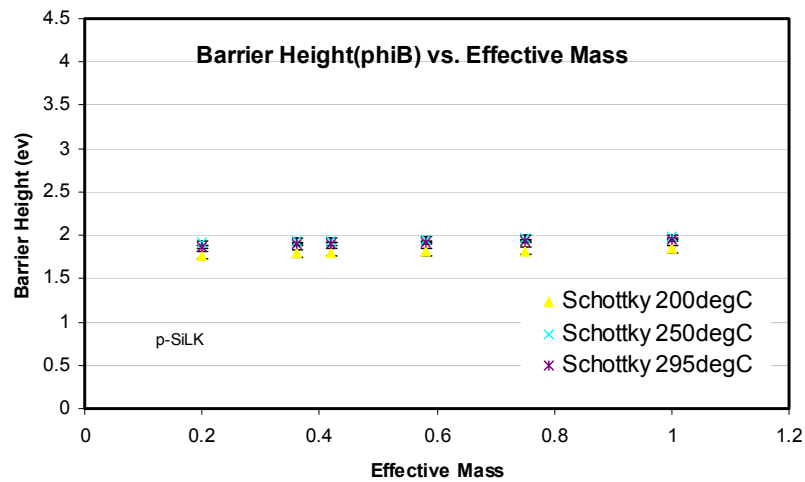


Figure 3.11 Barrier height calculated from Schottky fit shows that the barrier height is independent of the effective mass

3.4 MSQ TYPE DIELECTRIC (JSR)

Fig 3.12 shows the current versus electric field plot for JSR. The curves were fit to space-charge-limited (SCL) conduction mechanism for temperatures up to 250°C. The current at 295°C fit the Schottky conduction mechanism with a κ value of 2.04. Fig 3.13 shows the space-charge-limited fit and Fig 3.14 shows the Schottky fit at 295°C. The barrier height calculated from the Schottky fit at 295°C and $m^*=m_e$ is $1.95 \pm 0.01\text{eV}$. From the slopes of the space-charge-limited fit, the electron mobility is extracted for $k=2.04$. Fig 3.15 shows the mobility dependence on temperature. The mobility is exponentially dependent on temperature. The zero-field mobility thermal activation energy is $\Delta=57.6\pm5.6\text{meV}$. Table 3.2 shows the mobility of polymers as reported in the literature.

The current versus field curves shows a typical space-charge-limited conduction process. Initially there is Ohmic leakage until a critical transition voltage [Kao (1981)]. Above the transition voltage, the SCL dominates over the Ohmic leakage. The current is proportional to square of the voltage and the slope gives the mobility. The saturation of current seems to indicate that there is a charge build-up at the interface after the initial increase. If we compare p-SiLKTM and JSR, both of them have a SiN interface layer below the aluminum top electrode and both of them are deposited on a low-resistivity silicon substrate. However, p-SiLKTM (Fig 3.7) does not show current saturation while JSR (Fig 3.12) does. This seems to indicate that the interface between SiN and JSR is different from the interface between SiN and p-SiLKTM. A charge build-up probably occurs at the SiN-JSR interface that saturates the current. Charge build-

up may occur because of scattering due to interfacial roughness or mobility gradient between the two materials. Finally at very high fields, dielectric breakdown occurs. Further discussion will be presented in Section 3.6.

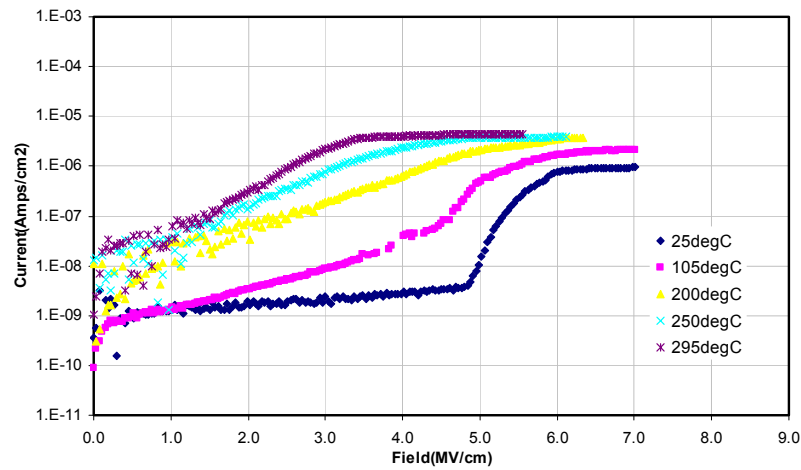


Figure 3.12 JE plot for JSR shows Ohmic leakage at low temperatures and low fields and SCL leakage at low temperature and high fields. There is also Schottky leakage at high temperatures and current saturation at higher electric fields

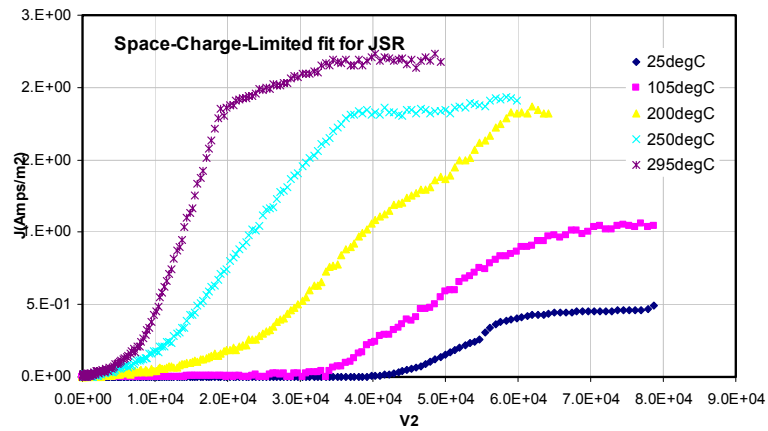


Figure 3.13 Space-charge-limited fit for JSR

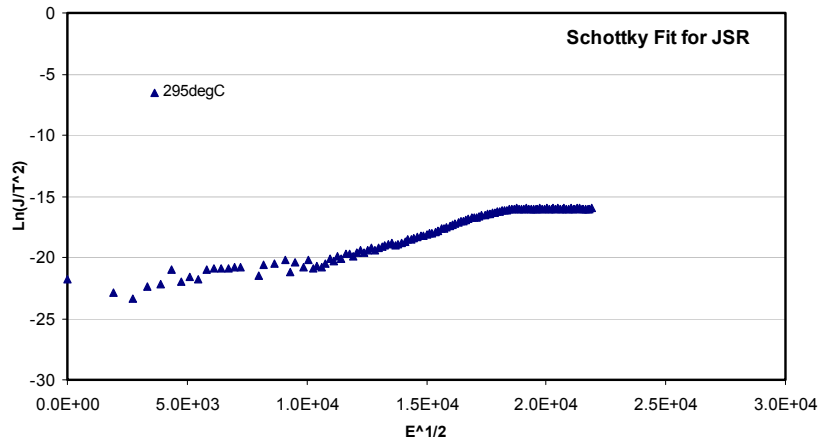


Figure 3.14 Schottky fit for JSR

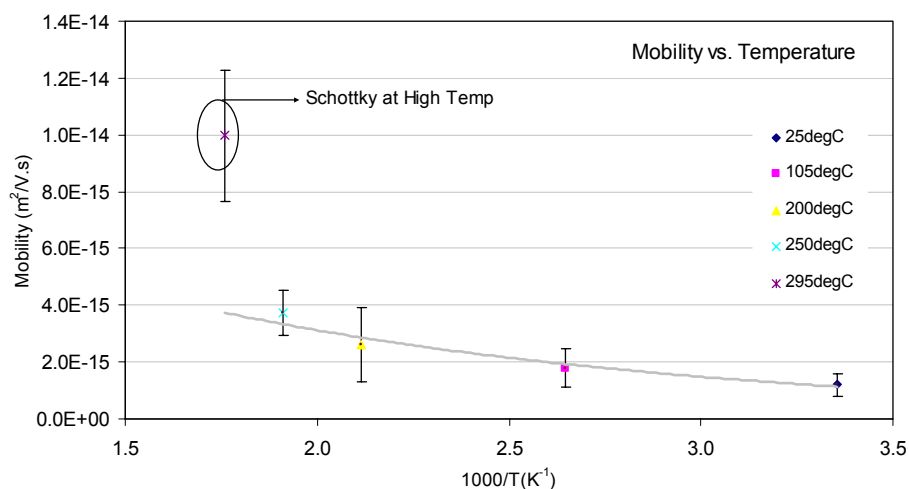


Figure 3.15 Electron mobility versus $1000/T$ calculated from SCL fit for JSR shows an exponential dependence except for 295°C where there is Schottky contribution to the total leakage

Source	Polymer	Mobility at RT ($\text{m}^2\text{V}^{-1}\text{s}^{-1}$)	Zero Field E_a (eV)
Reiser (1969)	Polymethylmethacrylate	2.5×10^{-15}	0.52
	Perspex	3.6×10^{-15}	0.48
	Poly-n-butyl-methacrylate	2.5×10^{-14}	0.65
	Lucite	3.5×10^{-13}	0.52
	Polystyrene	1.4×10^{-15}	0.69
	Butvar	4.5×10^{-15}	0.74
	Vitel	4.0×10^{-15}	1.08
	Polyisoprene	2.0×10^{-16}	1.08
	Silicone	3.0×10^{-18}	1.73
	Polyvinylacetate	2.2×10^{-16}	0.48
Keiss (1980)	PET	1.1×10^{-10}	0.20
	PS	2.1×10^{-15}	0.20
Bozano (1999)	MEH-PPV	1.2×10^{-13}	0.34
This study	JSR	1.2×10^{-15}	0.18

Table 3.2 Electron mobility in polymers at RT from literature

3.5 RAMP VOLTAGE BREAKDOWN

Ramp voltage breakdown tests were performed on the oxide, p-SiLKTM and JSR wafers. Fig 3.16, Fig 3.17 and Fig 3.18 shows the dependence of breakdown voltage on temperature for oxide, p-SiLKTM and JSR respectively. Fig 3.19 summarizes the average breakdown voltage for these three dielectrics.

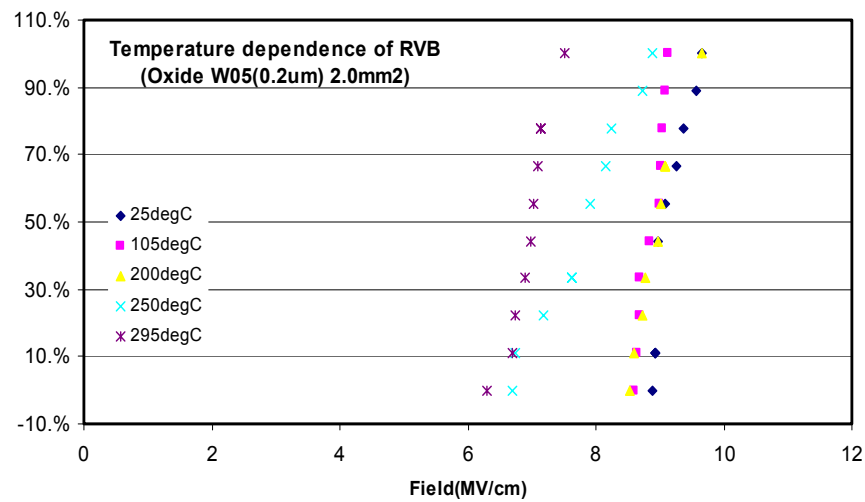


Figure 3.16 Temperature dependence of RVB for oxide shows lower breakdown field at higher temperatures

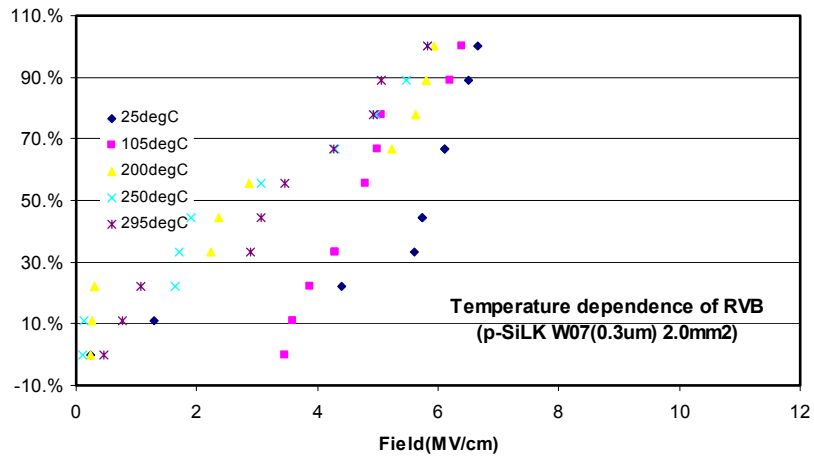


Figure 3.17 Temperature dependence of RVB for p-SiLK™ shows lower breakdown field at higher temperatures

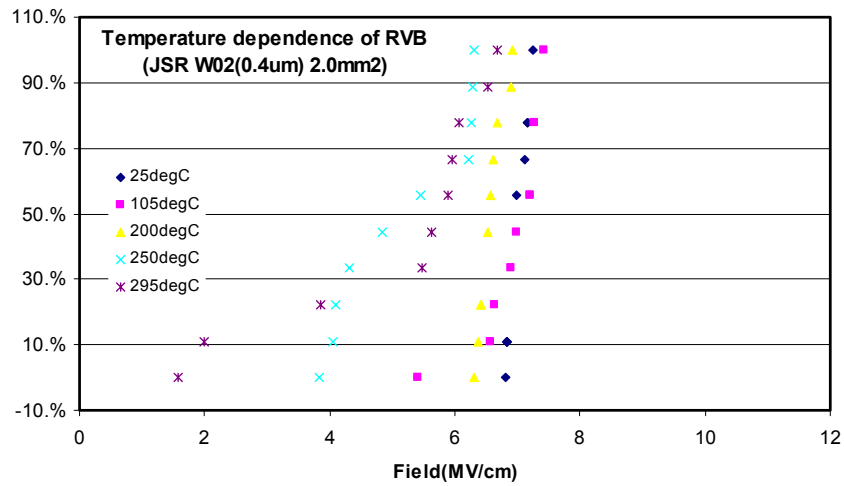


Figure 3.18 Temperature dependence of RVB for JSR shows lower breakdown field at higher temperatures

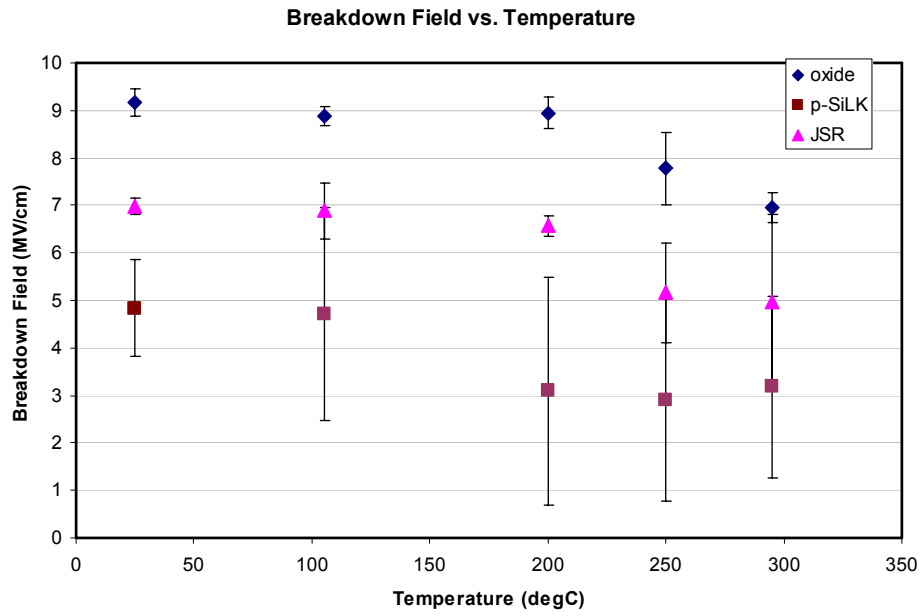


Figure 3.19 Temperature dependence of RVB shows lower breakdown field at higher temperatures for the three dielectrics and breakdown fields is higher for oxide than JSR which is higher than p-SiLKTM

Dielectric	Tunneling (25°C and $m^*=0.42m_e$)	Frenkel-Poole (25°C)	Schottky (295°C and $m^*=m_e$)
Oxide	$3.02 \pm 0.02 \text{ eV}$		$2.05 \pm 0.03 \text{ eV}$
p-SiLK TM		$1.37 \pm 0.11 \text{ eV}$	$1.96 \pm 0.02 \text{ eV}$
JSR			$1.95 \pm 0.01 \text{ eV}$

Table 3.3 A summary of barrier heights shows that the Schottky barrier height is similar for the low- κ dielectrics

Fig 3.19 shows that SiO₂ has a higher breakdown field than JSR, which in turn has a higher breakdown field than p-SiLKTM. The breakdown of the dielectric is a combination of electrical and thermal breakdown. Electrical breakdown phenomenon has thermal effects but it is not caused by temperature. Generally electrical and thermal breakdown occur simultaneously. Electrical degradation of a dielectric occurs when the electric field is high enough to cause destruction of the bond structure and removal of electrons and ionization of atoms. This effect is accelerated when there are defects present inside the dielectric. Charge buildup occurs at defect sites. This causes localized enhancement of electric fields. Higher local fields cause more local defects to form which in turn traps more charge. This process continues until the dielectric breaks down in a local area. The heat generated by this breakdown is not dissipated fast enough. Hence thermal degradation of the surrounding area also occurs simultaneously. Ultimately the dielectric fails at an electric field that is lower than the intrinsic breakdown field.

The breakdown in SiO₂ is due to impact ionization caused by tunneling electrons. The breakdown in p-SiLKTM is due to defect related electrical and thermal degradation of the dielectric. The conduction mechanism in p-SiLKTM is Frenkel-Poole. This is indicative of defect states present in the dielectric.

For the devices that were tested, JSR does not exhibit Frenkel-Poole. Instead the conduction mechanism is SCL. However at high fields there is current saturation. This is probably due to charge build-up at the nitride and JSR interface. An initial surge in current is followed by a saturation period. The charge build-up at the anode reduces the injection from the cathode. After a certain

saturation period, the current slowly increases until breakdown occurs. The breakdown mechanism in JSR is also defect related.

The RVB plots for the three dielectric shows that there is degradation of the breakdown field above 200°C. At high temperatures there is an increase in Schottky emission which increases the charge buildup. As a result the localized enhancement of electric field occurs at lower fields. Also thermal degradation is accelerated at higher temperatures because the dielectric cannot dissipate the heat fast enough. This causes the dielectric to fail at lower electric fields.

3.6 DISCUSSION

The analysis of three different types of dielectric shows that there can be different types of conduction mechanism at different ranges of electric fields for different dielectrics. Silicon dioxide had been in use as an ILD for a long time. It has low leakage at low fields and has a high breakdown field. At high temperatures there can be Schottky emission but generally there is negligible leakage until fields are high enough to cause tunneling. Breakdown is believed to be due to impact ionization caused by tunneling electrons.

The polymeric dielectric, p-SiLKTM, has Frenkel-Poole type of leakage at low temperatures and Schottky leakage dominates at high temperatures. This indicates that leakage in this polymeric dielectric is bulk limited and controlled by defect states. Trap states near the interface of the dielectric lowers the barrier height, which makes charge injection from the electrode more favorable.

JSR, which is an MSQ type of low- κ dielectric, mainly exhibits SCL leakage. Initially there is Ohmic leakage until a critical transition voltage [Kao (1981)]. Above the transition voltage, the SCL dominates over the Ohmic leakage. The current is limited by the bulk dielectric. When the field is high enough, there is a surge in current. The absence of Frenkel-Poole conduction indicates that there are no permanent defects states. At higher temperatures there is also Schottky emission. The high surge in SCL current is followed by saturation of current as shown in Fig 3.12. The current then slowly increases until breakdown occurs. The current saturation for JSR is due to the interface between SiN and JSR. The surge in current is limited by the ability of this interface to allow charge to move across it.

If we only compare RT leakages then oxide leakage is at the noise level whereas both p-SiLKTM and JSR have leakage around $1 \times 10^{-9} \text{ A/cm}^2$ at 2 MV/cm. However, at 250°C and 2MV/cm, p-SiLKTM has a leakage of about $1 \times 10^{-8} \text{ A/cm}^2$ whereas JSR has a leakage of about $1 \times 10^{-7} \text{ A/cm}^2$. Oxide leakage is still at the noise level. Thus, there is an order of magnitude difference in leakage currents between JSR and p-SiLKTM at high temperatures.

JSR and p-SiLKTM blanket films both show defect induced leakage current. Initially they both exhibit Ohmic leakage ($J \sim E$). After a critical voltage, JSR exhibits SCL ($J \sim V^2$) and p-SiLKTM exhibits Frenkel-Poole ($J \sim \exp(\sqrt{E})$) type of bulk limited conduction.

A perfect dielectric does not exist. There are generally structural and/or chemical defects present in the dielectric. Structural defects may be dangling

bonds or displaced atoms or molecules which produce vacancies and interstitial stress in the dielectric. Chemical defects are atoms or molecules that do not belong in the dielectric structure. Hydroxyl groups at the interface are an example of chemical impurity which would distort the molecular structure and create trap states near the interface of the dielectric. The effect of hydroxyl impurity is discussed further in Chapter 5. Chemical defects may be created by etching and ashing processes. These processes can cause a change in the molecular structure of the MSQ dielectric by depleting the carbon and could create low-energy Si-OH (100kJ/mole) and Si-Si (220kJ/mole) bonds which would weaken the dielectric.

If we assume breakdown occurs due to breaking of chemical bonds, then the dielectric is only as strong as the weakest bond. When the voltage is high enough, the weakest bonds are assumed to be broken and electrons and ions are formed. Energetic electrons can be emitted by tunneling processes, which would further break the weakest bonds and produce a cascade of carriers. If the weakest bonds are present throughout the dielectric, then at a critical voltage a surge of carriers will destroy the dielectric. On the other hand if the weakest bonds are present at or near the interface, the carriers will produce a cascade of carriers by impact ionization. Ultimately failure occurs by molecular degradation and thermal heating.

The chemical bonds at the interface of silicon dioxide and the native oxide on the substrate are Si-O (453kJ/mole) and possibly Si-Si (220kJ/mole) which is a weak defective bond.

The generalized formula of MSQ (methyl-silsesquioxane) is $((\text{CH}_3)_{1.0}\text{Si}_{1.0}\text{O}_{1.5})_n$ where each silicon atom is attached to one and a half (sesqui) oxygen atoms and one methyl group. The interface between the MSQ dielectric and the SiO_2 on the substrate is postulated schematically in Fig 3.20. The SiO_2 on the silicon substrate is the native oxide. The schematic shows that the bonds at the interface are Si-C (301kJ/mole) and Si-O (453kJ/mole). The Si-O bond is much stronger than O-O (140kJ/mole) bond hence Si-O bonding will be preferred over O-O bonding.

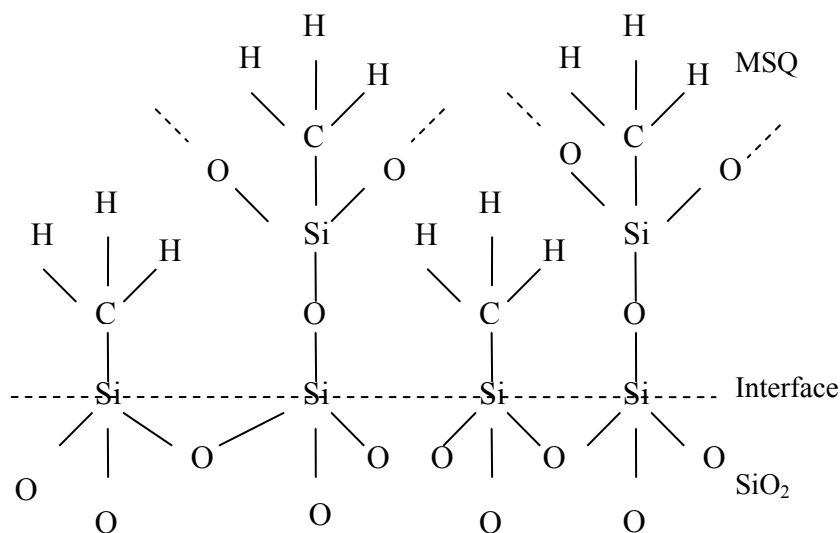


Figure 3.20 Schematic of postulated chemical bonds at the interface of JSR and SiO_2

The chemical structure of p-SiLKTM consists of cross-linked polyphenylenes. Fig 3.21 shows the chemical structure [Martin (2000)]. The postulated chemical bonds at the interface with SiO_2 are C-O (337kJ/mole), Si-O

(453kJ/mole), O-O (140kJ/mole) and Si-C (301kJ/mole). Fig 3.22 summarizes the interfacial bond strengths of the three dielectrics.

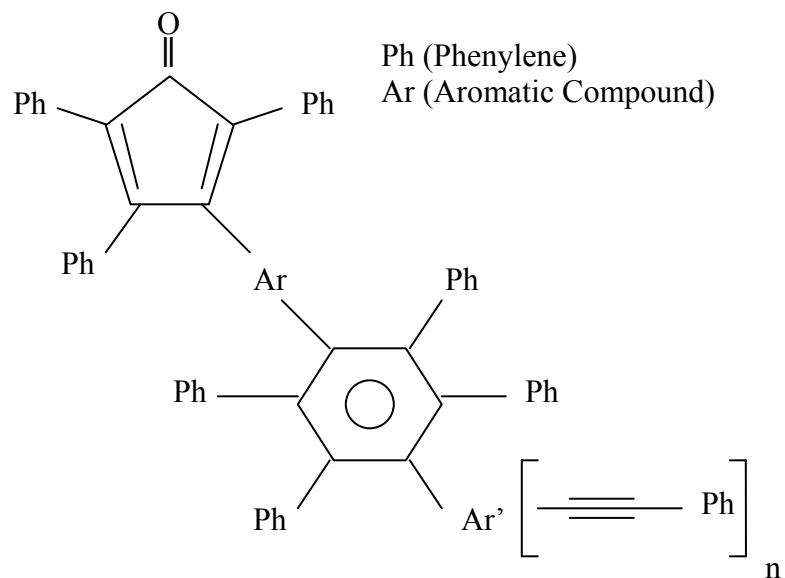


Figure 3.21 Chemical structure of p-SiLK™ shows a cross-linked polyphenylene system

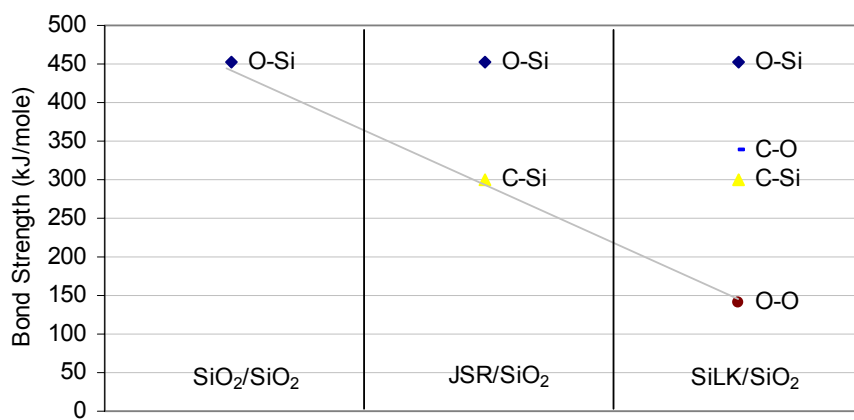


Figure 3.22 Bond strengths versus the dielectric stack shows the possible interfacial bonds for the three dielectrics

The high breakdown strength of SiO_2 indicates that the weak Si-Si defective bond is not widespread. Breakdown is probably due to high-field-induced tunneling electrons breaking the SiO_2 molecular structure and causing a cascade of charge which destroys the dielectric by thermal heating.

In the case of JSR, the bond (Si-C) exists not only at the interface but throughout the dielectric because it is an MSQ type of material. This may account for its electrical behavior. The bulk limited SCL leakage for JSR is due to random defects generated throughout the dielectric due to the breakage of Si-C bonds at a critical electric field. Initially there is low Ohmic leakage until a critical field is reached. The surge in current is due to large number of defects being generated at a critical electric field. Theoretically the electric field required to break the Si-C bond is orders of magnitude higher than experimentally observed. The reason is that in theoretical calculations we assume a perfect dielectric. In real cases the pre-existing defects contribute charge to the total current and the actual breakdown field is much less than theoretical calculations.

In the case of p-SiLKTM, the weakest bond is O-O. The second weakest bond (Si-C) is only at the interface. Hence the Frenkel-Poole leakage for p-SiLKTM is due to the defect states created by the Si-C and/or O-O bonds near the interface. The defect states lower the barrier height for charge injection and give the current an exponential dependence on the electric field. As in the case of JSR, pre-existing defects in the dielectric contribute charge to the total current and the actual breakdown field is much less than theoretical breakdown field.

In a Damascene structure the trench dielectric is surrounded by copper lines on both sides. Fig 3.23 shows the leakage current for a single damascene structure of pitch 0.3 μm for both JSR and p-SiLKTM.

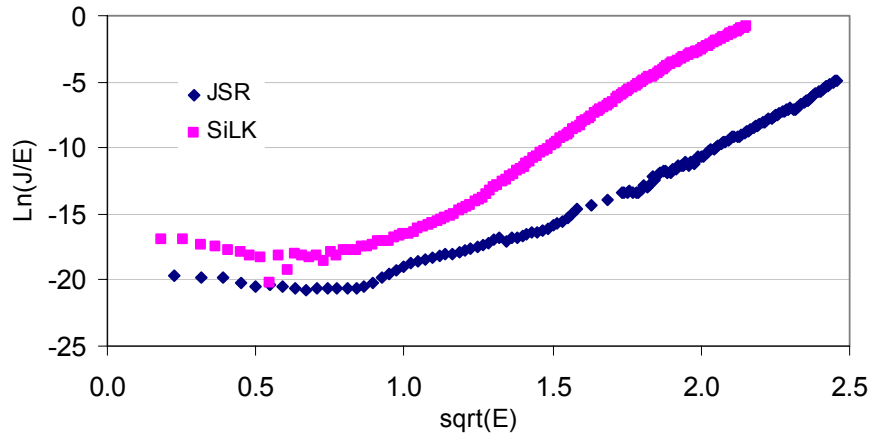


Figure 3.23 Leakage current in a damascene structure is fitted to a Frenkel-Poole conduction mechanism

JSR and p-SiLKTM both show Frenkel-Poole type of leakage. As a blanket film, JSR did not exhibit defect induced Frenkel-Poole leakage. But when it is processed into a Damascene structure it shows Frenkel-Poole leakage. This indicates that defects are generated by the processing conditions. The defects are generated at the sidewall interface during the etching and ashing processes. In the case of JSR, the etching process may preferentially remove Si-C (301kJ/mole) bonds rather than Si-O (453kJ/mole). This would deplete the carbon and Si-OH (100kJ/mole) bonds form at the interface by reaction with the etching agents. There may also be Si-Si (220kJ/mole) bonds at the interface. Carbon depletion could also occur at the p-SiLKTM trench interface, which results in the formation

of more O-O (140kJ/mole) bonds. For both these structures Frenkel-Poole leakage occurs due to barrier lowering at the interface due to defect states created by molecular defects. Final breakdown occurs at lower electric fields compared to blanket films.

We assume that dielectric breakdown is due to the breaking of the weakest bonds. The weakest bonds in SiO₂, JSR and p-SiLK™ blanket films are Si-O, Si-C and O-O respectively. For Damascene JSR and p-SiLK™ structures, Si-OH and O-O are the weakest bonds respectively. Fig 3.24 plots the breakdown fields versus the theoretical bond strengths of several low- κ materials (MSQ1, MSQ2, MSQ3, and ORG1) as well as JSR and p-SiLK™ blanket and Damascene structures. The Damascene process reduces the bond strength at the trench interface and causes breakdown at lower electric fields.

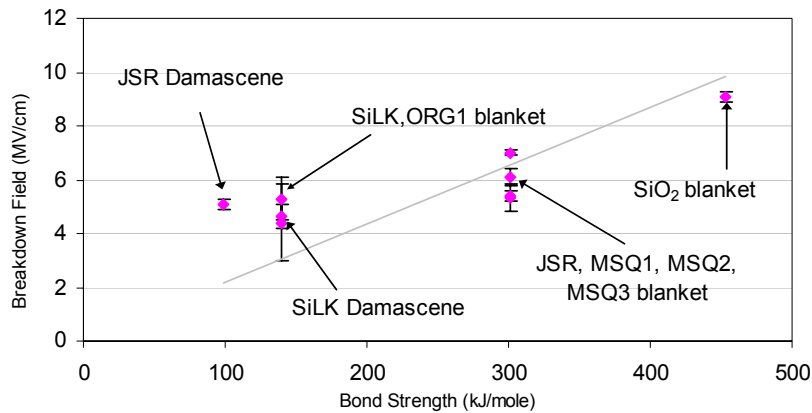


Figure 3.24 Breakdown field versus the bond strength shows that the carbon depleted interfaces of Damascene structures cause weak bonds which reduces the breakdown fields

Although there is a trend between breakdown field and bond strength, the actual breakdown mechanism depend upon the porosity as well as the extent of preferential leakage at the hard-mask or capping layer and low- κ interface. Nevertheless, the type of chemical bond at the trench interface is a fair indication of the strength of dielectric. The strength of the dielectric can be recovered by thermo-chemical treatments which can condense the hydroxyl bonds and repair the trench side-wall damage. Chapter 5 and 6 discusses in detail the chemical repair of the side-wall trenches.

The difference between the two low- κ materials in a Damascene structure is in the magnitude of the leakage and the breakdown. JSR has lower leakage and higher breakdown compared to p-SiLKTM. It also shows better reliability characteristics compared to p-SiLKTM (Fig 3.25). The reliability lifetime of JSR is more than 100 times than that of p-SiLKTM. It should be noted that this is an older version of p-SiLKTM and there are newer versions which have improved electrical properties.

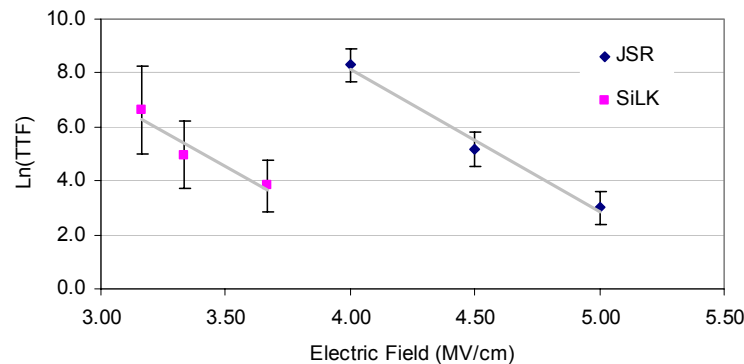


Figure 3.25 Lifetime of JSR and p-SiLKTM for a Damascene structure of 0.5 μ m pitch shows that the lifetime of JSR is about 100 times more than p-SiLKTM

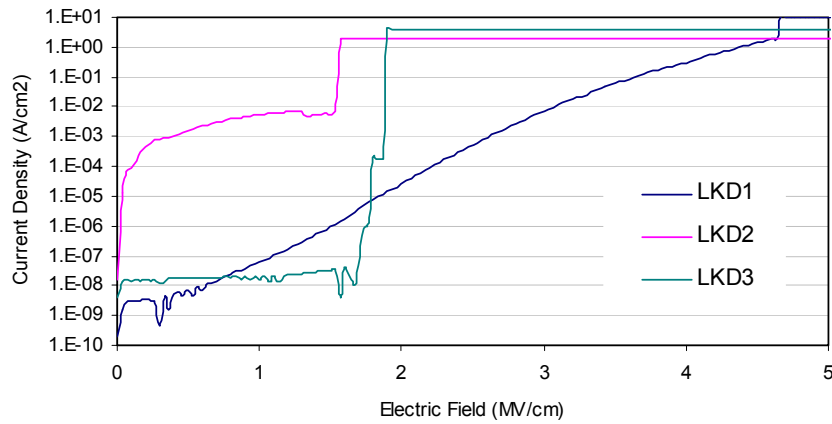


Figure 3.26 Leakage current for three different low- κ materials in a Damascene structure shows the conduction behavior of different dielectrics

It is important to evaluate the conduction mechanism before performing reliability tests. Fig 3.26 shows the leakage current for three different low- κ materials. The leakage characteristics can vary widely for different materials. This could be a material characteristic or processing effect. In either case the reliability testing should be done at similar conduction mechanism so that a valid comparison of the lifetimes can be made. If the purpose is to evaluate the dielectric properties, it is better to use lower temperatures. Then there will be negligible Schottky contribution to the leakage. Conduction will be bulk limited and controlled by the defect states of the dielectric. On the other hand, if the purpose is to determine the barrier integrity it is better to use higher temperatures at which copper ionic conduction will be favored.

Chapter 4: Effect of Pore Size and Distribution on Electrical Characteristics of Blanket low- κ Films

In this chapter four versions of the polymeric low- κ material SiLKTM will be investigated. First the test structure will be described. Then the κ value, leakage current conduction mechanism, breakdown and time-dependent-dielectric breakdown of the four films will be determined and compared. The composition of the low- κ films will be compared by FTIR. SEM and AFM analysis of the films will also be discussed.

4.1 SAMPLES AND EXPERIMENTAL SETUP

Fig 4.1 [Strittmatter (2004)] shows the pore-size and distribution of the porous SiLKTM films. Four films were tested. SiLKTM-D is a dense version of SiLKTM. SiLKTM-V.9, SiLKTM-U and SiLKTM-Y are porous versions of SiLKTM. In the figure, porous SiLKTM resin is also known as SiLKTM-V.9.

SiLKTM -V.9 has a large distribution of pores and it also has larger pores compared to SiLKTM -U and SiLKTM -Y. SiLKTM -Y has the smallest pore size and tightest distribution. All the porous versions have similar pore volume.

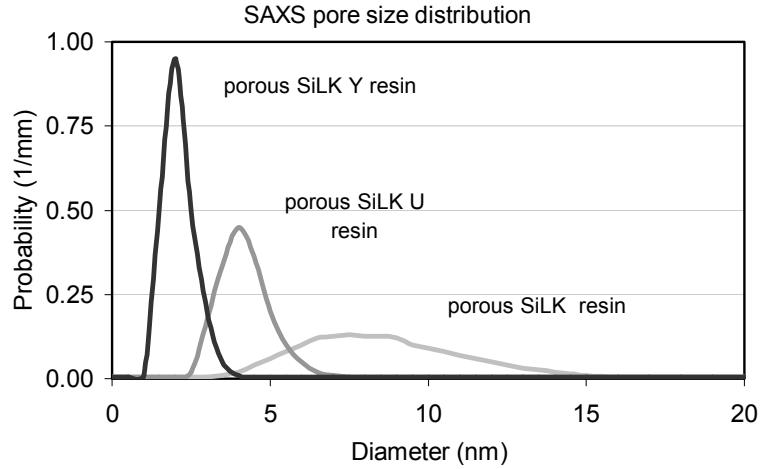


Figure 4.1 Pore size and distribution of porous SiLKTM resins shows that SiLKTM-Y has the smallest pore-size and tightest distribution and SiLKTM-V.9 has the largest pore-size and widest distribution

Fig 4.2 shows a schematic of the test structure used to perform the electrical tests. The structure is an MIS capacitor. The substrate is n-type silicon. The metal is aluminum that is deposited by sputtering under less than 2×10^{-7} Torr pressure. The capacitor is defined using a shadow mask. Capacitance was measured at 100 kHz with an HP4284 LCR meter. The capacitance at +3V was used to calculate the k-value. Leakage current was measured with an HP4156 Semiconductor Parametric Analyzer. The voltage was ramped at a constant ramp rate of 3V/s for the ramp-voltage-breakdown (RVB) measurements. The voltage was kept constant while current was monitored over time for the TDDB measurements. The voltage at which a hard breakdown occurs was taken as the

breakdown voltage. At breakdown the current increases by at least two orders of magnitude and reaches the current compliance limit.

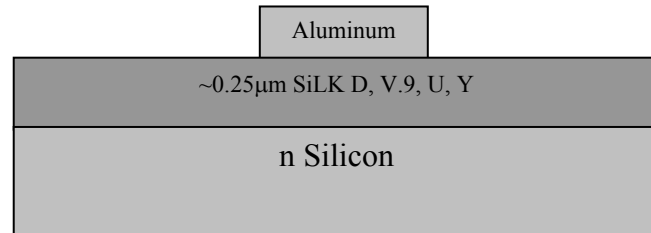


Figure 4.2 Schematic of test structure used for electrical tests

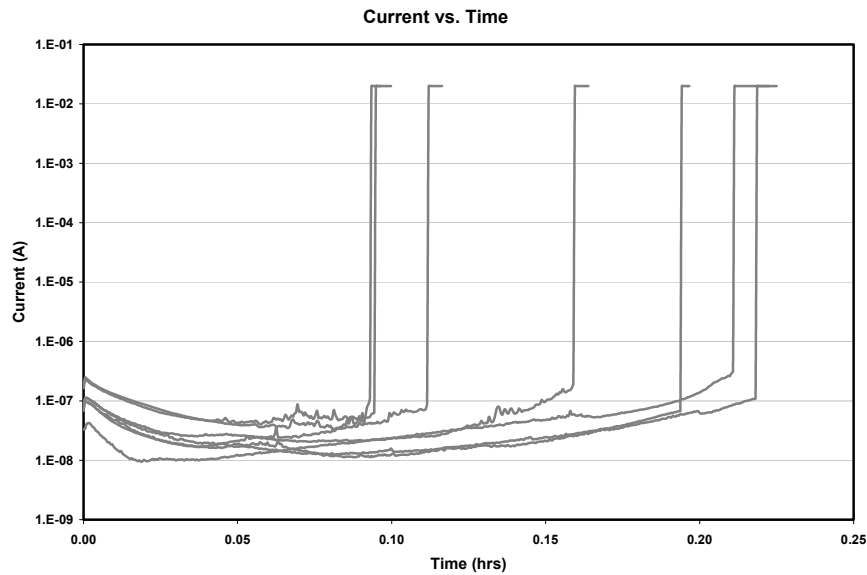


Figure 4.3 Representative current versus time plot showing hard breakdown

4.2 ELECTRICAL CHARACTERISTICS

The κ value, leakage current conduction mechanism, breakdown and time-dependent-dielectric breakdown of the four films were determined and compared.

4.2.1 Dielectric Constant

The dielectric constant was calculated from the measured capacitance at 100 kHz. The films were annealed at 100°C for 2.5 hrs and the κ value was measured again. Table 4.1 shows the κ values obtained for the four films.

k-value	Pre-Anneal (κ at RT, 100kHz)	Post-Anneal (κ at RT, 100kHz)
SiLK TM -D	2.60±0.03	2.53±0.03
pSiLK TM -V.9	2.40±0.03	2.39±0.04
pSiLK TM -U	2.29±0.03	2.21±0.05
pSiLK TM -Y	2.35±0.03	2.30±0.04

Table 4.1 Dielectric constant values of SiLKTM films

4.2.2 Ramp Voltage Breakdown

The RVB was determined for the four films. Fig 4.4 shows a representative JE plot showing the leakage current and breakdown characteristics at RT. Fig 4.5 shows the average breakdown field for all the dielectrics. The RVB test gives a quick assessment of the dielectric strength of the thin films.

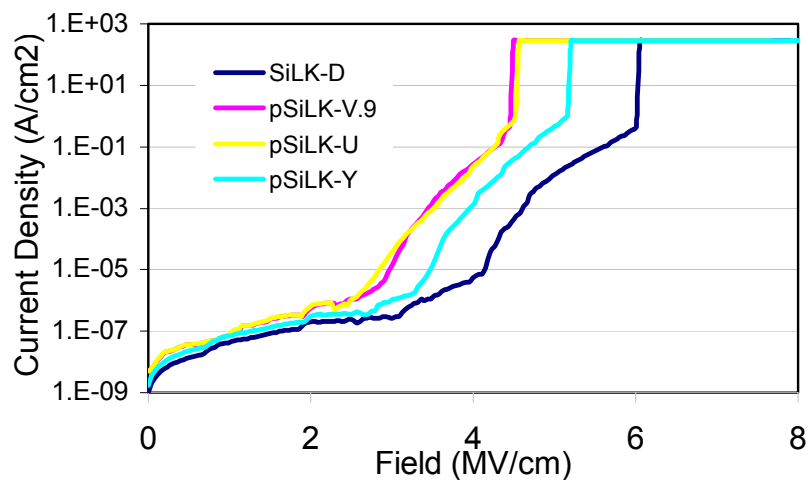


Figure 4.4 JE plot for SiLK™ films shows that there is Frenkel-Poole leakage at high fields

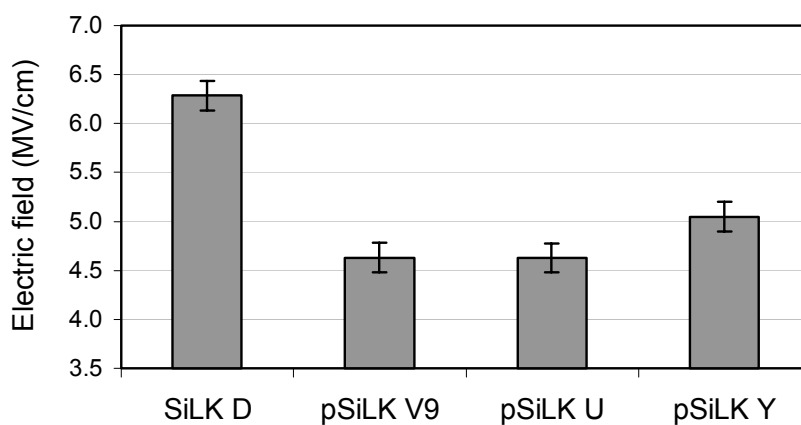


Figure 4.5 RVB for SiLK™ films shows that SiLK™-Y has a higher breakdown field compared to the other porous films

4.2.3 Conduction Mechanism

The JE curves at different temperatures were fit to different conduction mechanisms like Schottky, Frenkel-Poole and Ohmic. At lower fields Ohmic leakage was chosen instead of Schottky and Frenkel-Poole because Schottky and Frenkel-Poole gave improbable k-values. At higher fields the curves were fit to Frenkel-Poole.

Ohmic leakage occurs when thermally excited electrons hop from one isolated state to another. The current is exponentially dependent on temperature. Ohmic conduction is given by the equation,

$$J \sim E \exp [-\Delta E_{ae} / kT]$$

Where, J is the current density, E is the electric field and ΔE_{ae} is the activation energy for Ohmic conduction.

A plot of $\ln(J/E)$ vs. $1/T$ will yield a straight line from which the activation energy for Ohmic conduction can be calculated. Table 4.2 lists the Ohmic activation energies for all four dielectrics. The Ohmic activation energies are similar for the three porous dielectrics.

In Frenkel-Poole emission, current is carried by field enhanced thermally excited trapped electrons. As described in chapter 2, the Frenkel-Poole emission is given by the following equation,

$$J \sim E \exp [(-q(\phi_B - \sqrt{(qE/\pi\epsilon)}) / kT]$$

Where, J is the current density, T is the temperature in K, ϕ_B is the barrier height which is the Energy barrier for trap states, E is the electric field and ϵ is $\epsilon_0\epsilon_i$ which is the dielectric constant.

The Frenkel-Poole barrier lowering is given by the term, $\sqrt{(q E / \pi \epsilon)}$. A plot of $\ln(J/E)$ versus \sqrt{E} gives a straight line from which the barrier height, ϕ_B can be calculated. Frenkel-Poole leakage occurs at high temperatures and high fields. Fig 4.6 shows the Frenkel-Poole fit above 3MV/cm. Table 4.2 lists the Frenkel-Poole activation energies at 25°C for all four dielectrics. The Frenkel-Poole activation energies are similar for the three porous dielectrics.

The barrier heights and activation energies are higher for the dense SiLKTM film compared to the three porous films. The barrier heights and activation energies are similar for the three porous SiLKTM films. This indicates that the leakage conduction mechanisms are similar for all the porous dielectrics irrespective of the pore size or distribution. The conduction mechanism for all the films is Frenkel-Poole, which indicates that there are defect related trap states in the dielectrics.

	Ohmic Activation Energy (ev)	F-P Barrier Height $m^* = 0.42m$ (ev)
	E=0.5-3.0MV/cm	E>3.0MV/cm
SiLK TM -D	0.92±0.06	2.20±0.03
pSiLK TM -V.9	0.74±0.09	2.10±0.05
pSiLK TM -U	0.79±0.09	2.05±0.04
pSiLK TM -Y	0.84±0.07	2.08±0.07

Table 4.2 Ohmic activation energies and Frenkel-Poole barrier heights for SiLKTM films shows that the energies and barrier heights are similar for all the porous versions, which indicates that the conduction mechanism is similar irrespective of the pore-size or distribution

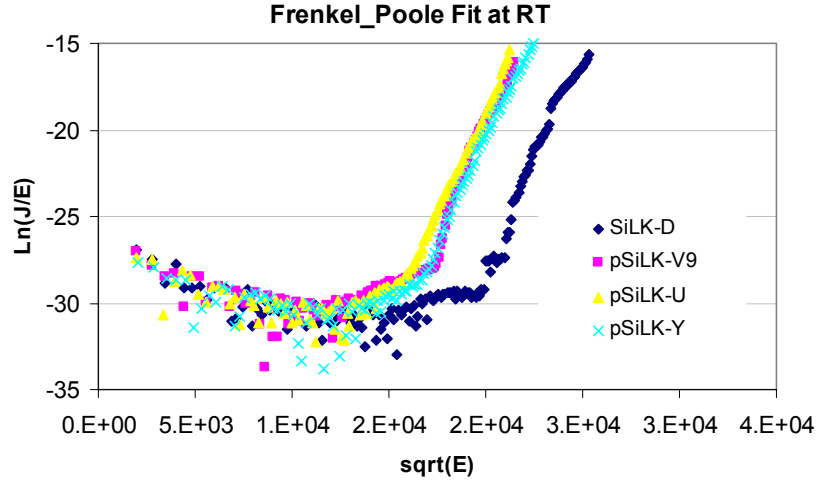


Figure 4.6 Frenkel-Poole fit at RT for SiLK™ films

4.2.4 Time dependent dielectric breakdown

TDDDB measurements were made at three different temperatures and at four different voltages. The electric fields were calculated from the actual thickness measured by both ellipsometry and cross-sectional SEM. The breakdown field distribution was fit to a Weibull distribution and the 63% value was taken for further calculations. Fig 4.7, 4.8, 4.9, 4.10 shows the failure distribution with Weibull fit at 300°C for the four dielectrics. Similar failure distributions were obtained at 275°C and 250°C. The Weibull shape parameter (β) was between 2.0 to 2.5 for all the fits. The data was fit to a thermo-chemical E-model (TCE model). The TCE model envisions a failure mechanism that depends

upon the molecular bond strength. Dielectric failure occurs due to molecular degradation. The time-to-fail (TTF) is given by,

$$\text{TTF} = A \text{ Exp } [(\Delta H_o^*)/(k_B T)] \text{ Exp } [-\gamma E]$$

$$\text{Ln (TTF)} \sim [(\Delta H_o^*)/(k_B T)] - \gamma E$$

Where, TTF is the Time to fail (sec), ΔH_o^* or E_a is the bond strength, k_B is the Boltzmann constant, T is the temperature in Kelvin, γ is the field acceleration parameter, E is the electric field across dielectric.

The 63% TTF data was plotted vs. electric field, at constant temperatures, to obtain the field acceleration parameter. Also the 63% TTF data, at constant fields, was plotted vs. $1000/T$ to obtain the enthalpy of activation (E_a). From this model we obtain a temperature dependent field-acceleration-parameter (γ) and a field dependent activation-enthalpy (E_a).

$$\gamma = A + B/T$$

$$E_a = \Delta H_o - mE$$

Fig 4.11 shows the 63% TTF vs. electric field at 300°C for all four dielectric films. Fig 4.12 shows the 63% TTF vs. $1000/T$ at 3.3 MV/cm for all four dielectric films. Fig 4.13 and 4.14 shows the 63% TTF vs. electric field for SiLKTM-D and pSiLKTM-Y respectively at different temperatures. Fig 4.15 shows the activation energy vs. the electric field. Fig 4.16 shows the field-acceleration-parameter vs. $1000/T$ for all four dielectric films. Tables 4.3 and 4.4 lists the field-acceleration-parameters and activation energies for all four dielectric films.

These plots show that the lifetime of the dense film is higher than all the porous films. And among the porous films SiLKTM-Y has a higher lifetime

compared to the other two. The activation energies and field acceleration parameters are comparable for all the porous films whereas the dense film has higher values.

The preceding analysis shows that there is a difference in leakage, breakdown and reliability characteristics among the porous SiLKTM films. Compositional analysis (Section 4.3), SEM (Section 4.4) and AFM analysis (Section 4.5) were done to determine the reason for the difference in electrical characteristics among the porous SiLKTM films.

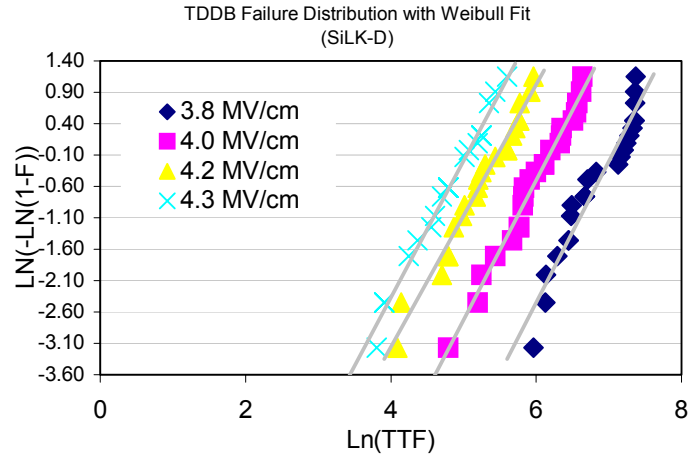


Figure 4.7 Weibull distribution of lifetime for SiLKTM-D shows higher lifetime for lower electric fields

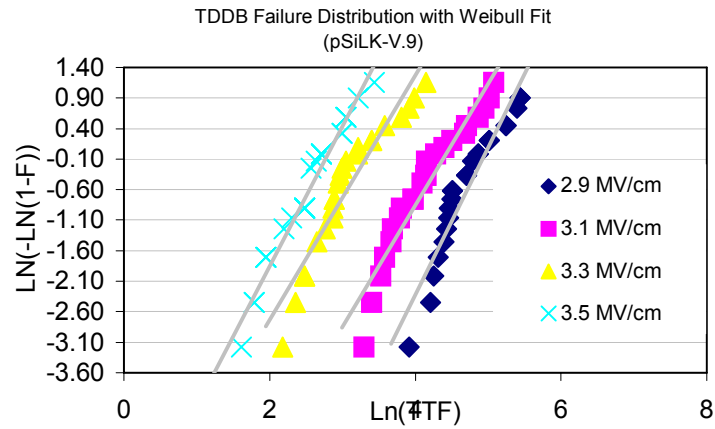


Figure 4.8 Weibull distribution of lifetime for SiLKTM-V.9 shows higher lifetime for lower electric fields

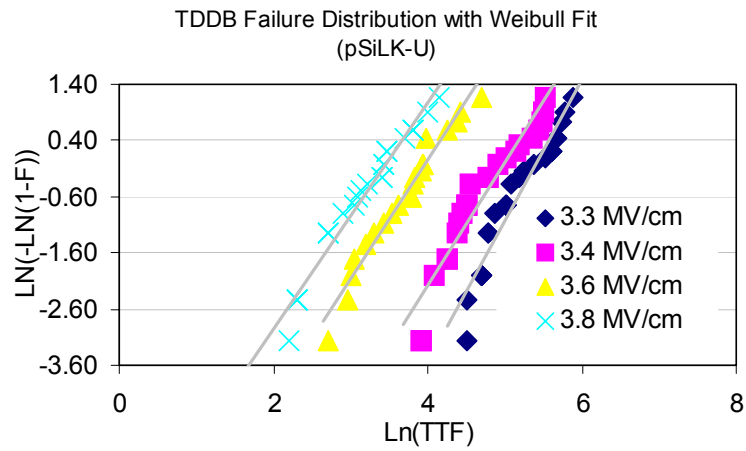


Figure 4.9 Weibull distribution of lifetime for SiLK™-U shows higher lifetime for lower electric fields

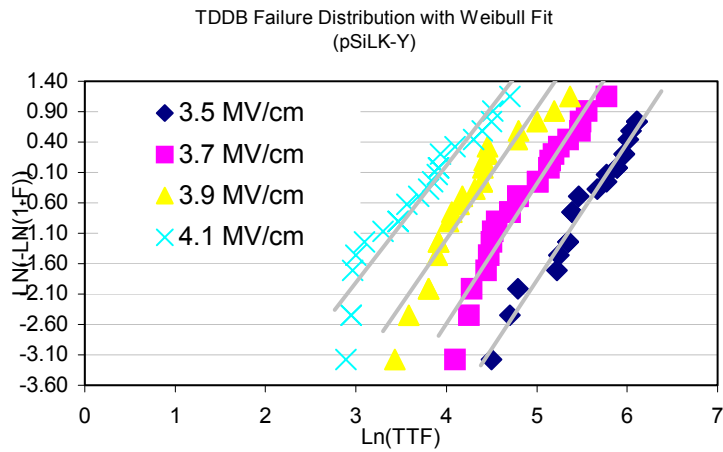


Figure 4.10 Weibull distribution of lifetime for SiLK™-Y shows higher lifetime for lower electric fields

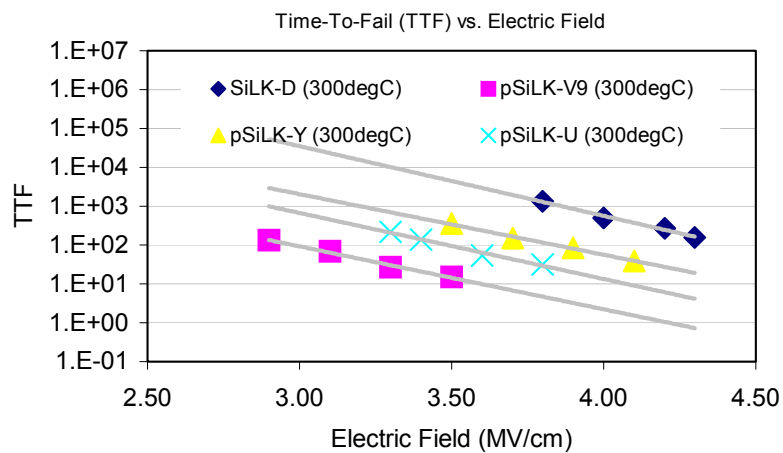


Figure 4.11 Time-to-fail versus electric field at 300°C for all four films shows that SiLK™-Y has a higher lifetime compared to the other porous films

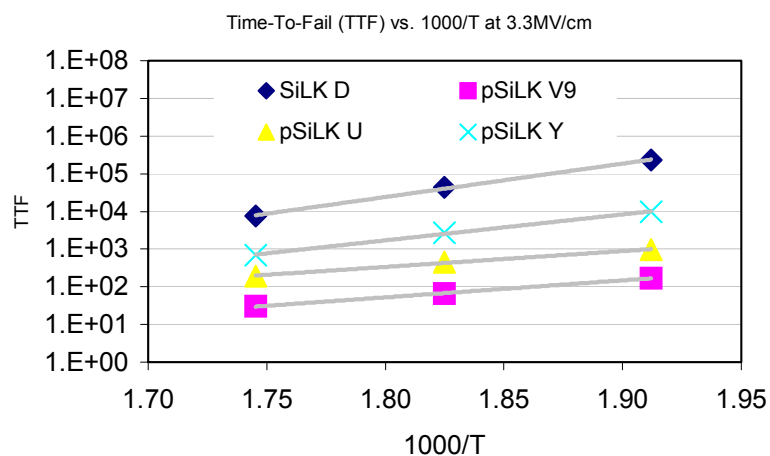


Figure 4.12 Time-to-fail versus 1000/T at 3.3MV/cm for all four films shows that SiLK™-Y has a higher lifetime compared to the other porous films

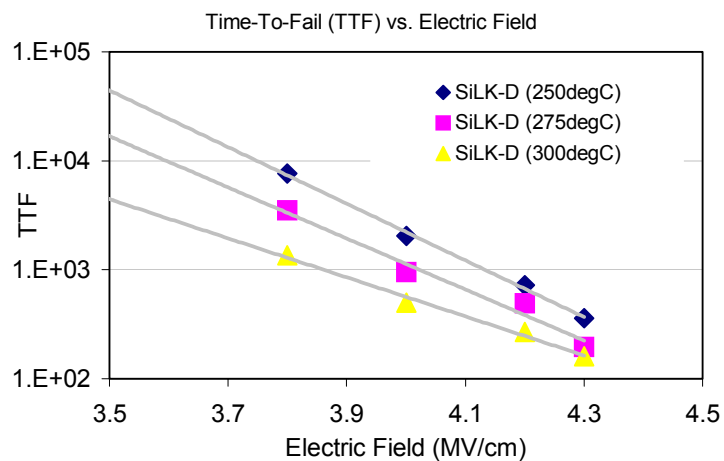


Figure 4.13 Time-to-fail versus electric field for SiLK™-D shows that higher temperatures gives lower lifetimes

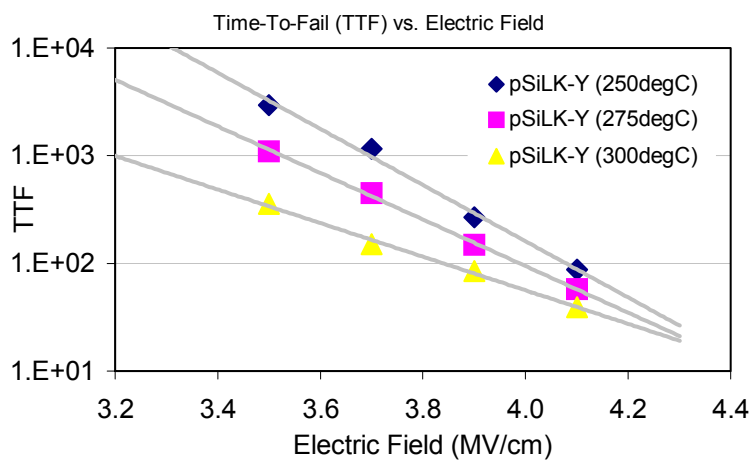


Figure 4.14 Time-to-fail versus electric field for SiLK™-Y shows that higher temperatures gives lower lifetimes

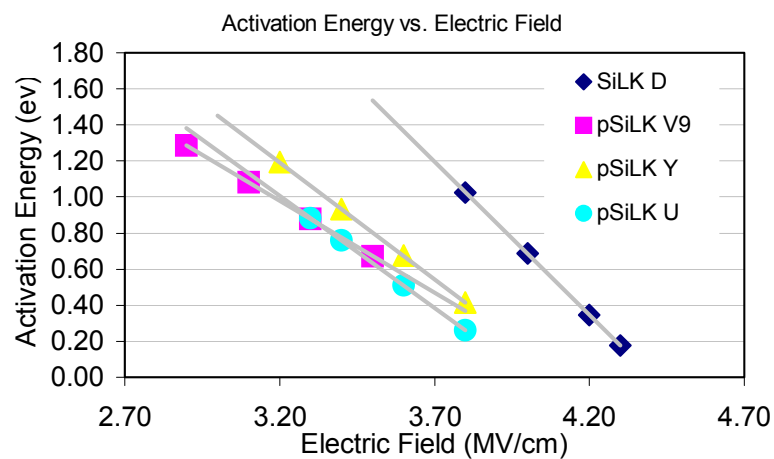


Figure 4.15 Activation energy versus electric field for all four films shows that SiLKTM-Y has slightly higher activation energies compared to the other porous films

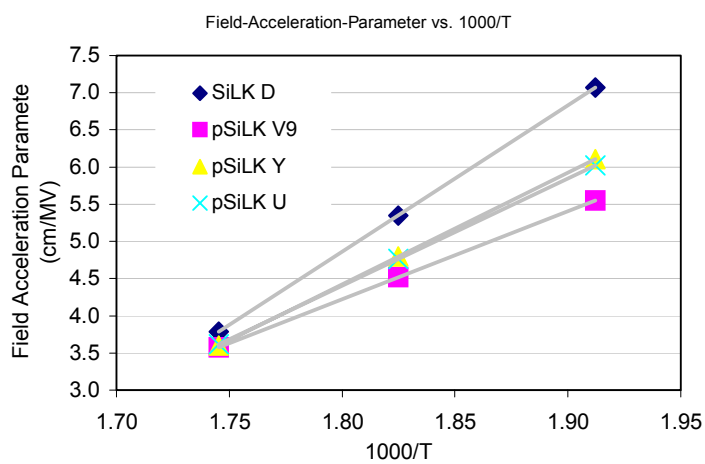


Figure 4.16 Field acceleration parameter versus 1000/T for all four films shows that SiLKTM-V.9 has slightly lower acceleration parameters compared to the other porous films

Field-Acceleration-Parameter (γ)	250°C (cm/MV)	275°C (cm/MV)	300°C (cm/MV)
SiLK TM -D	7.07±0.07	5.35±0.06	3.78±0.05
pSiLK TM -V.9	5.55±0.06	4.52±0.07	3.58±0.06
pSiLK TM -U	6.02±0.06	4.77±0.05	3.62±0.04
pSiLK TM -Y	6.11±0.07	4.80±0.06	3.60±0.05

Table 4.3 Field acceleration parameters for all four films

Activation Energy Ea (ev)	Ea at 3.6 MV/cm (Experimental)	Ea at 1.0 MV/cm (Extrapolated)	Ea at 0.1 MV/cm (Extrapolated)
SiLK TM -D	1.37±0.03	5.78	7.31
pSiLK TM -V.9	0.57±0.04	3.22	4.13
pSiLK TM -U	0.51±0.04	3.74	4.86
pSiLK TM -Y	0.67±0.03	4.05	5.22

Table 4.4 Activation energies for all four films

4.3 SPECTRAL ANALYSIS

The chemical structures of the SiLKTM films were determined from FTIR analysis. Fig 4.17 shows the FTIR spectra of all the four dielectric films. The wave number in FTIR spectroscopy is the frequency of vibration divided by the speed of light. Dow Chemical SiLKTM is an organic material with an aromatic hydrocarbon structure [Martin (2000)]. Cyclopentadienone- and acetylene-containing monomers are reacted to form polyphenylenes. Cross-linked polyphenylene systems are formed after curing. SiLKTM-D is a dense version while the SiLKTM-V.9, SiLKTM-U and SiLKTM-Y are porous versions of SiLKTM. The FTIR spectrum suggests ring structures and substituted cyclopentadienone (C₅H₄O) molecules.

All the films are compositionally very similar. The dense version had higher concentration of all peaks, as it is expected, but there is no apparent difference between all the porous versions. Although the films were porous they do not exhibit any moisture peaks, which indicate that the low- κ material is hydrophobic and resistant to ambient moisture. The Si-O-Si stretching peak is due to the thin layer of SiO₂ in the dielectric stack beneath the SiLKTM films and is not indicative of Si-O in the films. The similarity of the composition of the porous films indicates that the varying electrical properties are not due to compositional differences.

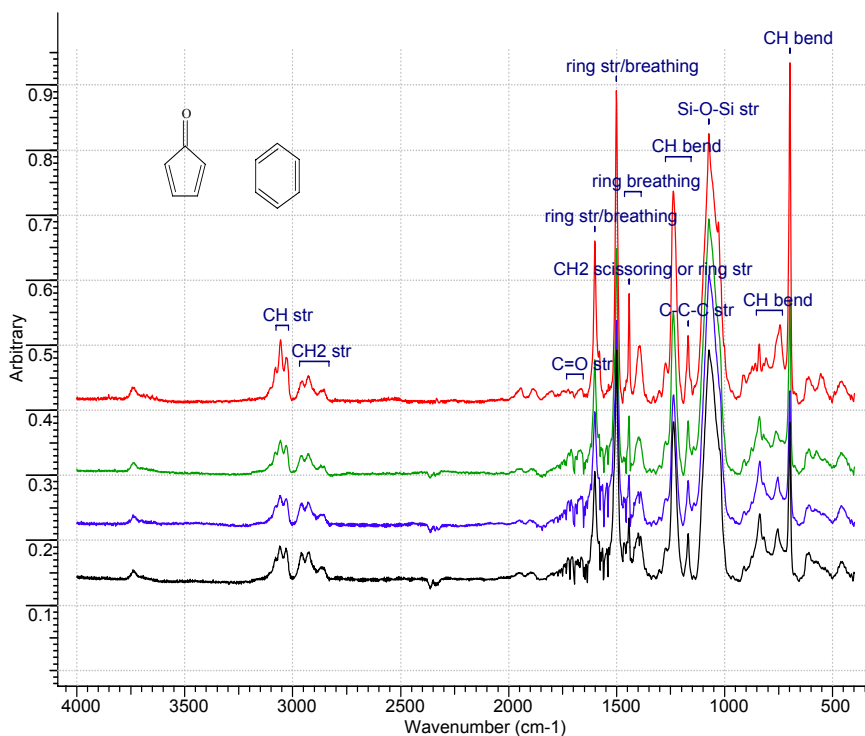


Figure 4.17 FTIR absorbance spectra for SiLK™ films shows the typical benzene ring as well as other organic bond signatures

4.4 CROSS-SECTIONAL SEM

The four low- κ films were cross-sectioned and observed under the SEM. Fig 4.18, 4.19, 4.20 and 4.21 shows the SEM micrographs of all four films. The SEM analysis of SiLK™-V.9 indicates that it has large pores and also a wider distribution of pore size. It is also observed that the interface between the SiLK™-V.9 film and the SiO₂ layer is rough.

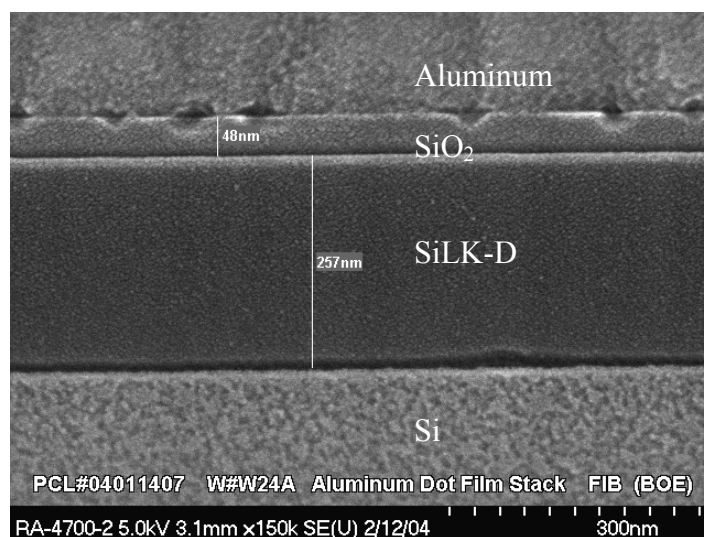


Figure 4.18 SEM micrograph of SiLKTM-D shows a dense film

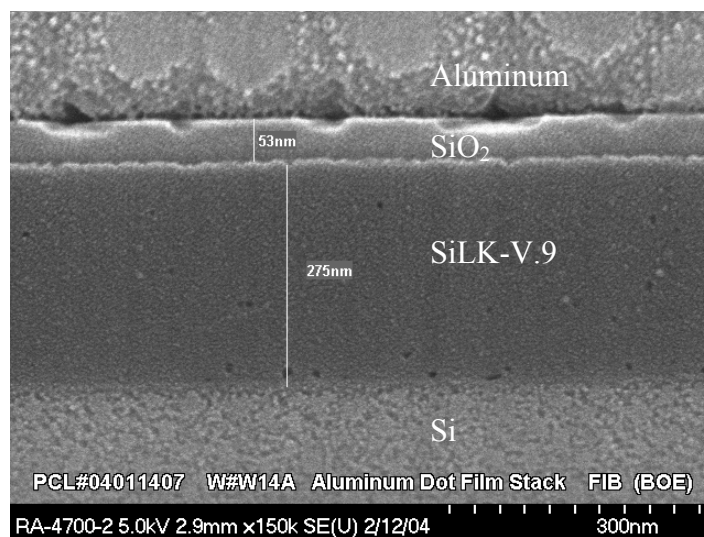


Figure 4.19 SEM micrograph of SiLKTM-V.9 shows a film with interfacial roughness and pores of large sizes

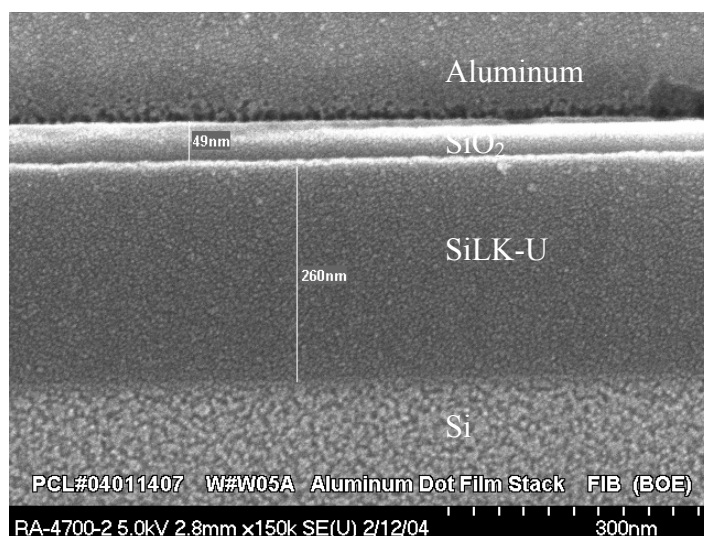


Figure 4.20 SEM micrograph of SiLK™-U does not show any large pores

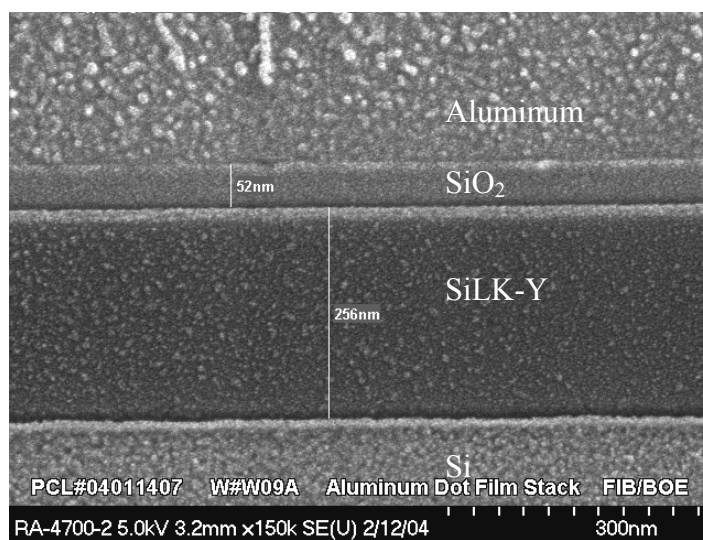


Figure 4.21 SEM micrograph of SiLK™-Y does not show any large pores

4.5 ATOMIC FORCE MICROSCOPY

The roughness of the four SiLKTM films was determined by AFM. Artifacts may show up due to tip wear. Hence new tips were used for each analysis. The scanner may cause tilt, bow or wave in the image. So appropriate flatten and plane fit filters were applied to the images. Fig 4.22, 4.23, 4.24, and 4.25 shows the roughness for all the four films and Table 4.5 summarizes them all. Ra is the average roughness, which is the average of each point's vertical deviation from the average height. Rrms is the root mean square roughness, which is the square root of the sum of the squares of each point's vertical deviation from the average height divided by the number of points. And Rmax is the difference between the highest and lowest point within the captured area.

500nm Scan	Ra	Rrms	Rmax
SiLKTM-D	3.08	3.86	29.82
SiLKTM-U	6.00	7.51	62.46
SiLKTM-Y	5.82	7.24	61.56
SiLKTM-V.9	10.61	13.43	104.06

Table 4.5 AFM surface roughness in Å for SiLKTM films shows that SiLKTM V.9 is twice as rougher than the other porous films

The roughness data shows that the porous films SiLKTM-U and SiLKTM-Y are about twice as rough as the dense film. Whereas, the film SiLKTM-V.9 is about four times rougher than the dense film.

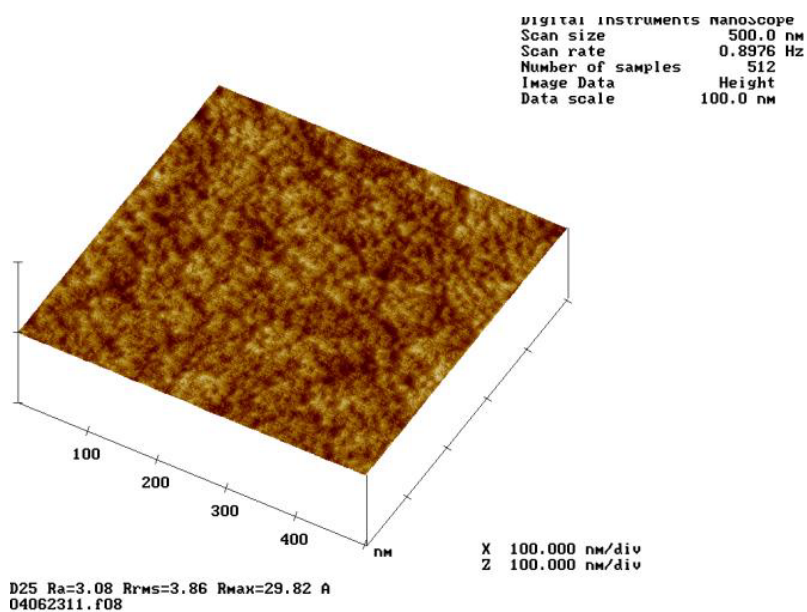


Figure 4.22 AFM micrograph of SiLK™-D

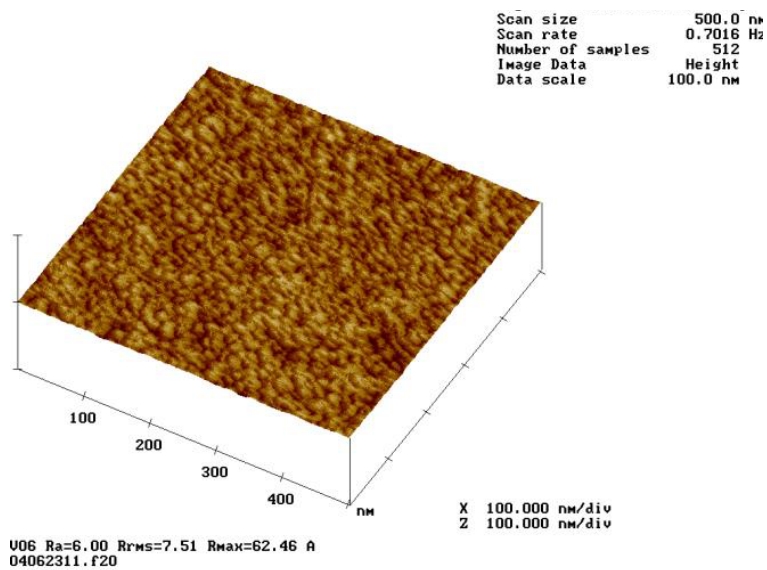


Figure 4.23 AFM micrograph of SiLK™-U

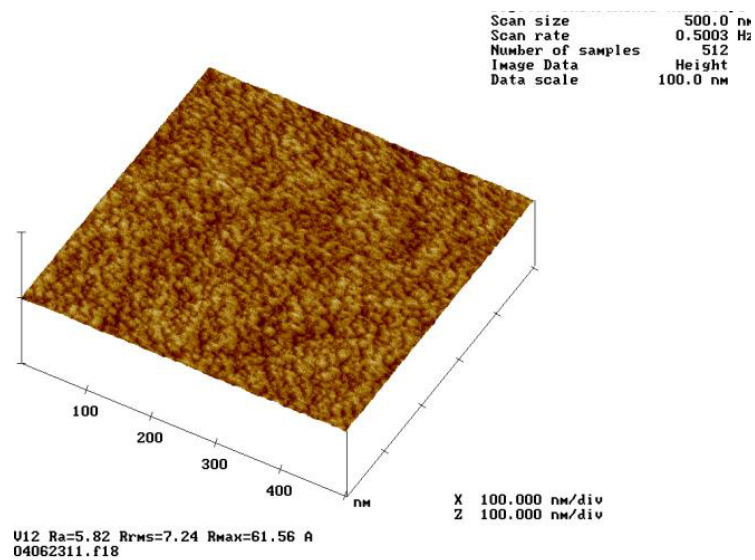


Figure 4.24 AFM micrograph of SiLK™-Y

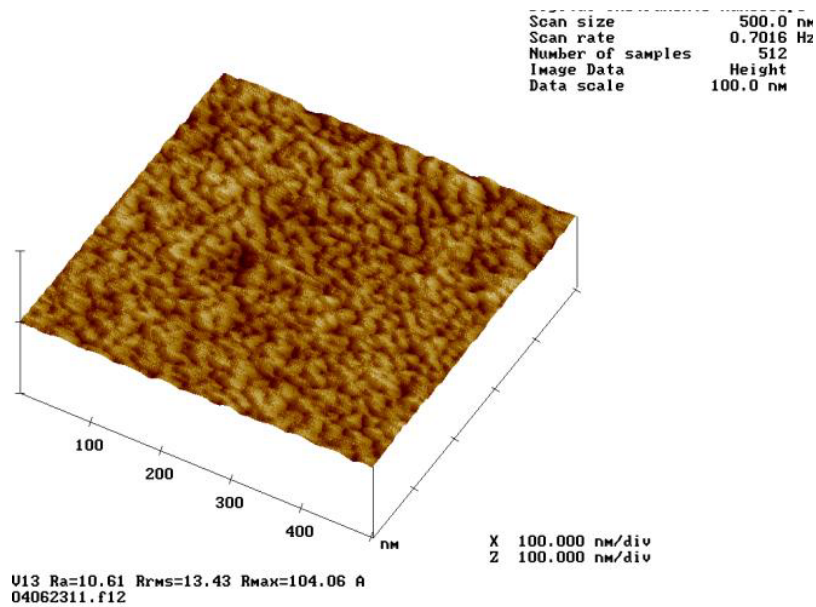


Figure 4.25 AFM micrograph of SiLK™-V.9

4.6 ESTIMATION OF ROUGHNESS AND DEFECT DENSITY

The AFM analysis as well as cross-sectional SEM indicated that the roughness of the SiLKTM-V.9 films is highest among the porous films. This film also has a large and wide distribution of pores. The comparatively poor electrical performance of the SiLKTM V.9 films may be due to the enhancement of electric field caused by the rough interface. In this segment an estimate will be made to determine the amount of roughness that will cause the observed difference in reliability lifetimes.

Fig 4.26 shows a schematic of the effective electric field due to a rough interface indicated by ΔX [Lee (1988), Tanaka (1993)]. The average thickness is given by X . The average electric field is E and the intensified electric field is E' .

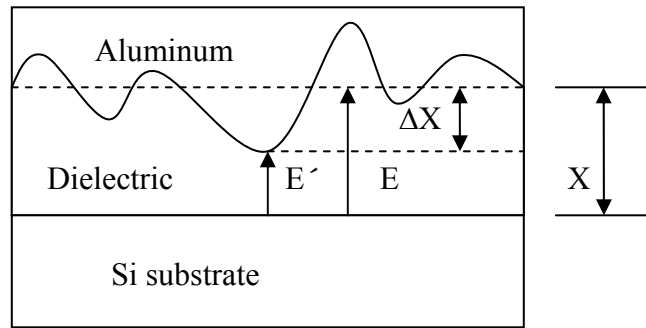


Figure 4.26 Schematic of interfacial roughness showing the intensified electric field (E') due to the rough interface

The TTF at 3.60 MV/cm at three different temperatures for the four dielectrics are plotted versus the roughness values that were measured by AFM (Fig 4.27). The plot shows that the lifetime decreases for increasing roughness. An estimate will be made to determine if roughness can account for the difference in lifetimes for all the films.

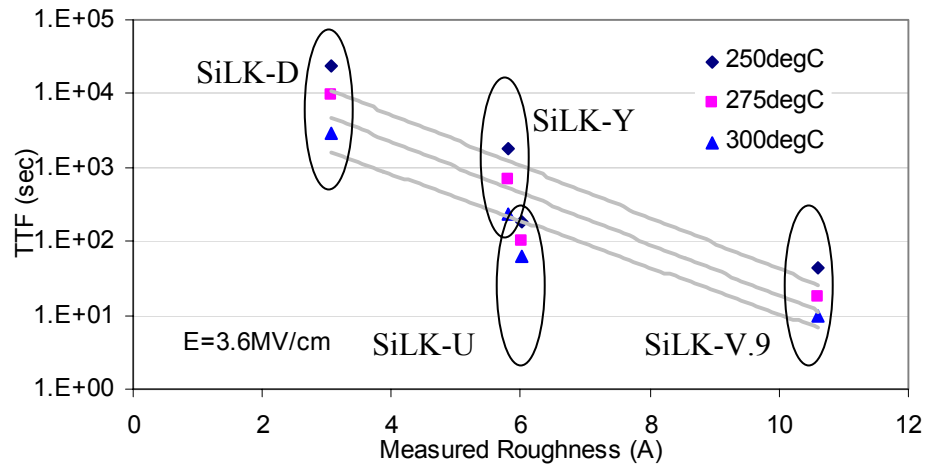


Figure 4.27 Time-to-fail versus the measured roughness for the SiLK™ films shows that the lifetime is lower for higher roughness

The TTF can be written as,

$\ln(\text{TTF}) = -\gamma E + A$, where γ is the field acceleration parameter, E is the average electric field and A is a constant.

We assume that the increase in roughness caused an increase in electric field. The $\ln(\text{TTF})$ at roughness (ΔX) equal to zero is determined from Fig 4.27 for 300°C. The constant A is then calculated.

Assuming that the film with a larger ΔX will breakdown faster, we can calculate E' from the following equation,

$\ln(\text{TTF}) = -\gamma E' + A$, where γ is the field acceleration parameter, E' is the intensified electric field and A is a constant.

From the TTF versus electric field plots, a field acceleration parameter (γ) of 4.0 cm/MV was assumed for further analysis and ΔX was determined from the following equation,

$$\Delta X = X (1 - E/E')$$

The calculated roughness (ΔX) is then plotted versus the measured roughness (Fig 4.28).

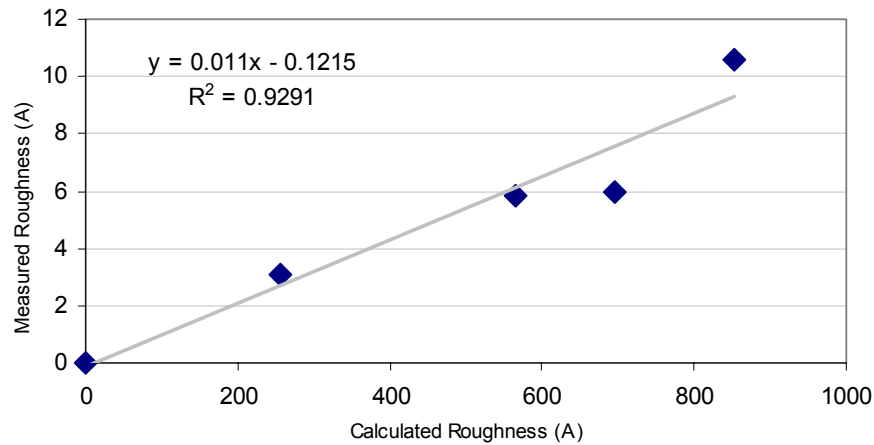


Figure 4.28 Measured roughness versus the calculated roughness shows that the roughness will have to be about 100 times greater than the calculated value to increase the electric field to a value large enough to explain the difference in lifetimes

The plot shows that the calculated roughness of the interface is about 100 times more than the measured value. It is unreasonable to expect such a high roughness of the dielectric films. Therefore, roughness alone cannot explain the difference in lifetimes for the four dielectric films.

The difference in lifetime can be better explained on the basis of critical defect density required for breakdown [Degraeve (1988)]. When a dielectric is electrically stressed, defects form randomly within the material. The defect density increases as stress time increases. Ultimately the dielectric will break down when there is a path of percolation from one end to the other. It is assumed that a critical defect density (N_{bd}) will be required to create a path of easy conduction through the dielectric. The lifetime of the device will depend upon this N_{bd} as well as the defect generation rate. The charge to breakdown (Q_{bd}) is the total cumulative charge flowing through a dielectric until breakdown occurs. It is directly related to the N_{bd} .

$Q_{bd} = N_{bd} / P_{gen}$ where, P_{gen} is the defect generation rate.

The Q_{bd} is compared between the SiLKTM films in Fig 4.29. From the figure we see that the Q_{bd} for SiLKTM-V.9 is lower than that of SiLKTM-Y, which in turn is lower than SiLKTM-D.

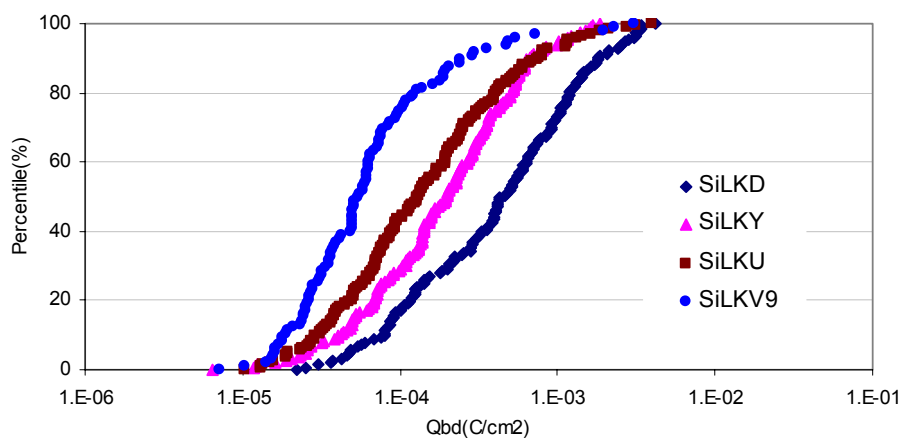


Figure 4.29 Percentile plot of Qbd for SiLK™ films shows that the SiLK™-V.9 films have a lower Qbd compared to the other porous films

Fig 4.30 shows a plot with Qbd versus the tbd. This plot shows that the lower value of the Qbd translates into shorter lifetimes.

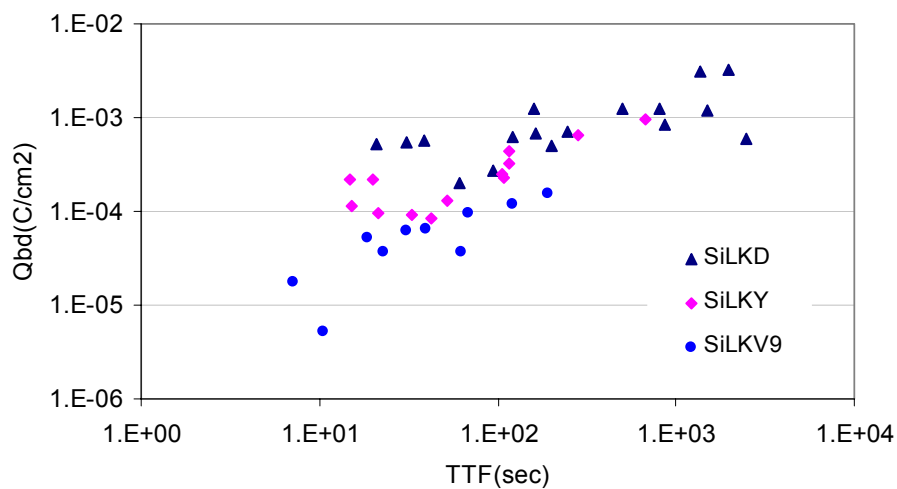


Figure 4.30 Qbd versus tbd for SiLK™ films shows that the SiLK™-V.9 film has lower Qbd and lower tbd compared to the other porous SiLK™ films

An estimation of the defect density can be made by a simple analysis. We consider the charge per unit area. A Qbd value of $1 \times 10^{-4} \text{ C/cm}^2$ is taken as a reliability criterion. The number of samples that has a Qbd greater or less than $1 \times 10^{-4} \text{ C/cm}^2$ is determined. An exponential distribution functions is considered [Michalka (1990)]. An exponential distribution function assumes that the high defect densities are increasingly unlikely.

The yield is given by Murphy's formula.

$$Y = \int_0^{\infty} e^{-DA^c} f(D) dD$$

Where Y is the yield, D is the defect density in defects per cm^2 , A^c is the critical defect area, which we approximate as equal to the actual area (A) and $f(D)$ is the defect distribution function.

If we assume that the defect distribution function $f(D)$ is exponential then the yield is given by,

$$Y = Y_0 / [1 + DA]$$

Where D is the defect density in defects/ cm^2 and A is the area in cm^2 .

The yield of each SiLKTM sample is calculated. The defect density is then calculated assuming an area of 0.007 cm^2 . Fig 4.31 shows the defect densities calculated from an exponential distribution function.

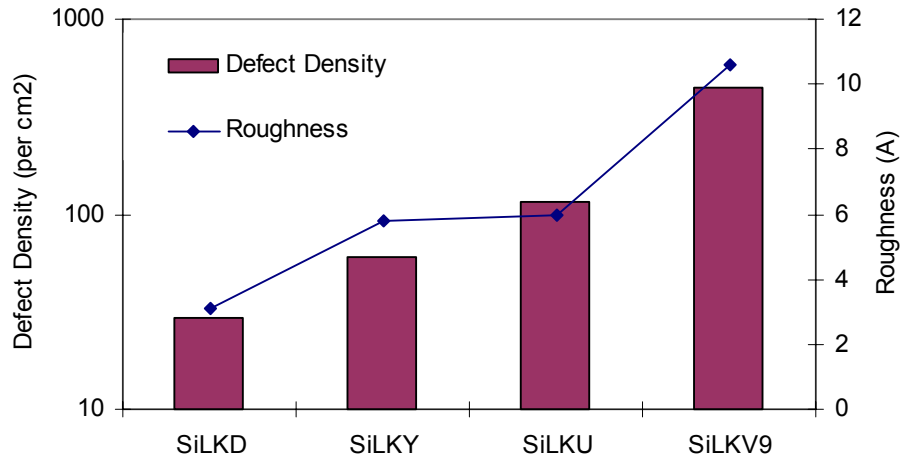


Figure 4.31 Defect density and roughness for SiLK™ films shows that the defect density increases for a rougher film

From the above analysis we see that the defect density of SiLK™-V.9 is about 7 times larger than SiLK™-Y, the defect density of SiLK™-U is about 2 times larger than SiLK™-Y and the defect density of SiLK™-Y is about 2 times larger than SiLK™-D.

If we assume that the critical defect density and the defect generation rate are constant for these films, then a lower Qbd implies that there are pre-existing defects in the dielectric. As a result it takes a shorter time to accumulate the additional defects required for percolation to occur. An estimate of the defect density shows that the SiLK™-V.9 has 7 times more defects than the SiLK™-Y film. Therefore we can infer that the higher roughness of SiLK™-V.9, due to the larger pore size and distribution, creates more defects at the interface. As a result the lifetime of the SiLK™-V.9 film is lower than the other SiLK™ films.

4.7 DISCUSSION

The four different SiLKTM dielectric films differ in the size of pores and distribution of pores. The purpose of this study was to determine and understand the electrical characteristics of the four different versions of SiLKTM. The FTIR analysis showed that there was not much difference in the chemical constituents among the three porous SiLKTM films.

The current conduction mechanism is Frenkel-Poole for all the four SiLKTM versions. This indicates that there are defect states present at or near the interface in the dielectrics. As discussed in Chapter 2, the weakest bonds in SiLKTM are O-O and Si-C which exist at the interface. The Frenkel-Poole leakage for SiLKTM is due to the defect states created by the Si-C or O-O bonds near the interface. There can also be pre-existing defects in the dielectric which would contribute charge to the total current.

The barrier heights and activation energies for current conduction are higher for the dense SiLKTM film compared to the three porous films. The barrier heights and activation energies are similar for the three porous SiLKTM films. This indicates that the leakage conduction mechanisms are similar for all the porous dielectrics irrespective of the pore size or distribution.

AFM analysis as well as cross-sectional SEM indicated that the roughness of the SiLKTM-V.9 films is highest among the porous films. This film also has a larger and wider distribution of pores. There will be localized field enhancement at the rough interface of SiLKTM-V.9. However, roughness alone cannot account for the difference in lifetime between the porous SiLKTM films. Roughness alone

is not enough to increase the electric field to an extent that the lifetime will be lowered to the values that were experimentally observed.

The difference in lifetimes is due to the higher initial defect density of the SiLKTM-V.9 film. The higher defect density is implied from the Qbd comparisons. Assuming that the critical defect density and defect generation rates are constant for all the films, the SiLKTM-V.9 film has a lower Qbd and hence a higher initial defect density. An estimate of the defect density shows that the SiLKTM-V.9 sample has 7 times more defects than the SiLKTM-Y sample. The higher initial defect density is due to structural damage caused by the high interfacial roughness. The higher interfacial roughness is due to the larger pore size and distribution of the SiLKTM-V.9 films.

SiLKTM-Y has a tighter distribution of pore-size than SiLKTM-U. It also shows better lifetime characteristics and slightly lower roughness compared to SiLKTM-U. It also has lower initial defect density and as a result the Qbd as well as the lifetimes are higher.

The reduction in pore size reduces the roughness at the interface as indicated by SiLKTM-U and SiLKTM-Y. This also translated into better reliability characteristics. A tighter distribution of pores (SiLKTM-Y) gave the best reliability among the porous SiLKTM films.

The leakage and conduction and subsequent reliability of these films depend largely on the interface. Large pore sizes give higher interfacial roughness, which causes localized field enhancements and higher defect densities, which ultimately results in poor electrical performance. The use of pores as a

means to reduce the k-value must take into account the deleterious effect of field enhancements at the interface. Also etching and ashing can cause further damage to the interface. The gases and chemicals used in etching, ashing and cleaning can enter into the open pores and poison the dielectric. Smaller pore-size can reduce these effects to an extent. Pore sealing is another way to protect the exposed interface of the porous dielectric.

Chapter 5: Processing Effects on Blanket Low- κ Films

In this chapter the effects of surface processing on a low- κ film will be discussed. The low- κ film under investigation is an MSQ type. Firstly the processing condition and test structure will be described. Secondly, the electrical tests and results will be presented and finally, FTIR spectral analysis will be discussed.

5.1 SAMPLES AND EXPERIMENTAL SETUP

Fig 5.1 shows a schematic of the test structure used to perform the electrical tests. The low- κ dielectric is an MSQ type of material. The low- κ was partially etched and ashed and treated with hexamethyldisilazane (HMDS) vapor. The complete experimental splits are shown in Table 5.1. The etching recipe consisted of $C_4H_8/Ar/N_2$ in the ratio 6/1000/150 sccm respectively. The process time was 12 seconds. The plasma ashing was done with N_2 and H_2 gas for 30 seconds. The annealing was done in a furnace for 30 minutes at $400^\circ C$ in a forming gas mixture. The HMDS treatment is done in three steps. First, a pre-bake was done at $120^\circ C$ for 60 seconds. In the second step the wafers are treated to HMDS vapor at $145^\circ C$ for 60 seconds. Finally, a post-bake is performed at $180^\circ C$ for another 60 seconds.

The thicknesses of the films were determined optically by measuring the refractive index. The dielectric constant was calculated from capacitance measurements. The capacitors were defined using shadow masks. Aluminum was deposited by sputtering at a high vacuum of $<3 \times 10^{-7}$ Torr. Leakage currents were measured by sweeping voltage at a constant ramp rate of 3V/sec. The

measurements were made using an Agilent 4156 semiconductor parametric analyzer and HP4284 LCR meter. The samples were also baked at 100°C for 2.5 hours and leakage currents and capacitances were measured both pre-bake and post-bake.

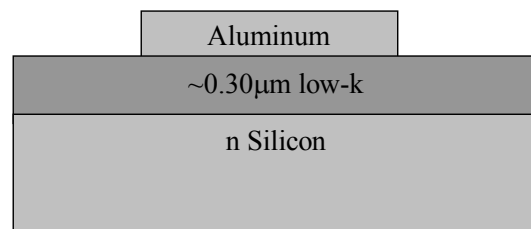


Figure 5.1 Schematic of test structure for electrical tests

	1	2	3	4	5	6	7	8
4.5nm Thermal oxide	X	X	X	X	X	X	X	X
300nm LKD	X	X	X	X	X	X	X	X
Partial Etch/Partial Ash		X	X	X	X	X	X	X
DI Water Rinse			X	X	X	X	X	X
Anneal, 400C, 30min, FG				X	X	X		
HMDS					X	X	X	X
Anneal, 400C, 30min, FG						X		X
Thickness Measurements	X	X	X	X	X	X	X	X
<p>X = Means do</p> <p>Filled = means can't do, wafer is removed</p> <p>No Fill or Blank = Means don't do</p>	Unetched	Etched/Ashed	DI	DI+Anneal	DI+Anneal+HMDS	DI+Anneal+HMDS+Anneal	DI+HMDS	DI+HMDS+Anneal

Table 5.1 Experimental split of thermo-chemical processes

5.2 ELECTRICAL CHARACTERIZATION

The κ value and leakage current of the capacitors was determined and the different recovery processes were compared.

The dielectric constant was determined at 100 kHz from capacitance measurements. Fig 5.2 shows the κ values both pre-bake and post-bake for all the splits. Etching and ashing of the film increases the κ value drastically. The thermal and chemical recovery processes are successful in recovering the κ value to an extent, but the κ value is not fully recovered.

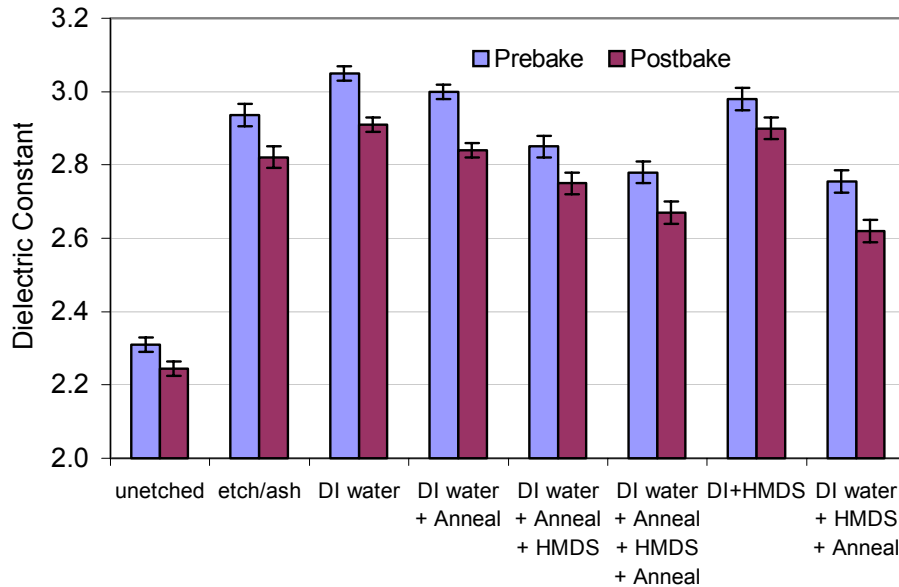


Figure 5.2 Dielectric constant of the different treatments shows the increase in κ value due to etching and ashing and the recovery of κ value by the various surface treatments

Annealing helps in reducing the κ value but a chemical treatment followed by an anneal further reduced κ to a lower value.

The leakage current was also determined both pre-bake and post-bake. Fig 5.3 shows the typical leakage curves for a few selected treatments. Fig 5.4 and 5.5 shows the leakage currents at 0.1MV/cm and 1.0MV/cm for all the treatments.

The capacitor leakage current follows the same trend as the κ value. The etching and ashing increases the leakage by about an order of magnitude. The various thermal and chemical recovery processes reduce the leakage current to an extent, but they are unable to completely reduce the leakage to its initial unetched state.

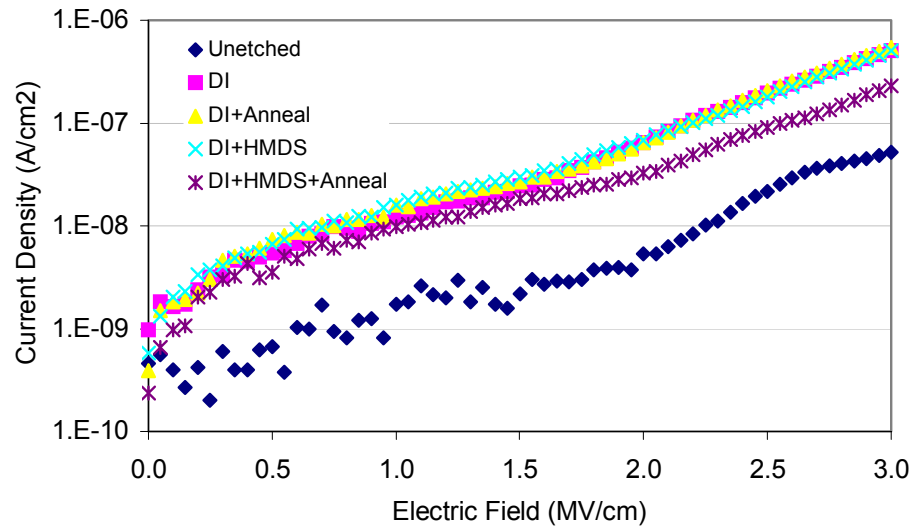


Figure 5.3 Typical leakage currents for the different treatments shows the increase in leakage due to the etching and ashing and the recovery of the leakage by the surface treatments

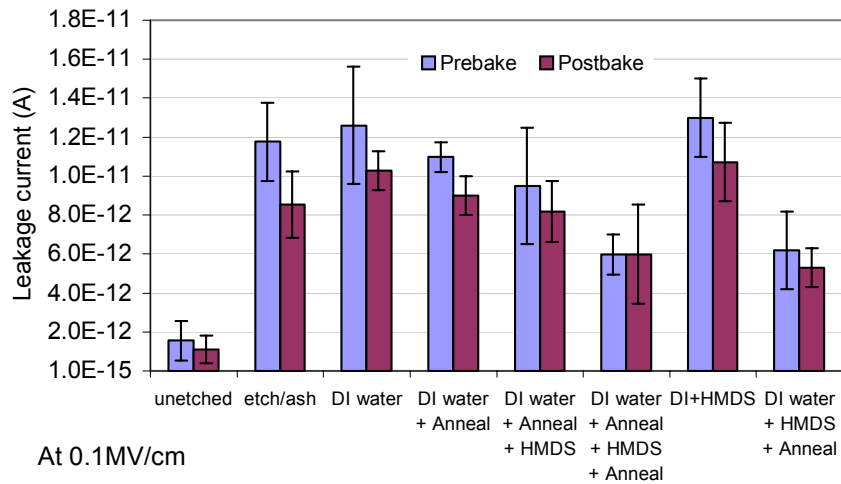


Figure 5.4 Leakage current at 0.1 MV/cm for different treatments shows the increase in leakage due to the etching and ashing and the recovery of the leakage by the surface treatments

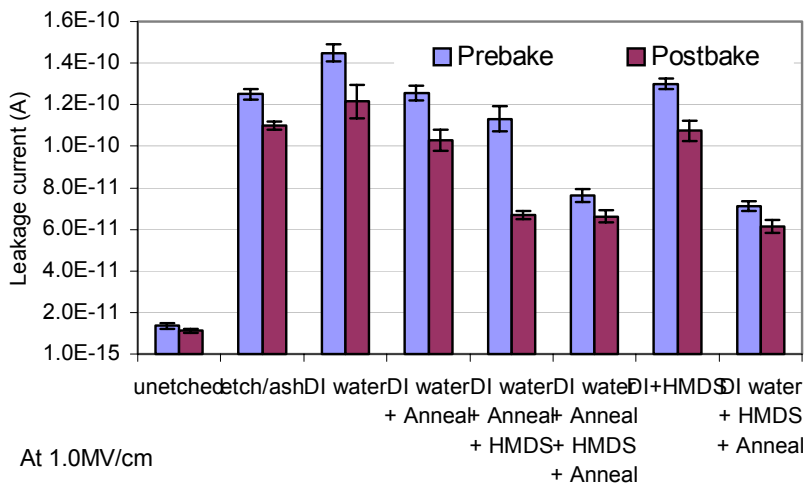


Figure 5.5 Leakage current at 1.0 MV/cm for different treatments shows the increase in leakage due to the etching and ashing and the recovery of the leakage by the surface treatments

5.3 FTIR ANALYSIS

The etching and ashing processes increase the κ value and the leakage of the dielectric films. These processes alter the chemical structure of the low- κ material. Fourier transform infra-red spectroscopy (FTIR) is a useful characterization technique to determine the molecular changes occurring in the dielectric film due to the processing conditions as well as the later recovery steps. Nuclear magnetic resonance spectroscopy (NMR) is another useful tool. NMR has the capability to distinguish configurations of silicon with different methyl concentrations [Mabboux and Gleason (2005)]. In this study only FTIR analysis will be discussed.

The SiO_4 tetrahedron is the primary structural unit in all solid forms of SiO_2 [Helms (1994), McPherson (2001)]. The bond angle between O-Si-O is 109° . The bond angle between the corner oxygen atoms to the nearby silicon atoms can range from 120° to 180° depending upon the chemical composition of the dielectric.

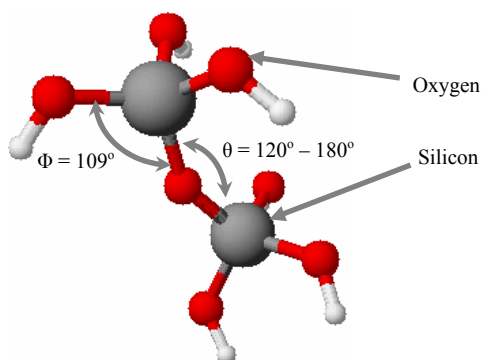


Figure 5.6 Schematic of Si-O-Si bond angle shows the bond angle between Si-O-Si could range from 120° to 180°

The absorbance spectrum of the dielectric film shows the typical bonds of an MSQ type of material. There is the characteristic Si-CH₃ umbrella peak around 1276 cm⁻¹ and there are also the Si-O-Si asymmetric stretching peaks around 1100cm⁻¹ and CH₃ stretching peaks around 3400cm⁻¹. There are also the water and Si-OH stretching peaks around 3600cm⁻¹ and the Si-OH bending peak around 950cm⁻¹.

The asymmetric Si-O-Si peaks around 1100cm⁻¹ can be deconvoluted into three peaks [Grill (2003)]. The peak around 1030cm⁻¹ can be attributed to the network sub-oxide (Si-O-Si angle <140°) stretching. The peak around 1060cm⁻¹ can be attributed to the silicon dioxide network (Si-O-Si angle ~140°) stretching and the peak around 1130cm⁻¹ can be attributed to the silicon dioxide cage structure (Si-O-Si angle ~150°) stretching. The presence of these three peaks is due to the structural constraint and chemical changes in the lattice of silicon dioxide due to the presence of carbon, hydrogen and oxygen bond groups (CH₃, CH₂, CH, OH).

The various peaks were deconvoluted using a Gaussian curve fit. The Gaussian peak fit (Fig 5.7 and Fig 5.8) clearly shows a decrease in the cage and sub-oxide peaks and an increase in the network peak due to the etching and ashing of the MSQ film. There is also a reduction in the Si-CH₃ peak.

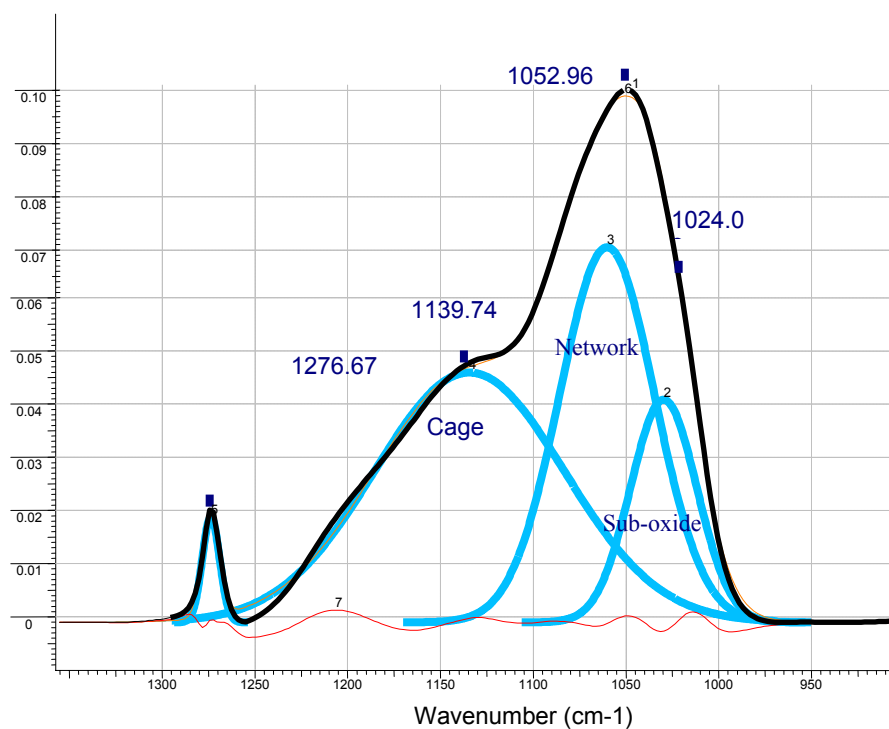


Figure 5.7 Gaussian peak analysis of unetched samples shows the cage, network and sub-oxide peak areas

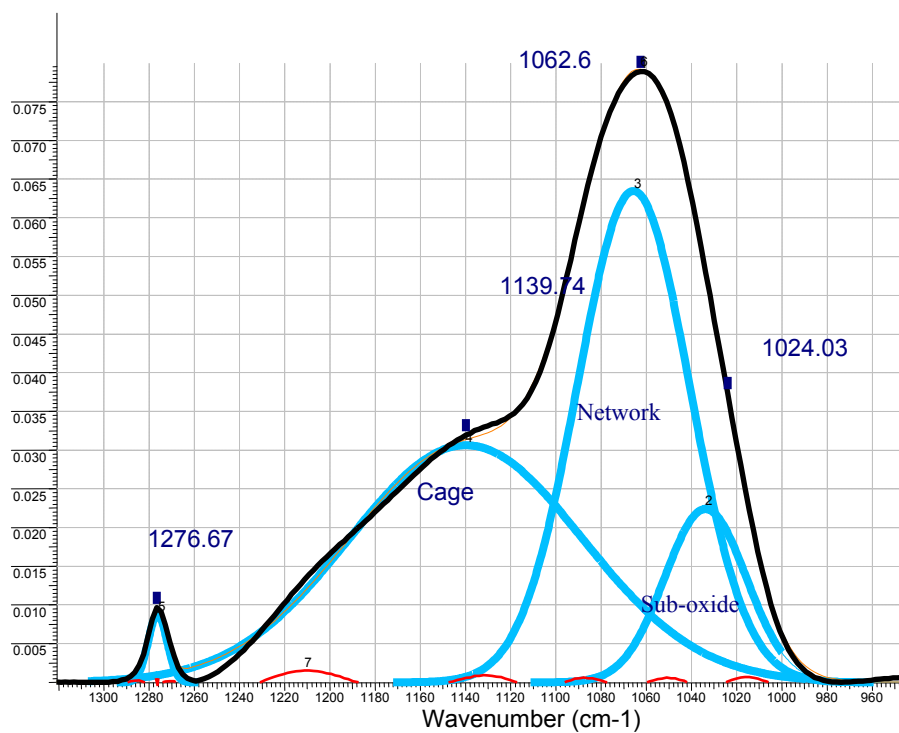


Figure 5.8 Gaussian peak analysis of etched sample shows the cage, network and sub-oxide peak areas. There is a higher percentage of network peaks compared to the unetched samples

The κ values that were determined in the previous section were compared to the cage, sub-oxide and network peak areas.

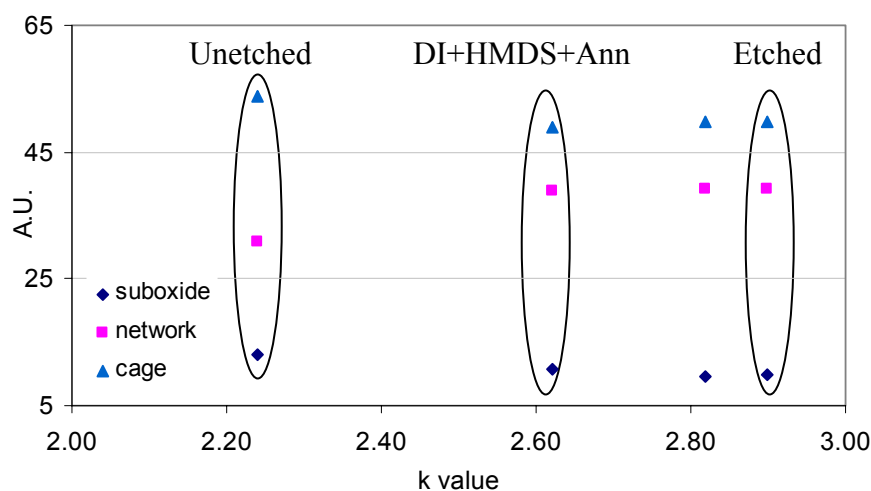


Figure 5.9 Deconvoluted peak areas versus the κ value shows that the cage and sub-oxide decreases and the network increases after the initial etching of the samples. The chemical treatment increases the sub-oxide peak

The κ values increases initially as the cage structure decreases. This is consistent with previously published results [Grill (2003)]. The cage structure is responsible for the porosity of the film. As the cage structure breaks down into a network structure due to etching and ashing, the porosity decreases and as a result the κ value increases.

The HMDS chemical treatment decreases slightly both the cage and network but increases the sub-oxide peak area concentration. The HMDS

treatment also increases the SiCH_3 peak area concentration slightly. The HMDS post ash chemical treatment attaches CH_3 bonds at the sub-oxide sites and as a result recovers the carbon content, to an extent, in the film.

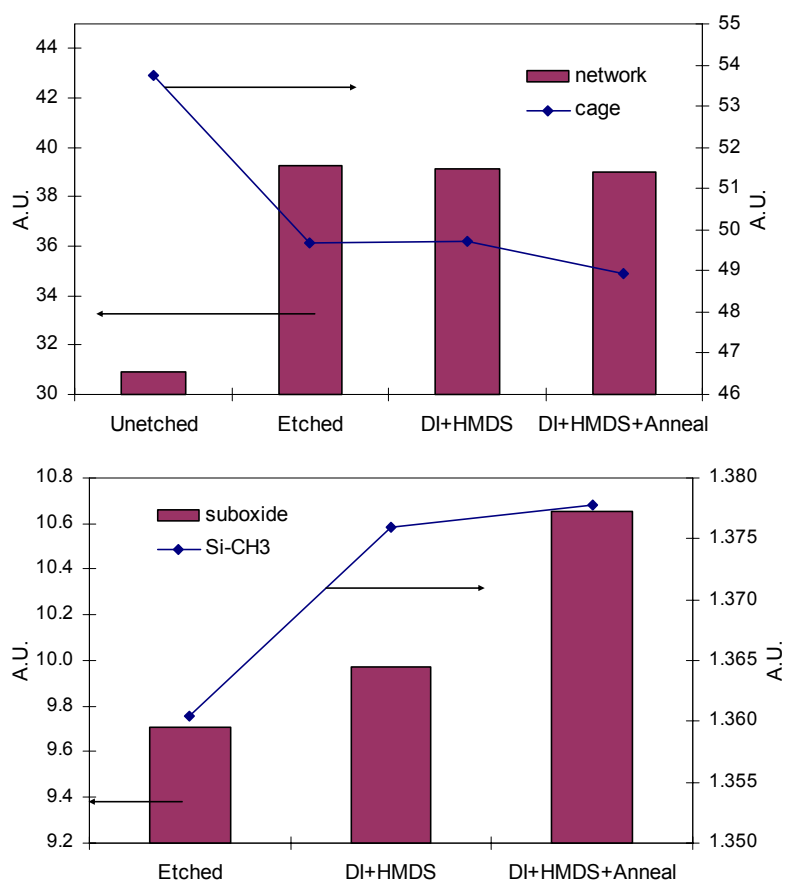


Figure 5.10 Deconvoluted peak areas versus the treatment of the films shows that the etching and ashing decreases the cage and increases the network area. The chemical treatments increases the sub-oxide and Si-CH_3 area to an extent

5.4 EFFECT OF MOISTURE

The κ value was also compared with the hydroxyl peak areas. It was found that the change in κ value could be related to the change in hydroxyl concentration in the films. Hydroxyl groups can be considered to be a type of chemical defect. Chemical defects are atoms or molecules that do not belong in the dielectric lattice. Hydroxyl groups at the interface are an example of chemical impurity which would distort the lattice and create trap states near the interface of the dielectric.

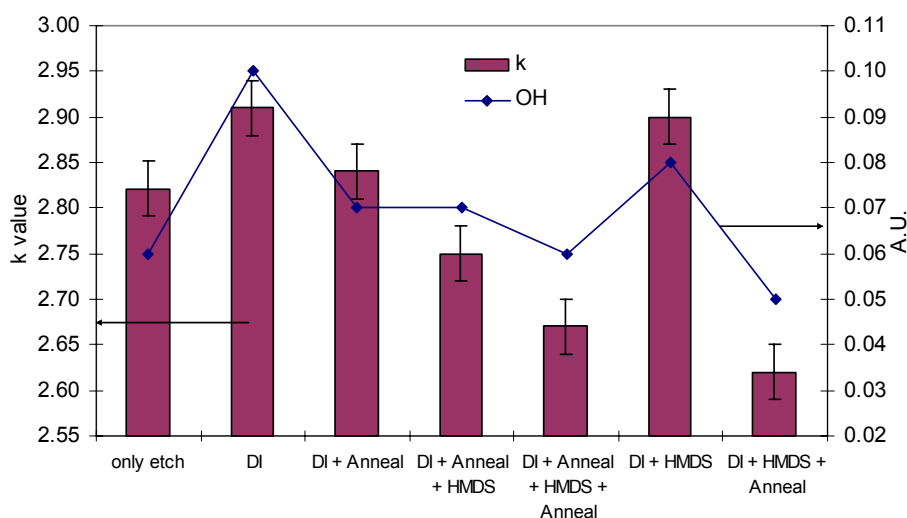


Figure 5.11 Deconvoluted hydroxyl peak areas and κ values versus the treatment of the films shows that the κ value follows the hydroxyl content trend

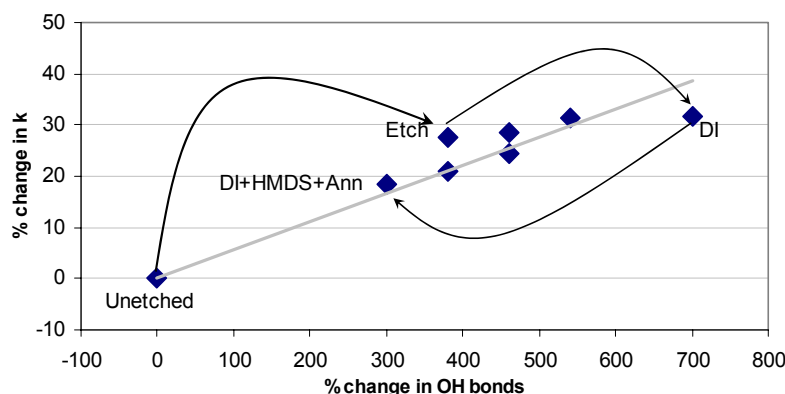


Figure 5.12 Percent change in κ value versus the percent change in hydroxyl bonds shows that the etching and ashing increased the κ value and the hydroxyl content and the chemical treatments reduce the hydroxyl content and recover the κ value to an extent

The change in κ value versus the change in hydroxyl bonds is plotted in Fig 5.12. A chemical treatment with HMDS and an anneal reduces the hydroxyl concentration by about 50% and the κ value decreases by about 10%.

The initial κ value of the unetched film is 2.21 ± 0.03 and the hydroxyl content is negligible. After the film is etched and ashed, the hydroxyl content as well as the κ value increases. The increase in hydroxyl is because of the depletion of carbon and reconfiguration of the Si-O-Si from a cage structure to a network structure. Fig 5.13 shows the postulated hydroxyl bonds at the surface of the low- κ film [Helms (1994), Nguyen (1995)]. The silanol bonds at the surface readily adsorb water. Hence, the κ value as well as hydroxyl content further increases after a DI water cleaning because of the additional water adsorption. This the damaged surface has become hydrophilic. Annealing the films after the DI water clean, removes the adsorbed water and hence reduces the κ value. However, an

anneal by itself does not remove the silanol bonds. A chemical treatment is required to reduce the silanol bond concentration as postulated schematically in Fig 5.13. The HMDS $[(\text{CH}_3)_3\text{Si-NH-Si}(\text{CH}_3)_3]$ treatment not only increases the carbon content in the film but also decreases the silanol content.

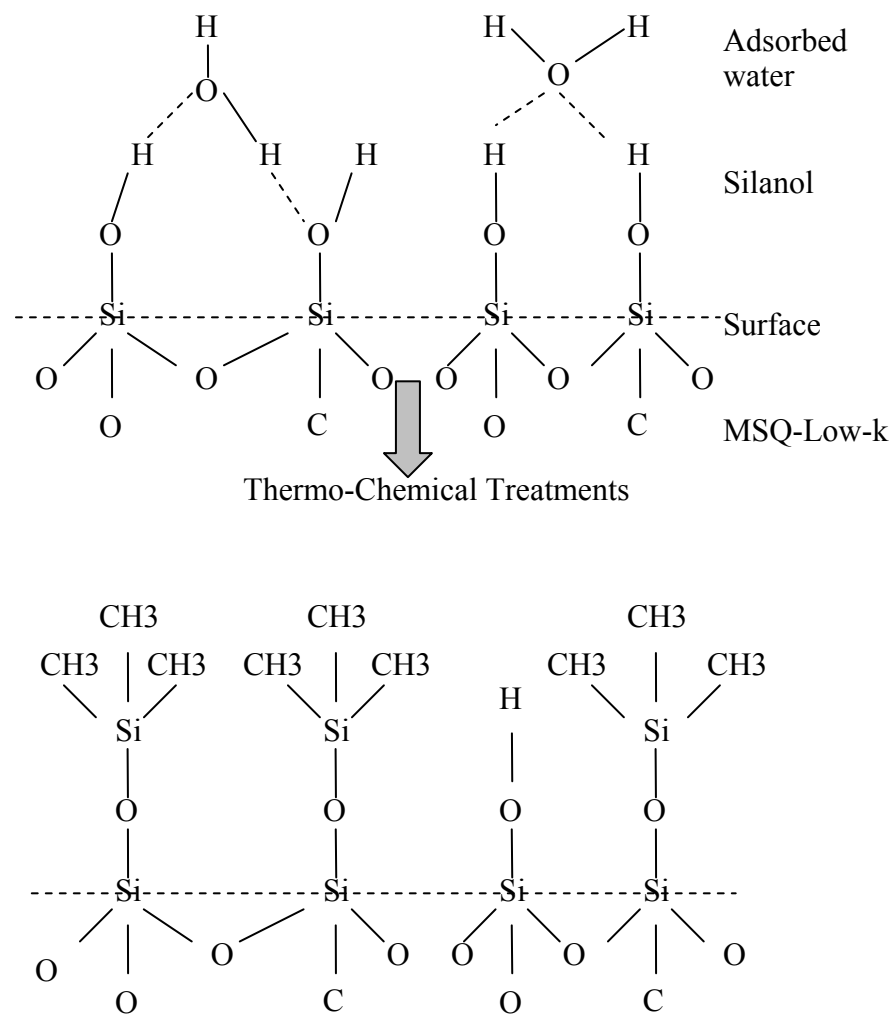


Figure 5.13 Schematic of postulated hydroxyl bonding at the low- κ surface

The concentration of hydroxyl bonds in the dielectric can be estimated from the experimentally determined κ values. We know that the hydroxyl bonds are distributed throughout the dielectric with higher concentration at the surface. The presence of the hydroxyl bonds increases the κ value of the dielectric. However, to simplify the calculation, we make an assumption that the increase in κ value is because of an effective thickness (T_{OH}) of hydroxyl bonds at the top surface of the dielectric. The κ value of this effective thickness is the κ value of water, which is 78.4 at 25°C. The total thickness of the dielectric is T_{total} . The κ value of the dielectric (κ_{LK}) without any hydroxyl bonds is taken to be 2.2 at 25°C. The two thicknesses are assumed to behave like two capacitors in series. Fig 5.14 shows a schematic of the model.

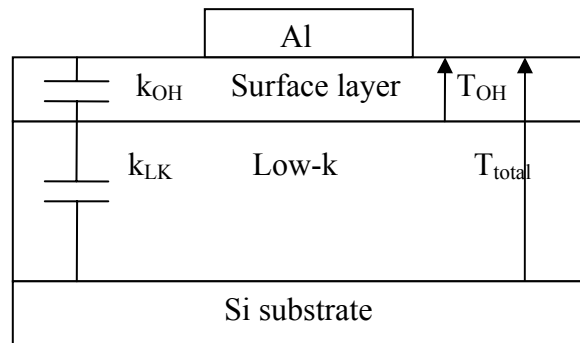


Figure 5.14 Schematic of a capacitance modeling shows the effective hydroxyl thickness at the surface

The effective thickness is calculated from the following formula.

$$T_{OH} = \frac{k_{OH} * [k_{LK} - k_{total}]}{k_{total} * [k_{LK} - k_{OH}]} * T_{total}$$

Where, $T_{total} = 2000 \text{ \AA}$, $k_{OH} = 78.4$, $k_{LK} = 2.2$ and k_{total} is the experimentally determined κ value.

The effective hydroxyl thickness (T_{OH}) is calculated for the κ values (Fig 5.9) obtained from all the different treatments. Fig 5.15 shows the results. A chemical treatment with HMDS and an anneal reduces the hydroxyl concentration by about 34% and the κ value decreases by about 10%.

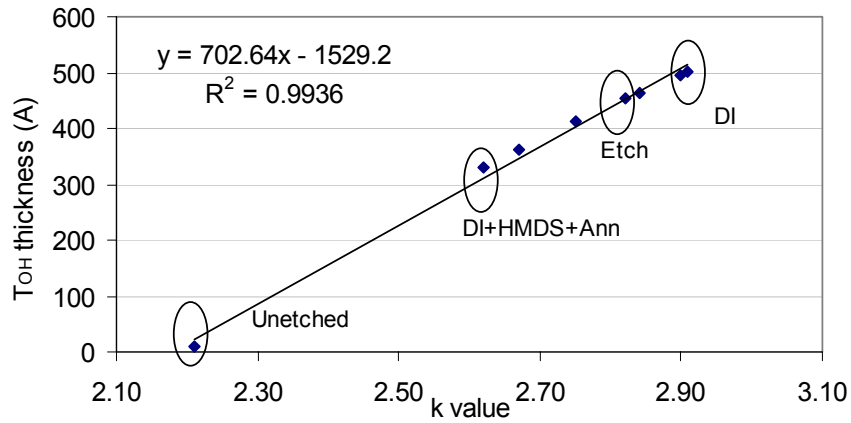


Figure 5.15 Effective OH thickness versus the κ value shows that a chemical treatment reduces the amount of hydroxyl bonds

The effective volume is then calculated by assuming a surface area of 0.007 cm^2 . The density of water is taken as 1.0 g/cc and the concentration of hydroxyl groups is determined from Avogadro's number ($N_A = 6.023 \times 10^{23}$) and atomic mass of water molecules (18g). The result is shown in Fig 5.16.

The concentration of hydroxyl bonds in the dielectric can also be estimated from the FTIR concentration. The hydroxyl peak area concentration is determined from a Gaussian analysis of the FTIR spectra. The concentration of the hydroxyl peak area concentration per unit volume is then calculated from Beer-Lambert law.

$$\ln(I_0/I) = c * \epsilon * t$$

Where I_0 and I are the initial and transmitted IR intensities respectively, c is the concentration of the absorbing constituent in moles cm^{-3} , t is the optical path or the thickness of the sample in cm and ϵ is the extinction coefficient in $\text{cm}^2 \text{ mole}^{-1}$.

The extinction coefficient for the hydroxyl band at 3750 cm^{-1} is taken as $1.79 \times 10^5 \text{ cm}^2 \text{ mole}^{-1}$ from the literature [Korn (1980)].

Fig 5.16 shows the calculated concentration of hydroxyl groups by the effective thickness model as well as the FTIR analysis versus the κ value.

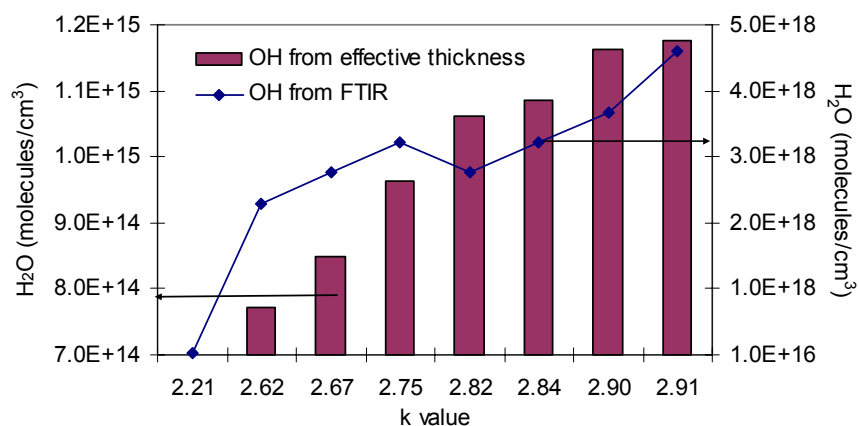


Figure 5.16 Concentration of hydroxyl bonds versus κ value shows that the κ value can be co-related to the concentration of hydroxyl bonds in the dielectric

The plot shows that the κ value increases with increasing concentration of the hydroxyl groups. In Fig 5.17 the fractional change in hydroxyl bonds is plotted versus the fractional change in κ value with respect to the etched sample ($\kappa = 2.82$).

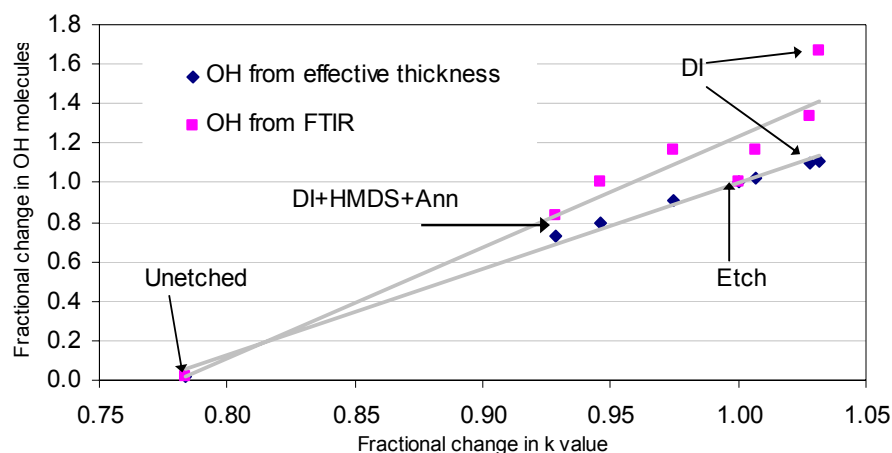


Figure 5.17 Fractional change in κ and hydroxyl bonds with respect to the etched sample shows that a chemical treatment recovers the κ value to an extent

A chemical treatment with HMDS and an anneal reduces the hydroxyl concentration by about 50% and the κ value decreases by about 10%. The effective thickness model is over simplified in its assumption of the effect of hydroxyl bonds on the κ value. Nevertheless, the model justifies the observed κ value dependence on the hydroxyl peak area concentration from FTIR analysis.

5.5 DISCUSSION

Processing effects on the electrical characteristics and the molecular structure of a low- κ material were analyzed. Etching and ashing of an MSQ type of low- κ material alters the silicon dioxide structure in the film. The SiO_2 cage structure is broken down to form a SiO_2 network type of structure.

The κ value of the film should depend on the ratio of cage to network Si-O bonds [Grill (2003)]. A higher percentage of cage structure should give a lower κ

value because of the increase in the porosity. Etching and ashing processes increase the κ value by two ways, first they break the cage structure and as a result decrease the porosity, which increases the κ value, and second they deplete the carbon and increase the hydroxyl concentration, which increases the κ value also.

Thermal and chemical processes were analyzed in terms of their effect on the molecular structure of the damaged dielectric film as well as their effectiveness in recovering the κ value and lowering the leakage. Annealing was useful in reducing the κ value and the leakage to an extent. But annealing by itself, cannot remove all the hydroxyl bonds. The analysis shows that the chemical treatment increases the silicon dioxide sub-oxide type of molecular bonds. Although the treatment does not recover the cage structure of the original low- κ film, it does recover the κ value by reducing the hydroxyl concentration of the film. The analysis showed that a chemical treatment like HMDS vapor restores the carbon content of the film to an extent. This repair of the damage and partial restoration of the κ value leads to better reliability characteristics.

The increase in κ value due to processing will lead to increased effective κ of the Cu/low- κ structure and nullify any advantageous effects of using a low- κ material. The increase in leakage current is also not desirable because of its deleterious effects on the reliability. Further analysis of the effect of processing on reliability will be done in Chapter 6.

Chapter 6: Processing Effects on Damascene Cu/low- κ Structure

In this chapter the effects of surface processing on a single damascene Cu/low- κ structure will be discussed. Firstly the single damascene build will be described. Secondly, two different cleaning technologies will be analyzed. Finally the effects of post ash chemical treatments on electrical characteristics and reliability will be investigated in detail. TEM/EELS and failure analysis will also be presented and discussed.

6.1 SINGLE AND DUAL DAMASCENE TEST STRUCTURES

The dual damascene process has been discussed in detail in chapter 2. The test structure is built in a similar process. The single damascene test structure builds one metal level only. In the first step, a thin thermal oxide (SiO_2) is deposited on the silicon substrate. Then an etch-stop layer is deposited on top of the oxide layer. The etch-stop layer can be silicon nitride (SiN). The purpose of the etch-stop layer is to provide an indication of the completion of the etching of the low- κ material. After the etch-stop layer has been deposited, the low- κ material is deposited. Depending on the type of low- κ , this can either be spin-on process or a chemical vapor deposition process. If it is a spin-on process the wafer will then be cured. The next step is the deposition of the hard mask. The hard mask can be oxide, silicon nitride or silicon carbo-nitride (SiCN). The purpose of the hard mask is to provide an indication of the completion of the chemical mechanical polishing process (CMP). The next step is the deposition of the backside antireflective coating (BARC) and the resist. The BARC is used to prevent the reflection of light, which may cause interference. The wafer is then

exposed to UV light through a mask. After the exposure, the wafer is etched in plasma. Plasma etching is directional. The etching agents are a combination of fluorocarbons, hydrogen, oxygen and nitrogen. The etch products are volatile products of carbon and silicon. After the etching the BARC and the resist has to be removed by a process step known as ashing. The ashing gases are a combination of nitrogen, hydrogen and oxygen. After the etching and ashing of the low-k, a clean is done to further remove the resist and any leftover particulate matter. This step is important in dual damascene because it can also remove the oxides of copper and tungsten. The cleaning is done by de-ionized (DI) water or some combination of chemicals. The next step is the deposition of the thin copper barrier. This is generally tantalum (Ta). Copper seed is then deposited. The trenches are then filled by copper, which is deposited by electroplating. The copper is then annealed to promote grain growth and in order to stabilize the grain structure. CMP is done to remove the excess copper from the surface. The CMP is stopped at the hard mask or it can remove the hard mask partly or completely. It is desirable to remove the hard mask because it increases the effective κ of the structure. However, removing it completely may damage the surface of the low-k. The next step is the deposition of the capping layer, which can be silicon nitride or silicon carbo-nitride. The wafer then goes through another set of patterning to open the contact pads and also to passivate the surface after the pads are opened. The passivation layers are generally silicon dioxides. Fig 6.1 describes in detail the various steps in this process.

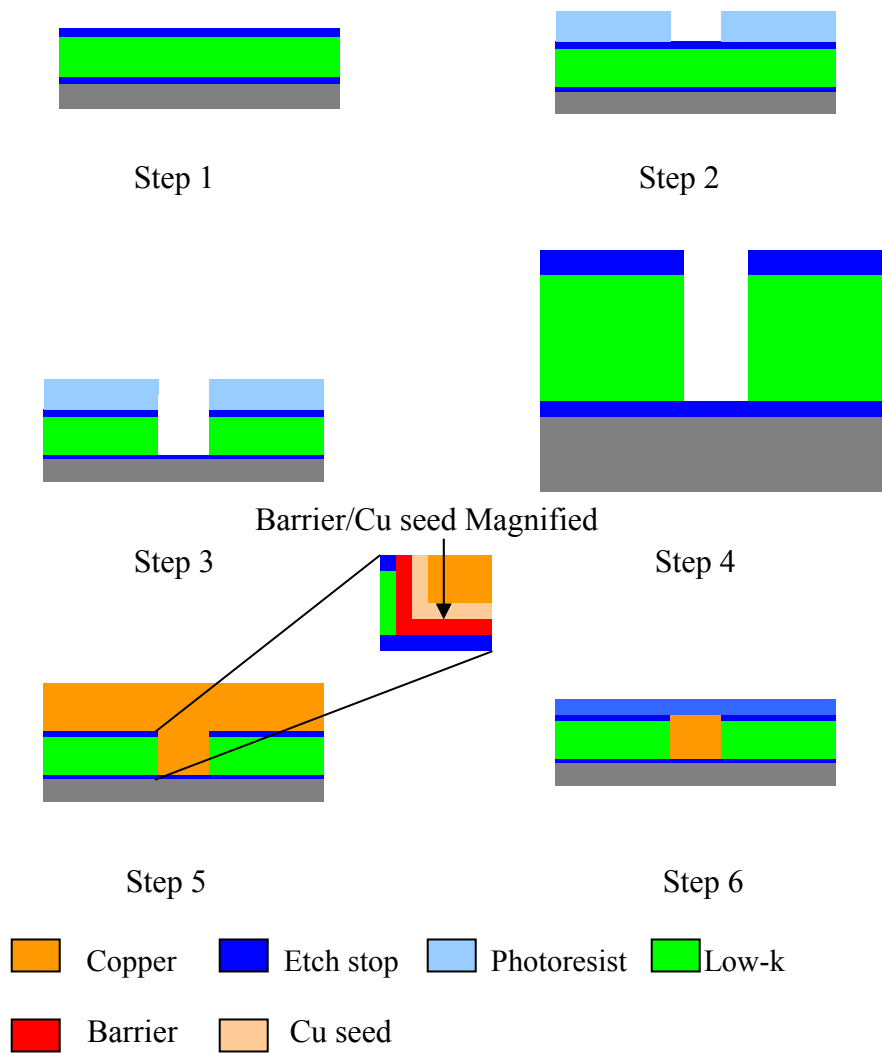


Figure 6.1 Schematic of a single Damascene test structure process

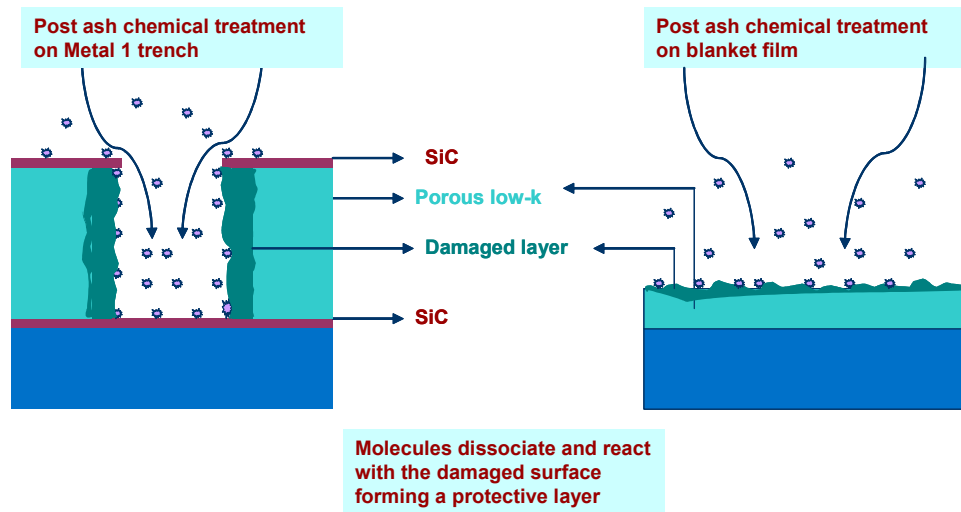


Figure 6.2 Schematic diagram of post-ash chemical treatment on a metal 1 trench and blanket low- κ dielectric film shows the sidewall damage layer

The etching and ashing in step 4 creates damage at the trench side-wall of the low- κ dielectric. Post-ash cleaning and chemical treatments will be investigated in this chapter.

6.2 CLEANING PROCESSES

Trench cleaning after etching and ashing removes particulate matter and also removes metallic oxides and other impurities. There are various cleaning compounds that are used to clean trenches. These compounds contain different chemicals, which are generally proprietary information. In this section cleaning chemistries will be analyzed with de-ionized (DI) water as a baseline. The cleaning chemistries include methanol (MeOH), ethanol (EtOH), iso-propanol (IPA), proprietary treatments (PT1 and PT2) and super-critical carbon dioxide (SCCO₂).

6.2.1 Liquid Cleaning

A dual damascene process was used to build copper/low- κ structures with comb-comb capacitors. The dual damascene scheme is described in detail in Chapter 2. Various combinations of liquid chemicals were used for cleaning purposes after the trench was etched and ashed. The cleaning was performed in the metal 2 level only. Table 6.1 lists the various chemical combinations that were used. The purpose of this study is to determine the effect of cleans on the capacitance and the leakage of the Cu/low- κ structures.

The comb-comb capacitors with line widths of 0.25 μm and line space of 0.30 μm were used for electrical tests. Capacitance and leakage current were measured for all the splits. Measurements were made all across the wafers.

Figure 6.3 shows the RVB and κ value for all the splits.

Wafer#	DIW	PT1	PT2	IPA	MeOH	HMDS
W01				X		X
W03	X			X		X
W06			X		X	
W07		X			X	
W09		X			X	X
W12	X				X	X
W15					X	
W16					X	X
W24	X					

Table 6.1 Split information of different liquid cleans

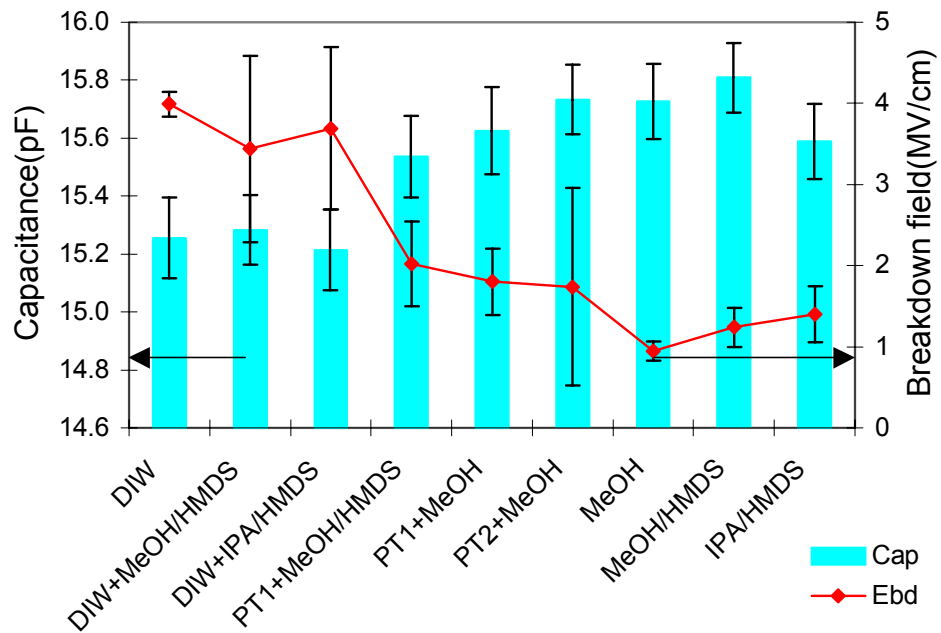


Figure 6.3 Breakdown and capacitance values for different cleans shows that the various cleans increase the capacitance slightly and decreases the breakdown field

The experimental data showed that all the liquid cleans increased the capacitance compared to only DI water. Also the leakage current increased and breakdown field dropped.

DI water is the most gentle of all the liquid cleans. Except for water absorption by the trench low- κ material, there is no other chemical change due to DI water clean. Alcohols can remove silanol bonds from the MSQ material and help in reducing the k -value. However, for the splits we looked at, alcohol additives did not show any improvement in the k -value or the breakdown. The purity of the additives could be an issue. However, it is more probable that the liquid chemistries are adding instead of removing hydroxyl bonds. This could increase the defect density at the interface and result in higher leakage and higher capacitances.

6.2.2 Super Critical CO₂ Cleaning

In recent years super critical CO₂ (SCCO₂) has been investigated as a cleaning fluid. Its attractiveness lies in the fact that it has minimal surface tension, which allows it to penetrate into small geometries [Hsiao-Shou (1994), Purtell (1993) and Biberger (2000)]. Supercritical fluids have solvating properties of a liquid and the mass transfer characteristics of a gas. These characteristics make it a promising candidate for wafer cleaning processes. The condensation of silanol in alcoholic solvents is well known [Grubb (1954), Sprung (1960), Lu (2001), Silvestrelli (2004) Carbone (2005)]. Xie (2004) showed that SCCO₂, when used with alcoholic co-solvents removed the silanol bonds in a porous MSQ film and restored the hydrophobicity of the film. The depletion of carbon and increase in

hydroxyl bonds due to etching and ashing is one of the primary reasons for the increase in effective κ of the whole structure. Recovery of κ is essential, especially for smaller geometries where the effect of carbon-depletion and hydroxyl increase is magnified. In this section, the effect of SCCO₂ and additives will be analyzed by measuring capacitance and leakage of Cu/low- κ structures.

The test structure is comb-comb capacitors, which were processed by the dual damascene scheme. The SCCO₂ clean is used for the metal 2 level only. Table 6.2 shows the different splits, which were processed to analyze the effect of SCCO₂. DI water was used as the baseline.

Wafer#	DI water	CO ₂ only	MetOH	EtOH	HMDS
W18	X				
W21		X			
W22		X		X	
W23		X	X		
W24		X	X		X

Table 6.2 Split information for the SCCO₂ experiment

Three types of additives were used along with the SCCO₂. The additives are 99% pure methanol (MetOH), 95% pure ethanol (EtOH) and 99% pure hexamethyldisilazane (HMDS). Previous studies have shown that these additives reduce the silanol bonds in the MSQ materials and as a result lower the κ value. They also change the surface from hydrophilic to hydrophobic.

Figure 6.4 shows the capacitance and breakdown fields for the different splits. The SCCO₂ process by itself or with MetOH showed an improvement in

both κ value and breakdown. The SCCO₂ process with EtOH did not show an improvement.

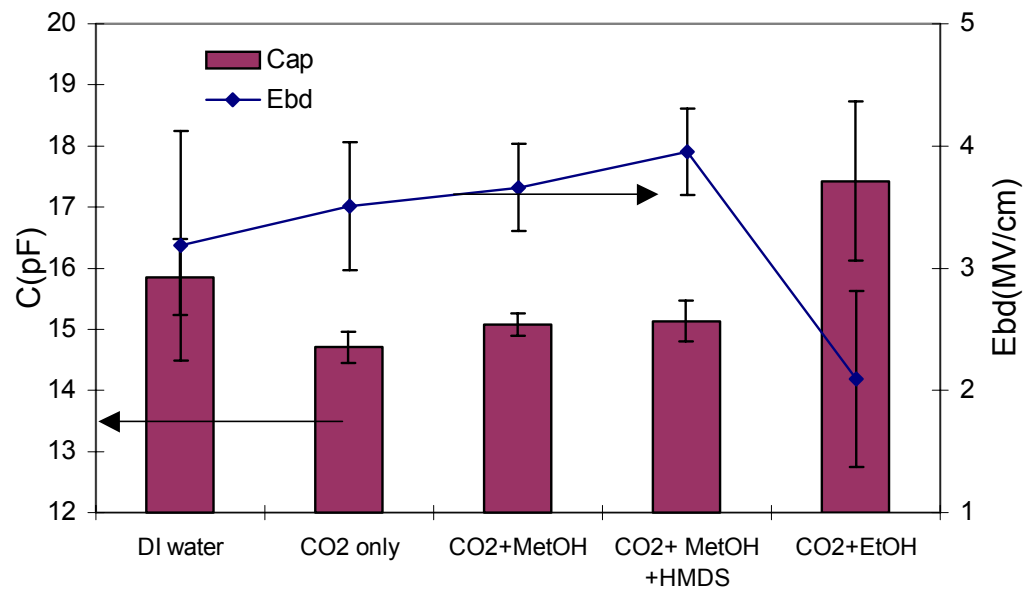


Figure 6.4 Capacitance and breakdown field versus the cleaning treatments shows the improvement due to SCCO₂ cleaning

The effect of SCCO₂ on the dielectric reliability was also investigated. TDDB measurements were made on comb-comb structures with line width 0.25 μm and line space of 0.30 μm . Time-to-fail (TTF) were obtained at three different electric fields and all the measurements were made at 105°C.

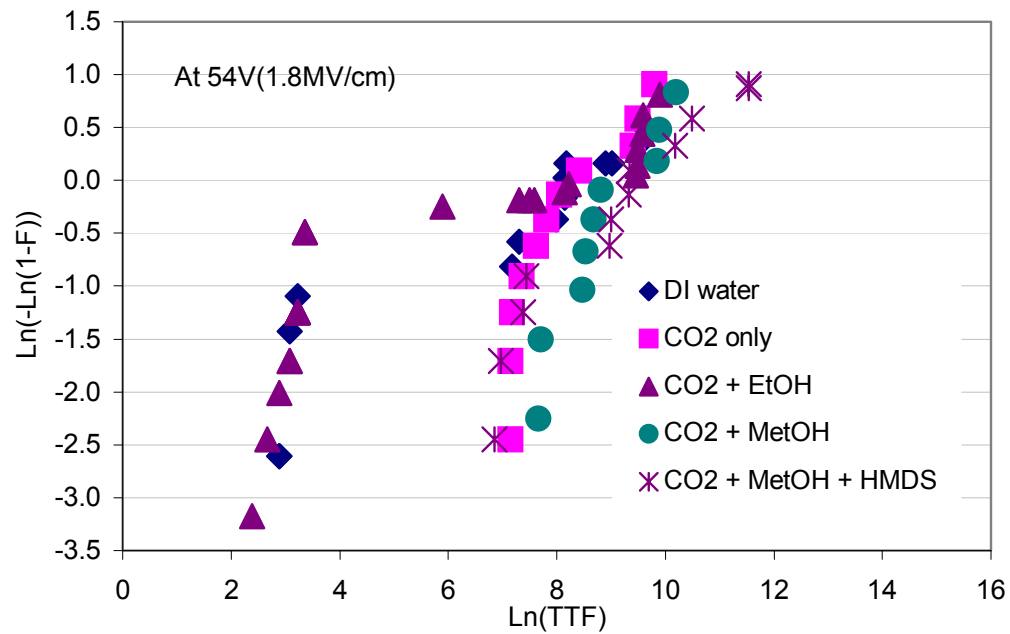


Figure 6.5 Weibull distribution of the TTF at 1.8MV/cm shows that the SCCO₂ processes, with the exception of EtOH, improve the lifetime slightly

The Weibull distribution of the TTF shows that there are a large percentage of early failures for the split SCCO₂ with EtOH. The DI water split has a higher early failure percentage than the other SCCO₂ splits. The measurements were made across the wafer. The die yield, which is defined as the percentage of good dies, is 90-92% for the splits with SCCO₂, SCCO₂ with MetOH and SCCO₂ with MetOH and HMDS. The DI only split has a die yield of 65% whereas the split with SCCO₂ with EtOH has a die yield of 33%. The yield percentages were also determined for the metal 1 level comb-comb structures. The metal 1 level for all the wafers did not undergo any separate processing and hence they should give the same yield. This was found to be the case with ~70% yield percentages for all the wafers. Also, the early failure dies are all across the wafer. Therefore, the low die yield of SCCO₂ with EtOH is not due to non-uniform distribution of ethanol. The low yield is an effect of the ethanol additive, which is not pure enough. The lower yield of DI water compared to the SCCO₂ splits could be an effect of moisture. There is the possibility that water penetrates into the interface between the low- κ and the hard mask. This would result in early failures.

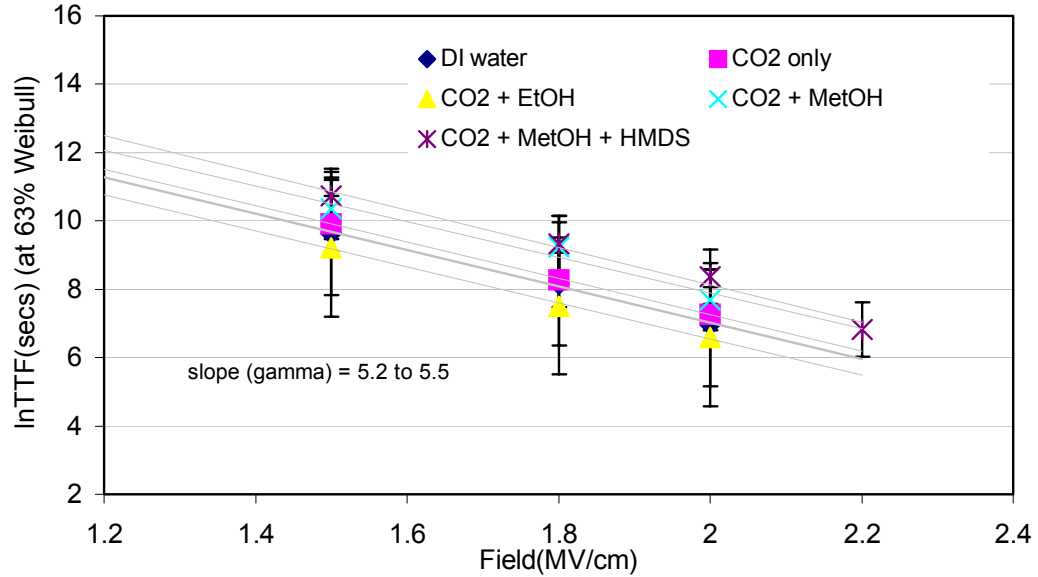


Figure 6.6 Lifetime versus the electric field for the various splits shows that the SCCO2 processes improve the lifetime slightly

Figure 6.6 shows the lifetime for the different SCCO2 splits. The lifetime is taken at 63% of the Weibull distribution. Even though the standard deviation is high (0.7 to 0.9) it can be seen that the SCCO2 cleaning processes showed an improvement in the lifetimes by a factor of 2 to 3 compared to only DI clean. Even if the early failures are removed the improvement is still the same. The effect of the additives cannot be separated due to the high standard deviations. However, ethanol as an additive gave low die-yields and a high percentage of early failures.

SCCO2 process reduced the capacitance by 5-7% and improved the breakdown field of the Cu/low- κ structures. It also improved the lifetime slightly.

SCCO₂ process is a promising technology, which can be used as a carrier of other chemical compounds for repairing the damage and restoring the effective κ of the Cu/low- κ structure.

6.3 POST ASH PROCESSES

The previous section showed how cleaning processes can affect the electrical characteristics of Cu/low- κ structures. In this section the effect of post-ash treatments will be discussed. In the first part, the purpose of post ash treatments will be discussed. Different chemical treatments will then be investigated. The pitch dependence of capacitance will be discussed and one treatment will be chosen to perform further analysis. In the second part reliability tests will be performed at room temperature and the results will be discussed in detail. In the third and final part, the reliability of these structures at high temperatures will be analyzed and the results will be discussed.

6.3.1 Chemical Treatments

Low- κ materials are susceptible to etching and ashing damage. Unoptimized etching, ashing and cleaning processes could potentially damage the dielectric. This damage may be carried forward into subsequent processing steps and ultimately leads to higher effective dielectric constant. The damage also increases the leakage current through the intra-level dielectric (ILD) and compromises the reliability of the interconnect structures.

The purpose of post ash treatments is to recover the κ value of the trench dielectric and improve the leakage and reliability characteristics. TEM/EELS analysis was done to determine the extent of the damage caused by etching and ashing. Electron energy-loss spectroscopy (EELS) is performed in a transmission electron microscope (TEM). The incident electrons in a TEM lose energy due to inelastic collisions. The transmitted electrons can be analyzed in terms of their energy losses. Information about the elemental composition, chemical bonding and electronic structure can be obtained from EELS analysis.

Figures 6.7 and 6.8 shows the TEM/EELS analysis. The analysis was done on a 0.125 μm line width and 0.175 μm line space comb-comb structure. The scan shown in the figure is from the center of the trench. If we consider the ratio of oxygen to carbon content, the analysis shows that there is carbon depletion at the interface for the untreated sample. After the post ash treatment the carbon is recovered significantly. The O to C ratio decreases from about 3 to about 1. The carbon depletion is accompanied by the creation of silanol (Si-OH) bonds, which increases the κ value of the structure. The post-ash chemical treatment recovers the carbon to an extent and reduces the hydroxyl bonds, which leads to lower κ values. FTIR analysis of blanket films in Chapter 5 explains in detail the changes in chemical structures due to the etching and ashing.

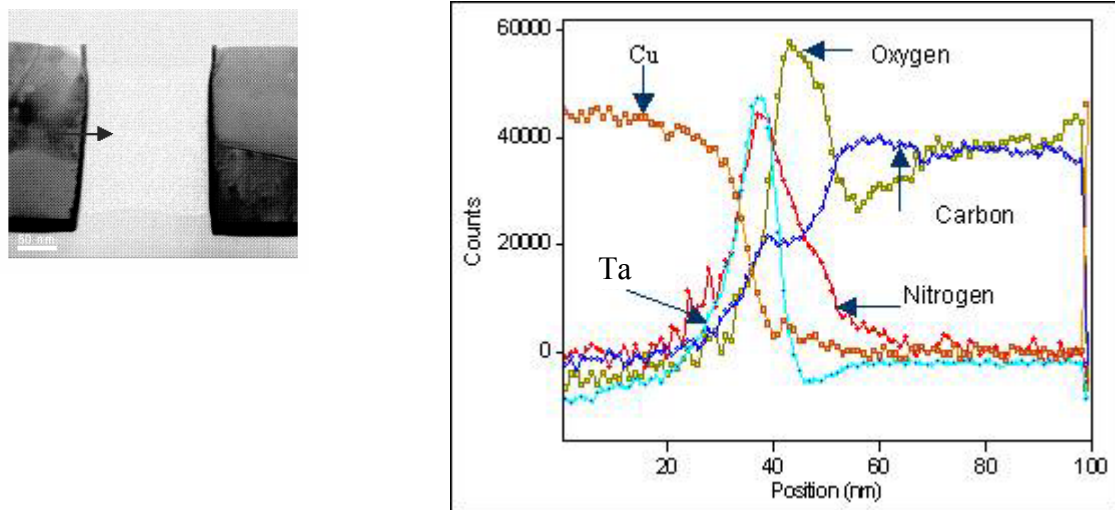


Figure 6.7 TEM/EELS without post-ash treatment shows the carbon depletion

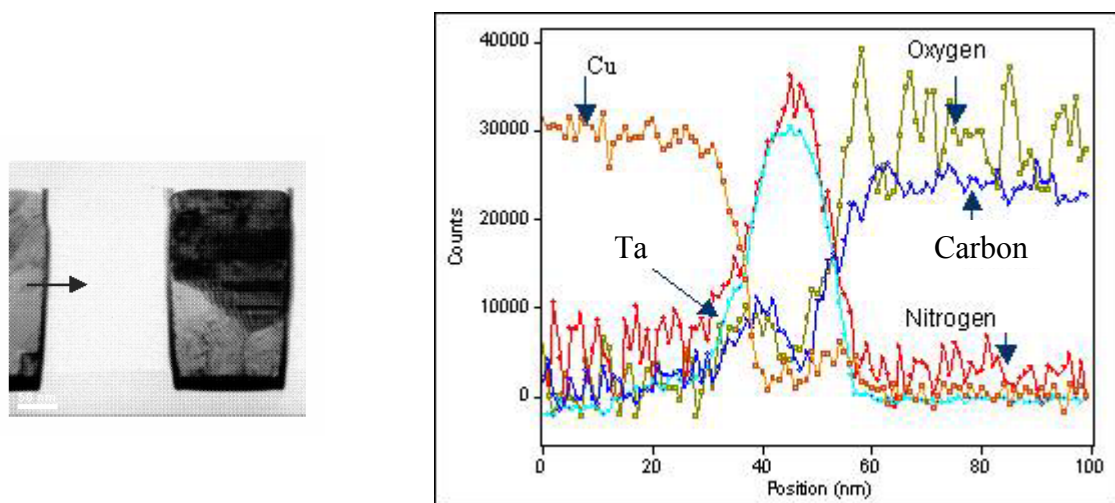


Figure 6.8 TEM/EELS after post-ash treatment shows the carbon recovery

The TEM/EELS analysis shows that the extent of damage could be as much as 10 nm on each side of the trench. Etching and ashing processes are directional. Hence the extent of damage will be constant irrespective of the width of the trench. As metal lines shrink further, the extent of damage will be far greater for smaller pitches than larger pitches. If we assume a κ value of 2.3 and a damaged layer κ value of 4.0, which is a conservative estimate because the damaged layer will absorb moisture which will greatly increase the κ value, then the increase in κ value at the 45 nm node is as much as 60%. Figure 6.9 illustrates this effect. It is therefore essential to recover the κ value before filling the trench with metal.

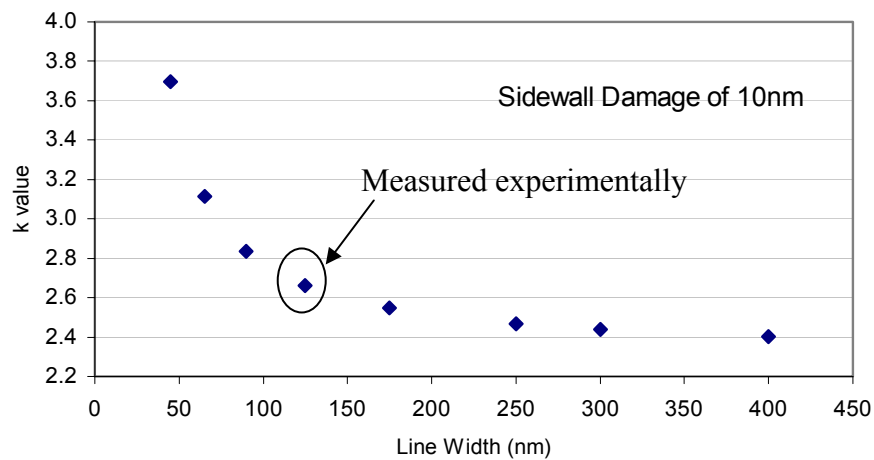


Figure 6.9 Effective κ value rapidly increases with decreasing line-widths assuming a constant side-wall damage of 10nm

A single damascene Cu/low- κ structure was built for analyzing the effects of post ash treatments on the electrical characteristics. The low- κ material is MSQ based with a κ value of 2.3. After etching opened the trench, and ashing removed the resist and BARC, a DI water cleaning was done to remove any particulate matter or other chemical leftovers. After the cleaning three types of post ash chemical treatments were performed. They are hexamethyldisilazane (HMDS), tetramethylcyclotetrasiloxane (TMCTS) and tetramethylsilicon (4MS). They are all vapor treatments. These chemicals were chosen because they can easily disassociate and condense silanol and add methyl groups to the damaged interface. A split was also made where each wafer was also annealed after the treatment. The annealing was done at 400°C for 30 minutes. The data for 4MS without annealing is not available because the wafer was misprocessed.

Figure 6.10 shows the distribution of the capacitance for all the splits. The data is for a line width of 0.125 μm and a line spacing of 0.175 μm . The data shows that the HMDS followed by an anneal reduced the capacitance by about 3%. The split with only annealing also reduced the capacitance, but by only about 0.5%. All other treatments increased the capacitance by 1-8%. Figure 6.11 summarizes the capacitance and breakdown fields for all the treatments. Annealing increased the breakdown field for all the three treatments. Annealing removes the moisture and as a result reduces the leakage current, which results in higher breakdown fields.

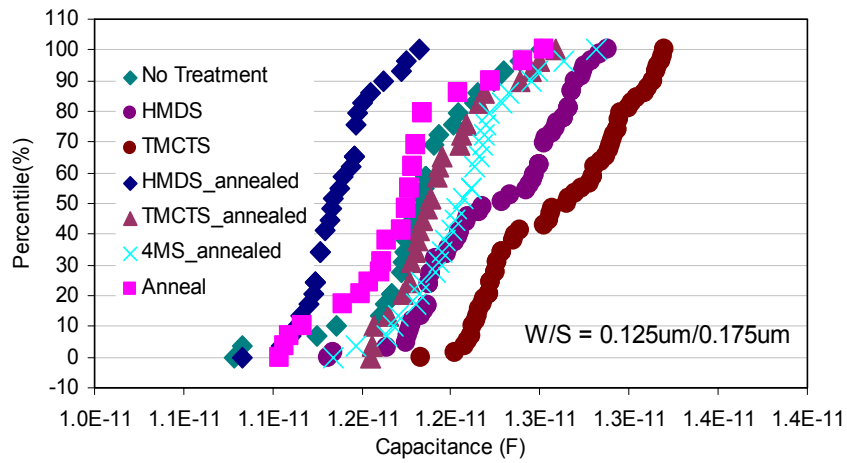


Figure 6.10 Distribution of capacitance for all treatments shows that the HMDS followed by an anneal treatment decreases by capacitance by about 3%

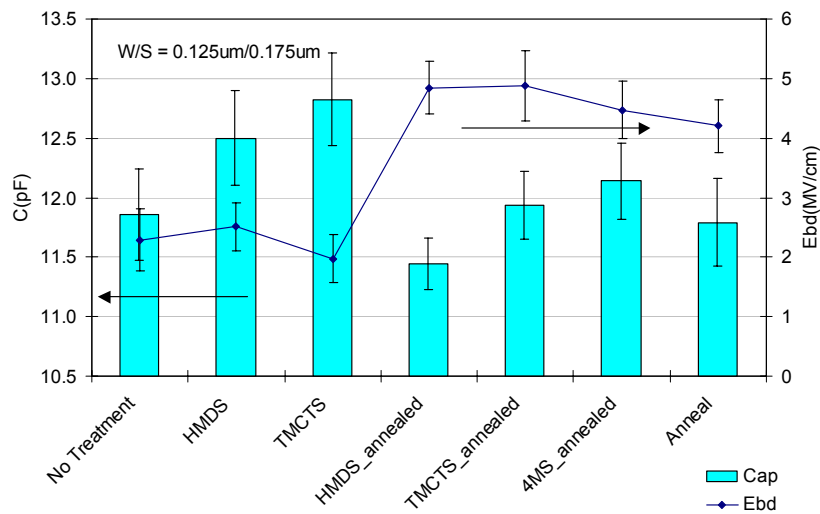


Figure 6.11 Capacitance and breakdown fields for all treatments shows that the thermo-chemical treatments decrease the capacitance and increase the breakdown field

The breakdown field also has a dependence on the pitch. Smaller pitches generally have a lower breakdown field. Figure 6.12 shows the pitch dependence of the breakdown field for all treatments. The effect of the treatments is also more apparent for smaller pitches. This is because of the directional nature of etching and ashing, which produces constant damage layer thickness irrespective of the trench width.

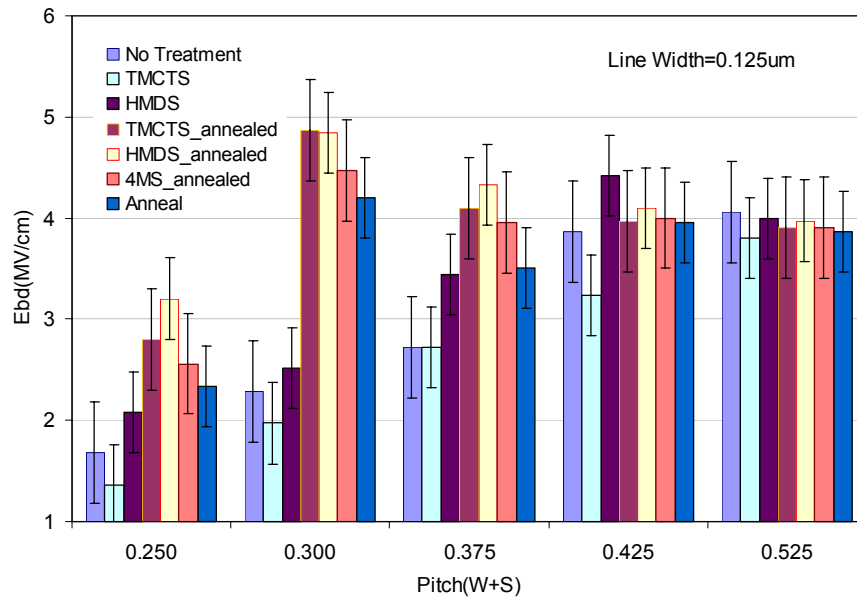


Figure 6.12 Pitch dependence of breakdown fields shows that the breakdown field decreases for smaller pitches

The capacitance also has a pitch dependence similar to the breakdown field. The extent of the κ recovery by the post ash treatment can be estimated by analyzing the pitch dependence of the capacitance. The sidewall damage can be modeled as an addition of a sidewall series capacitance to the bulk undamaged capacitance as shown in Figure 6.13 [Iacopi (2004)].

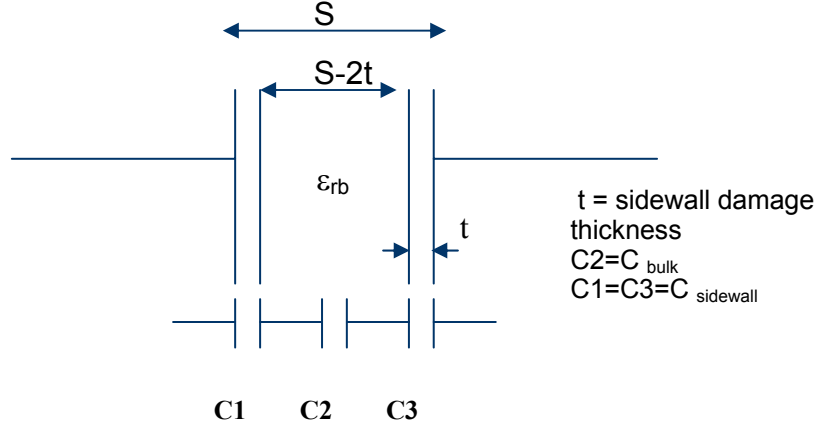


Figure 6.13 Schematic of capacitance modeling shows the effective side-wall damage layers

If we assume that the thickness of the sidewall layer is “t”, then the thickness of the inside bulk undamaged layer is (S-2t) where S is the total line space. The total capacitance is then given by,

$$1/C_{\text{total}} = 2/C_{\text{sidewall}} + 1/C_{\text{bulk}}$$

$$\text{or, } 1/C_{\text{total}} = 2/C_{\text{sidewall}} + (S-2t)/\epsilon_0\epsilon_{rb} A$$

The TEM/EELS analysis shows that the damage thickness layer can be as much as 10 nm. So if we assume a sidewall thickness (t) of 10 nm and plot $1/C_{\text{total}}$ vs. (S-2t) then the intercept should give us the sidewall capacitance. Figures 6.14 and 6.15 shows the $1/C_{\text{total}}$ vs. (S-2t) plots for the control sample and HMDS followed by an anneal sample. The sidewall capacitance for the control is $104 \pm 4 \text{ pF}$ whereas it decreases to $61 \pm 2 \text{ pF}$ for the post ash HMDS treatment. From this we can infer that at the sidewall of the trench the κ value has been recovered by a factor of ~2.

The fit is made with the average value of capacitance as shown in the figure 6.14 and 6.15 by the central line.

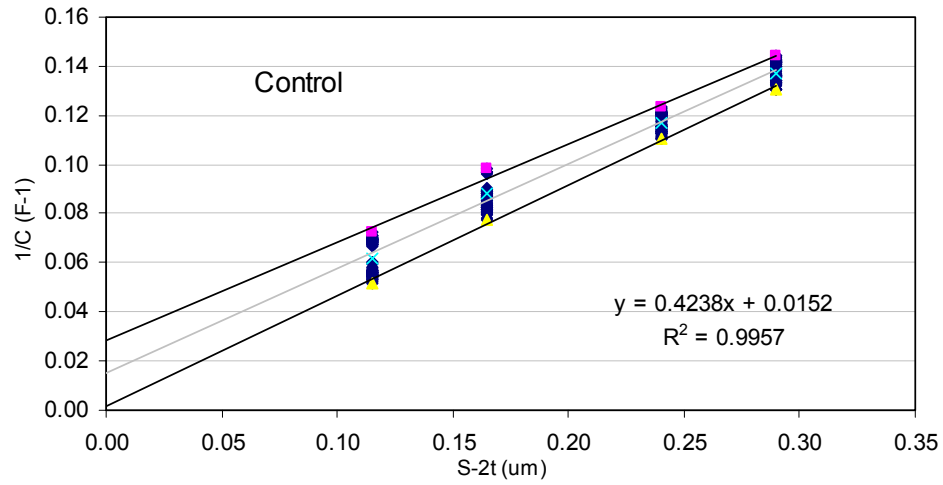


Figure 6.14 Plot of $1/C$ versus $(S-2t)$ for the untreated control sample

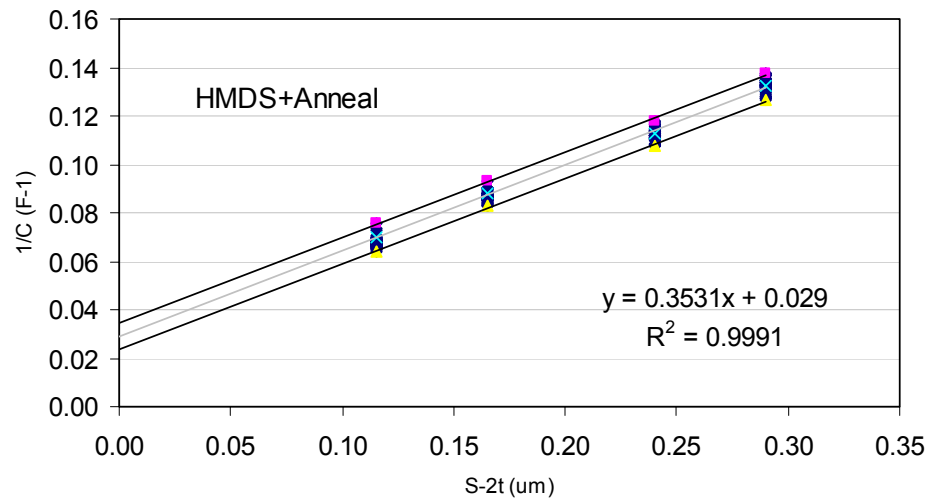


Figure 6.15 Plot of $1/C$ versus $(S-2t)$ for the HMDS followed by an anneal treatment shows that the sidewall capacitance has decreased ($1/C$ increases)

The analysis of the electrical data for all the post ash treatments shows that HMDS followed by an anneal showed the most improvement in the κ value as well as breakdown field and leakage. Further testing of the reliability characteristics is done on this split.

6.3.2 Low Temperature Reliability

Reliability of Cu/low- κ structure is determined by TDDB measurements. The test structure is a comb-comb capacitor with line width of $0.125\mu\text{m}$ and a line spacing of $0.175\mu\text{m}$. Three different splits were tested. The first split is a control split without any post ash treatment. The second split underwent a post ash treatment of HMDS vapor. The third split underwent an annealing after the HMDS vapor treatment.

Three different comb-comb areas were tested. The breakdown fields of the three areas and three splits are shown in Figure 6.16. As can be seen from the figure, the HMDS treatment followed by an anneal gave higher breakdown fields. Also smaller areas had a higher breakdown field. A capacitor with a larger area will have a higher probability of defects than a capacitor with a smaller area. Hence the breakdown field of a small capacitor is higher than a large capacitor.

Low temperature reliability measurements are made at high electric fields. In this case, electric fields from 3.0 to 4.0 MV/cm were applied. All the measurements were made on the medium sized capacitor with an area of 0.001 cm^2 .

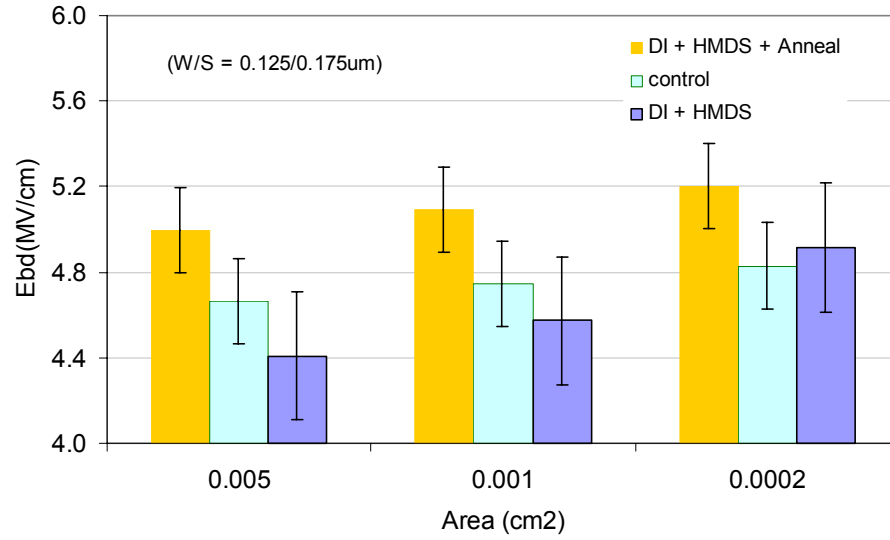


Figure 6.16 Breakdown field for all three treatments versus the capacitor area shows that the breakdown field is smaller for larger areas and it is higher for the HMDS followed by an anneal treatment

The lifetimes obtained from TDDB measurements fit well to a Weibull distribution. The Weibull shape parameters ranged from 1.3 to 2.3, which is similar to values reported in the literature for Cu/low-κ structures [Ogawa (2003)].

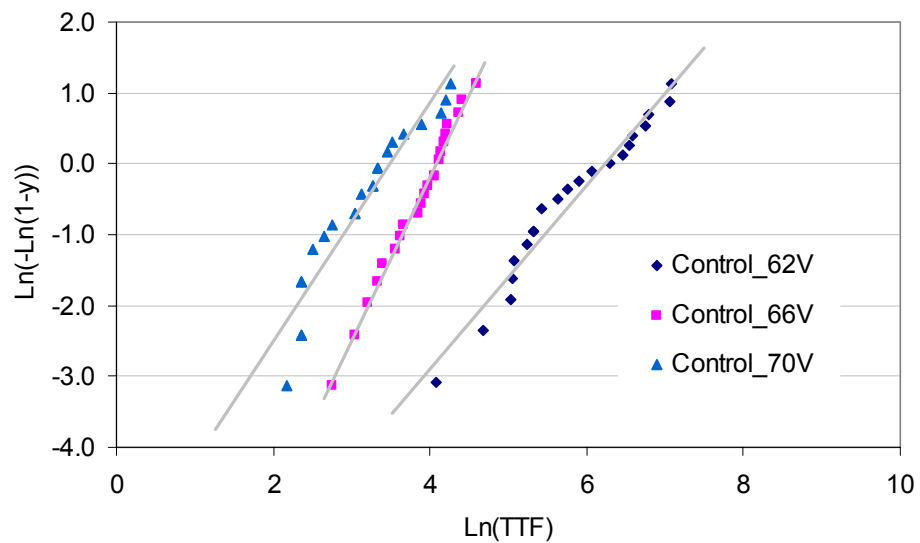


Figure 6.17 Weibull fit for the control sample shows that higher fields gives lower lifetimes

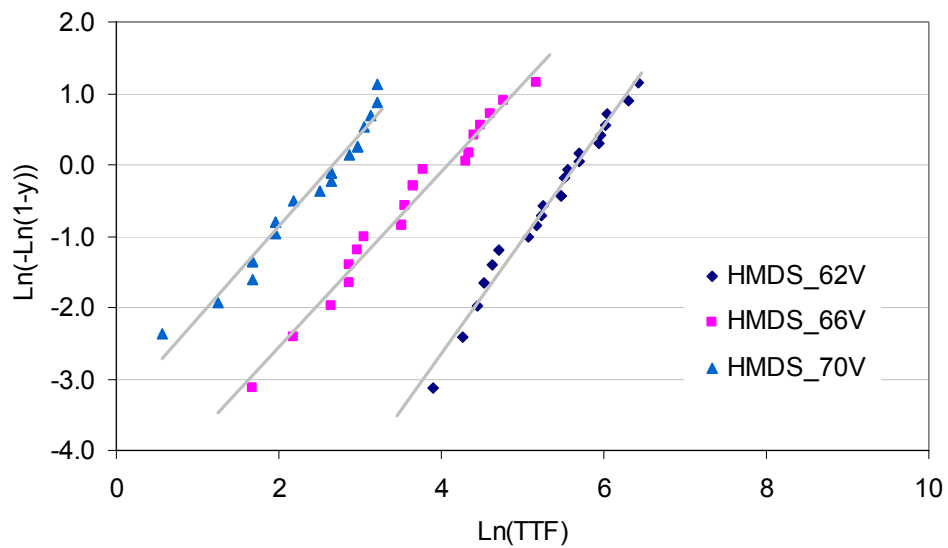


Figure 6.18 Weibull fit for the HMDS post ash treatment shows that higher fields gives lower lifetimes

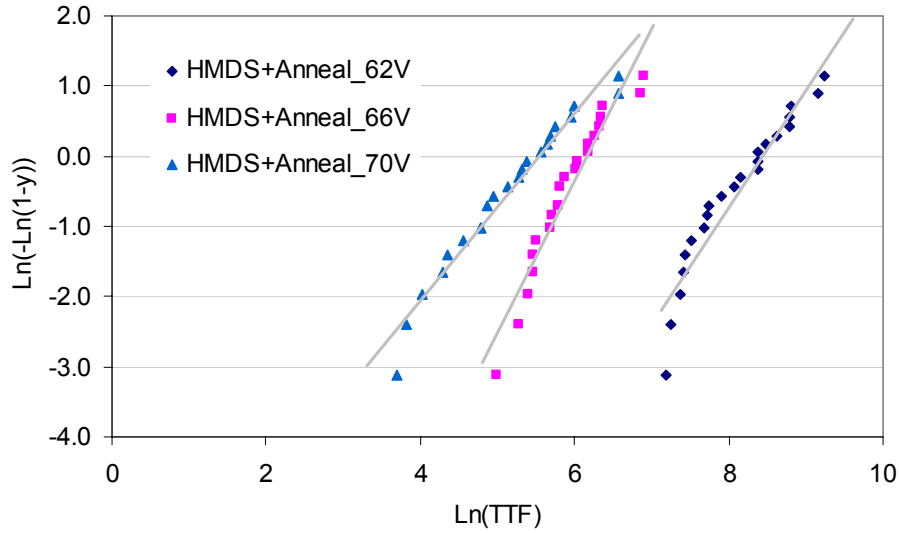


Figure 6.19 Weibull fit for the HMDS followed by an anneal post ash treatment shows that higher fields gives lower lifetimes

The lifetime values at 63% of the Weibull fit are plotted versus the electric field as shown in the Fig 6.20. The field acceleration parameter ranges from 6-7 cm/MV for all three splits. The data shows that the HMDS followed by an anneal improved the reliability by about 8-9 times. The improvement in reliability is believed to be due to the beneficial effect of the post ash clean in reducing the defect density at the interface. An estimation of the defect density will be made after further analysis of the reliability at high temperatures.

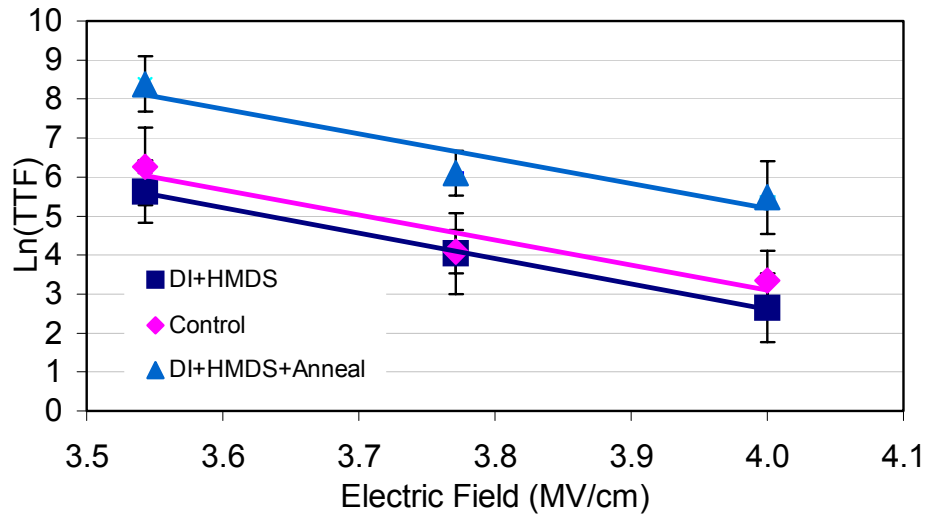


Figure 6.20 Lifetime at 63% Weibull fit versus the electric field shows that the HMDS followed by an anneal treatment gives higher lifetimes

6.3.3 High Temperature Reliability

The high temperature reliability tests were performed on comb-comb capacitor with line width of $0.25\mu\text{m}$ and a line spacing of $0.30\mu\text{m}$. Three different splits were tested. The first split is a control split without any post ash treatment. The second split underwent a post ash treatment of HMDS vapor. The third split underwent an annealing after the HMDS vapor treatment.

Three different comb-comb areas were tested. The breakdown fields of the three areas and three splits are shown in Fig 6.21. As can be seen from the figure, the HMDS treatment followed by an anneal gave higher breakdown fields. Also smaller areas had a higher breakdown field. A capacitor with a larger area will

have a higher probability of defects than a capacitor with a smaller area. Hence the breakdown field of a small capacitor is higher than a large capacitor.

High temperature reliability measurements were made at electric fields ranging from 2.5 to 3.3 MV/cm was applied. All the measurements were made on the medium sized capacitor with an area of 0.001 cm^2 .

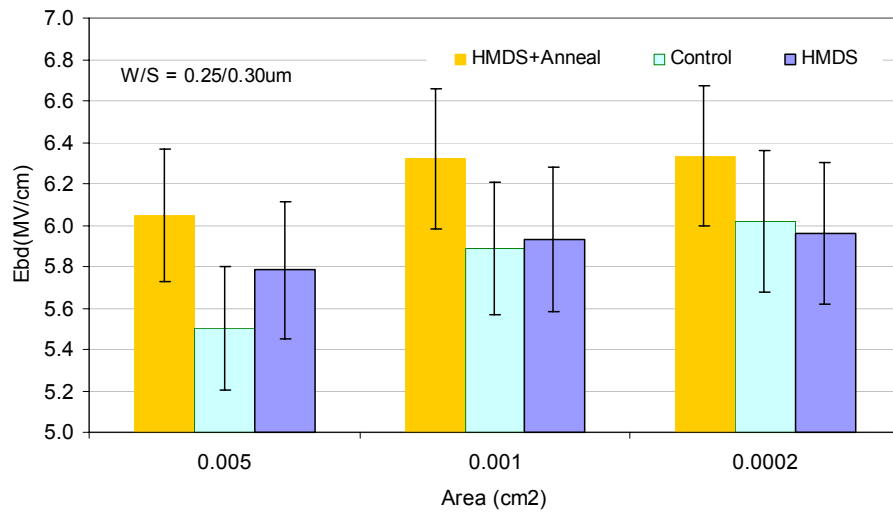


Figure 6.21 Breakdown field for all three splits shows that the breakdown field is smaller for larger areas and it is higher for the HMDS followed by an anneal treatment

TDDDB measurements were made at temperatures of 200°C, 250°C and 300°C. The lifetimes obtained from TDDDB measurements fit well to a Weibull distribution. The Weibull shape parameters range from 1.2 to 2.0, which is similar to values reported in the literature for Cu/low-κ structures [Ogawa (2003)]. Fig 6.22, 6.23 and 6.24 shows the Weibull distributions of all three splits at all three temperatures.

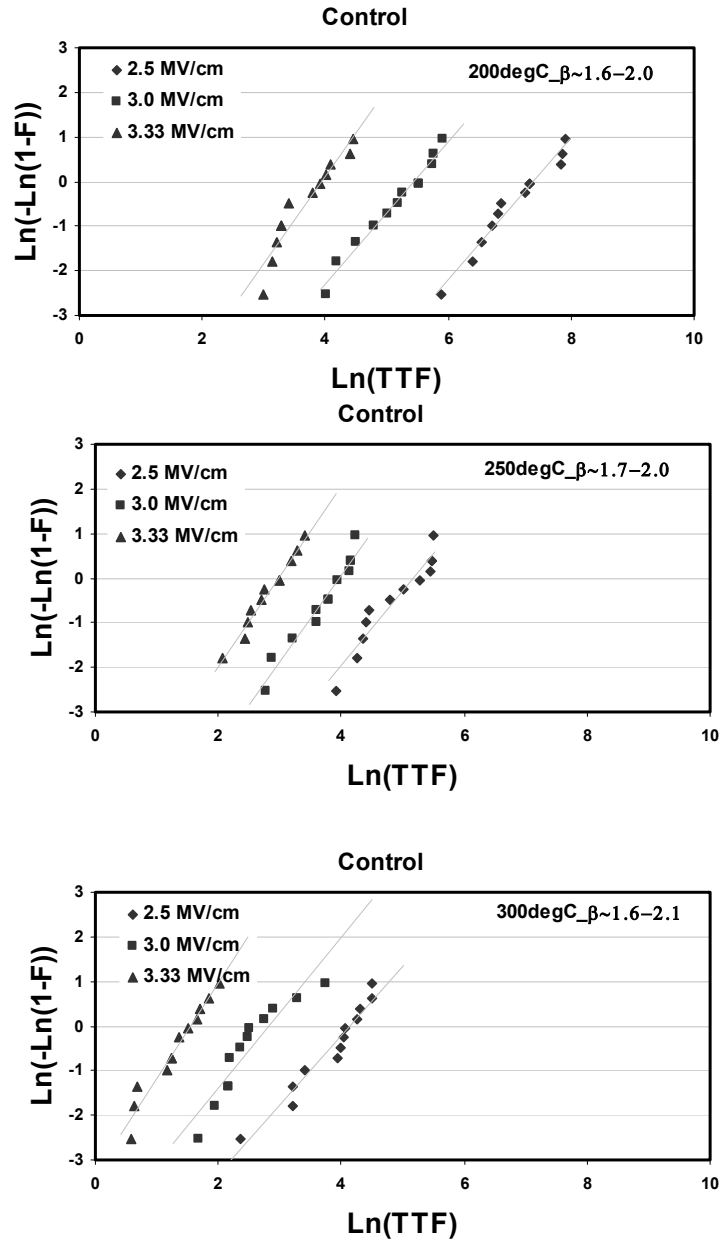


Figure 6.22 Weibull fits for the control sample at three temperatures shows that lifetimes decrease with increasing temperatures

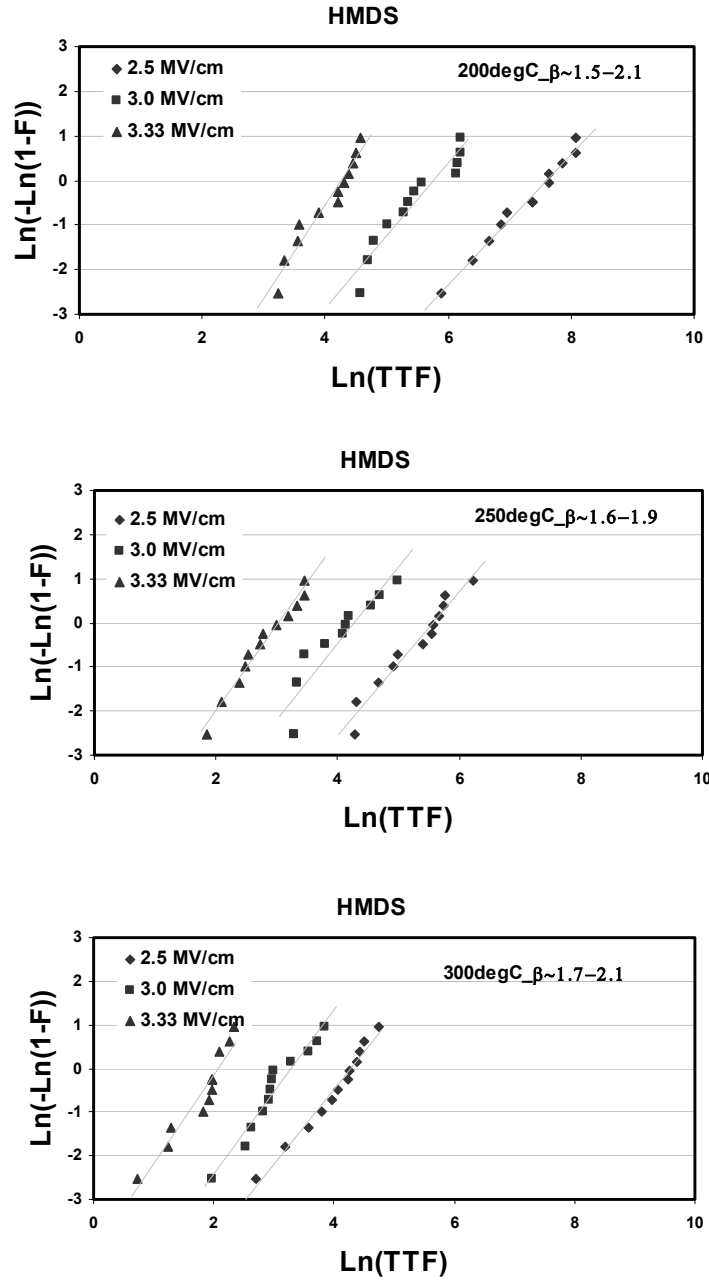


Figure 6.23 Weibull plots for the HMDS treated sample at three temperatures shows that lifetimes decrease with increasing temperatures

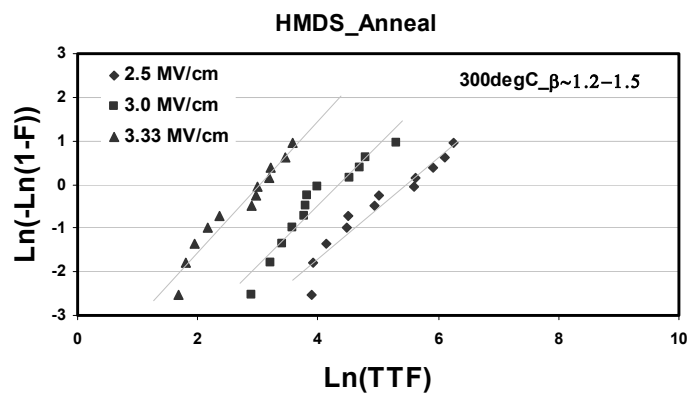
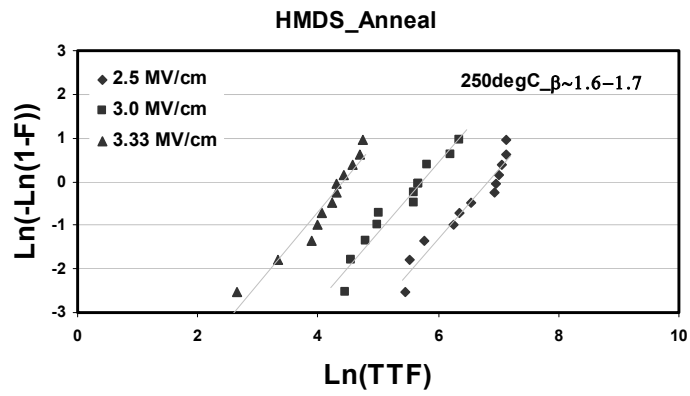
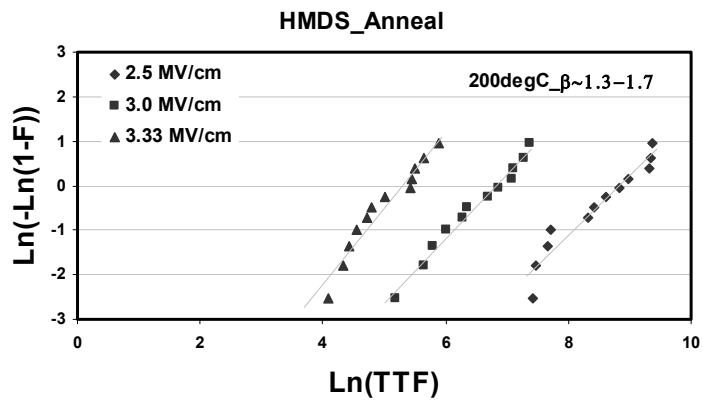


Figure 6.24 Weibull plots for the HMDS followed by an anneal sample for three temperatures shows that lifetimes decrease with increasing temperatures

The 63% Weibull lifetimes are extracted and plotted with respect to electric field to determine the field acceleration parameter at three different temperatures. The lifetimes are also plotted with respect to the inverse of temperature to determine the activation energies at three different fields. Table 6.3 summarizes the field acceleration parameters and activation energies for the three splits.

Split	Ea (ev)	Gamma
Control	0.56 - 0.78	2.9 - 4.0
HMDS	0.55 - 0.79	3.1 - 4.0
HMDS+Anneal	0.57 - 0.76	3.1 - 4.1

Table 6.3 Activation energies and field acceleration parameters for all three splits are similar, which shows that the breakdown mechanism is similar

The activation energies and field acceleration parameters are similar for the three splits. However, the lifetimes are higher by a factor of 4 to 6 times for the HMDS followed by an anneal treatment.

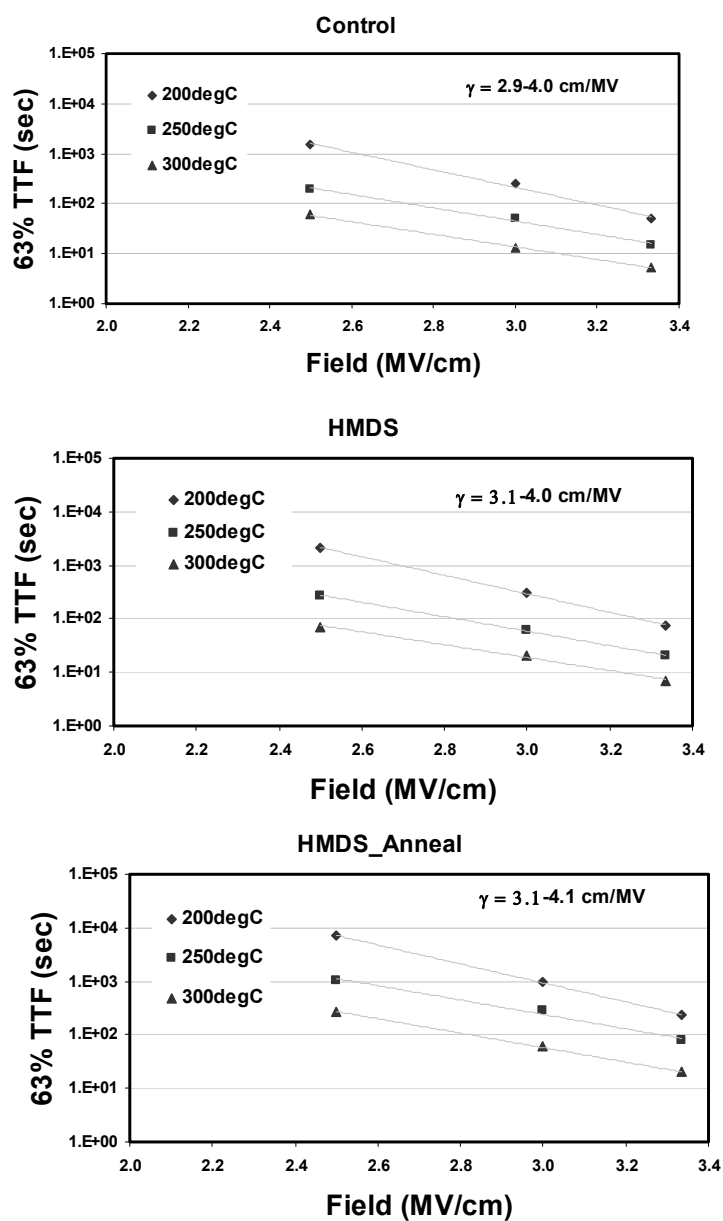


Figure 6.25 Lifetimes are plotted versus the electric field to obtain the field acceleration parameters

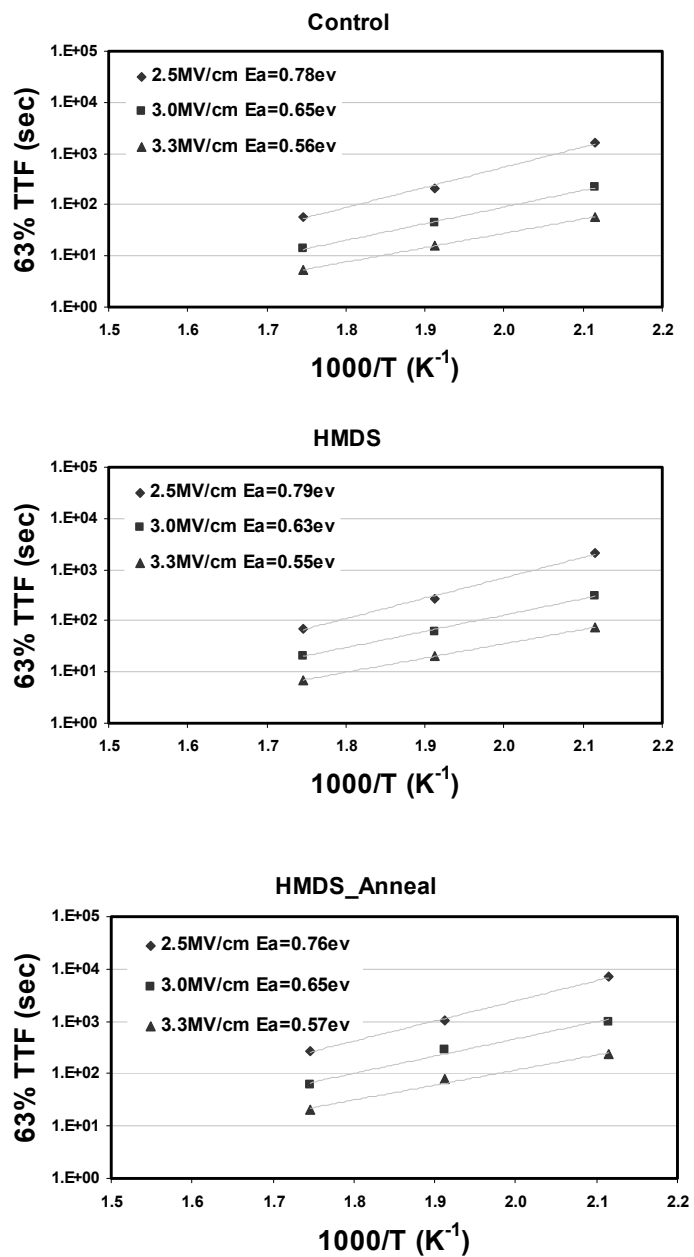


Figure 6.26 Lifetimes are plotted versus 1000/T to determine the activation energies of the three splits

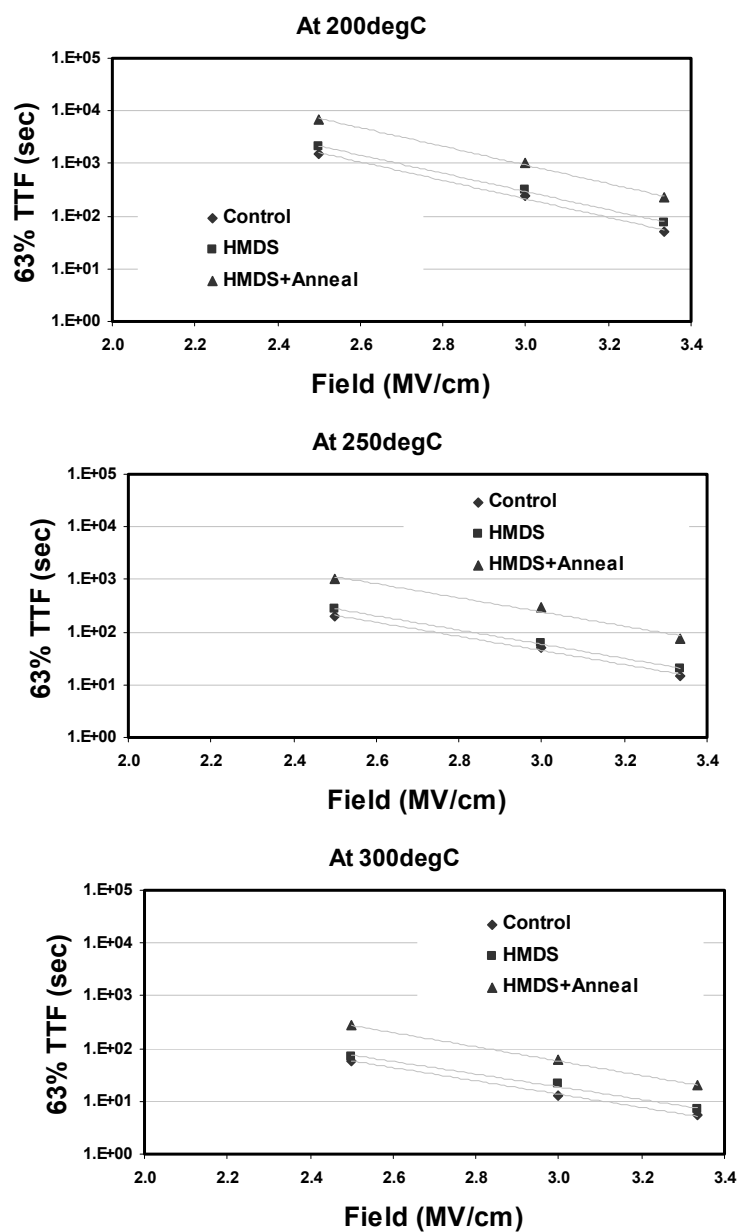


Figure 6.27 Lifetimes are compared among the three splits for all the three temperatures. The HMDS followed by an anneal treatment has higher lifetimes.

The activation energies are similar for all three splits. This implies that the breakdown mechanism is similar for all the three splits. The HMDS followed by an anneal treatment showed an improvement in breakdown field as well as lifetime even though the activation energy and the field acceleration parameters are similar. The reason for the improvement is believed to be due to the reduction in the initial defect density at the trench interface. An estimation of the defect density will be made in the next segment.

6.3.4 Estimation of Interfacial Defect Density

The control sample and the HMDS followed by an anneal sample were further subjected to TDDB tests to determine the improvement in defect density. These tests were performed at 70V at RT for three different comb/comb areas (0.005cm^2 , 0.001cm^2 and 0.0002cm^2).

The charge-to-breakdown (Qbd) was calculated from the current versus time plots and a Qbd value of 1.5 C/cm^2 was taken as a reliability criterion. The number of samples that had a Qbd greater or less than 1.5 C/cm^2 were determined. The yield fraction was then plotted with respect to the area. The data was fit to two distribution functions [Michalka (1990)]. The first one is a delta function that assumes that the defects are random and uniformly distributed. The second is an exponential function that assumes that the high defect densities are increasingly unlikely.

The yield equation for the Delta function is given by,

$$Y = Y_0 \text{Exp} (-DA).$$

And the yield for the exponential function is given by,

$$Y = Y_0 / [1 + DA].$$

Where, D is the defect density in defects/cm² and A is the area in cm².

Fig 6.28 and 6.29 shows the data fits for these two equations. The exponential function has better fit than the delta function. The analysis indicates that the HMDS treatment decreased the defect density by a factor of about 5. This reduction in the defect density is believed to enhance the lifetime of the Cu/low-κ structures.

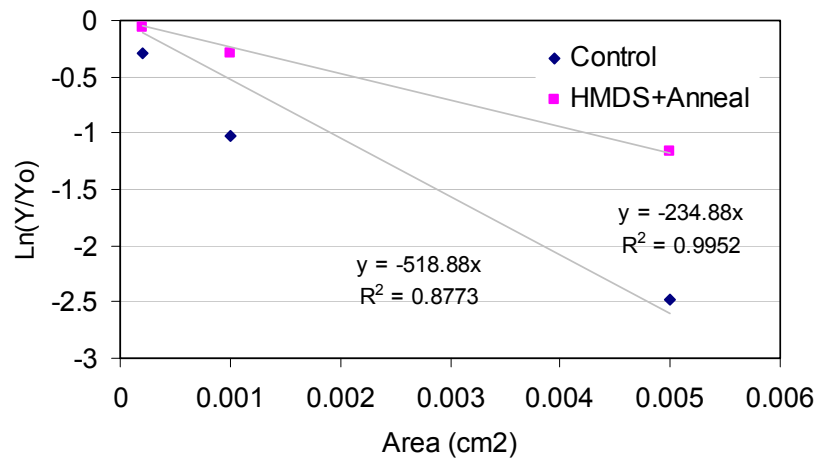


Figure 6.28 Delta function fit shows a poor fit for the control sample

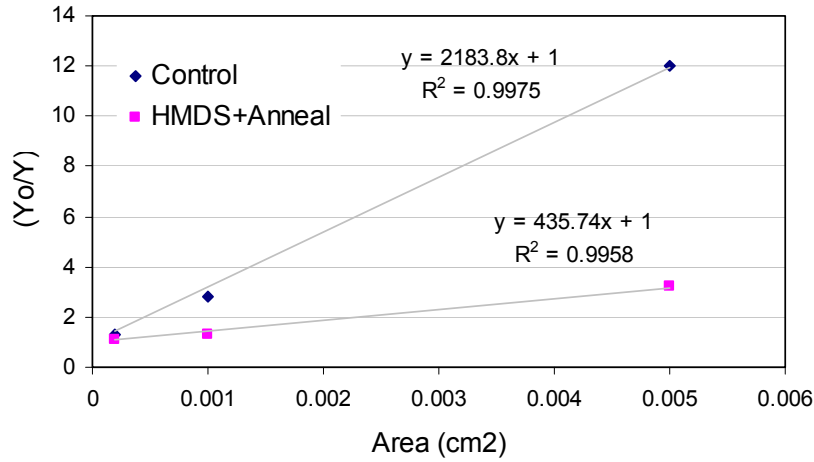


Figure 6.29 Exponential function fit shows a good fit for both samples and shows that the HMDS followed by an anneal treatment reduces the defect density by a factor of about 5

6.3.5 Analysis of the Charge-to-Breakdown

In the physical-damage theory of dielectric breakdown, the charge-to-breakdown (Qbd) is defined as the cumulative charge moving through a dielectric until failure occurs [Apte (1994)]. The dielectric degradation can be modeled on the basis of percolation theory. In this model, the dielectric will fail when there is a path of percolation from one end of the capacitor to the other end. The dielectric is divided into individual cells that are assumed to be “normal” or “defective”. It is assumed that defective cells allow an easy conduction path and are generated over time.

The dielectric will fail when a certain amount of charge creates a critical amount of defects, which will result in dielectric failure due to percolation. This charge is defined as the Qbd and it is related to the total cumulative charge passing through the dielectric until the time of failure. This charge-to-breakdown (Qbd) can be directly calculated from experimentally obtained current vs. time curves using the relation,

$$Qbd = \int_0^{tbd} Jdt$$

Although the time-to-fail (TTF) has an exponential dependence on the electric field, the charge-to-breakdown (Qbd) should be constant irrespective of the electric field. The current will be higher at high electric fields and if the Qbd is constant the TTF will be lower. As a result, the TTF can have an exponential dependence on electric field. The Qbd depends upon the initial state of the dielectric. If the dielectric already has defects then the Qbd will be less than that of a defect free dielectric, and this will give lower lifetimes. The final defect density at failure should be constant. Ultimately the dielectric fails when there is a path of percolation from one end to the other end.

A simple percolation model analysis can show that if there are already defects present at the interfaces, the number of additional defects required for percolation is much less. A Monte Carlo simulation was done to illustrate this point. A 10x10 grid of 2-d cells was taken to represent the dielectric. The percolation path was determined from one side to the other. An initial defect density was taken at the sidewalls for simulating etch and ash damage. The results are shown in Fig 6.31. From these results we see that the additional defect cells

required for percolation decreases for increasing initial defects. This implies that the dielectric with damage will have a lower lifetime compared to a sample that has been chemically treated to repair the damage.

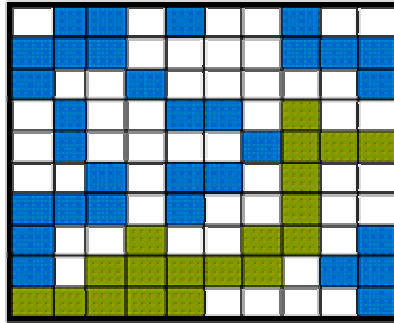


Figure 6.30 10x10 grid representing a trench dielectric with percolation from one side to the other

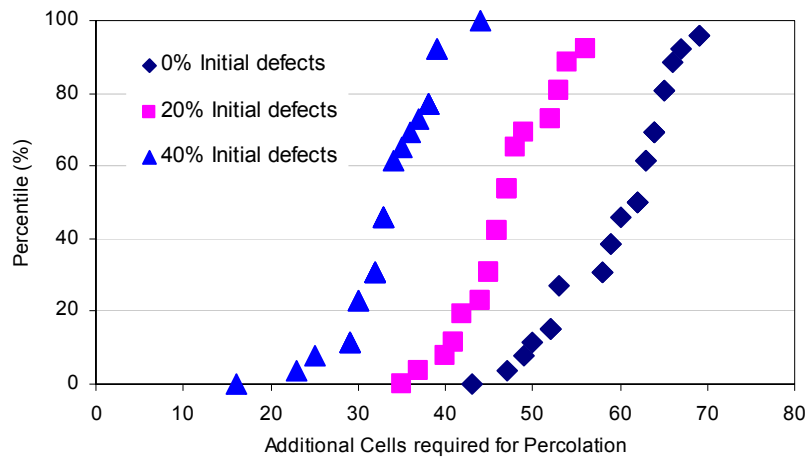


Figure 6.31 Distribution of the additional cells required for percolation shows that the additional cells required for percolation decreases with increasing initial defects

The etching and ashing processes create defects at the trench interfaces. Post ash treatments reduce the defect density and hence the Qbd of a post ash treated sample should be higher than an untreated sample. Fig 6.32 shows the Qbd versus the TTF.

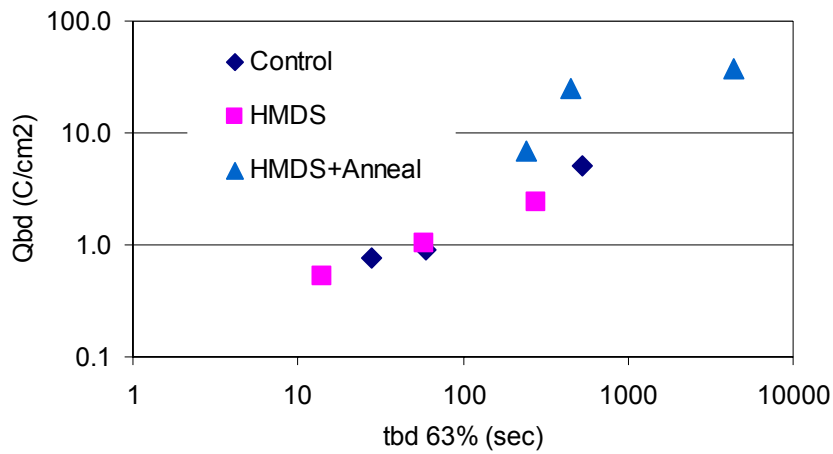


Figure 6.32 Qbd versus TTF for all three splits shows that the HMDS followed by an anneal treatment has higher lifetimes and higher Qbd

The Qbd is higher for the HMDS followed by an anneal post ash treatment. This is consistent with the observation that this treatment reduced the defect density by a factor of about 5. Fig 6.33 shows the Qbd and the TTF versus the electric field. Although the TTF has an exponential dependence on electric field, as it should, the Qbd is not constant at all electric fields.

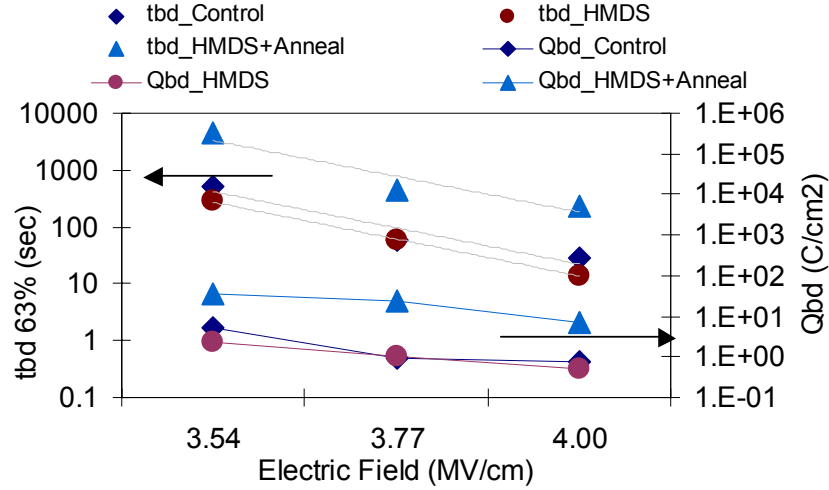


Figure 6.33 Qbd and TTF versus the electric field show that both Qbd and TTF decrease with increasing electric field but TTF has an exponential dependence whereas Qbd does not.

As the electric field is increased from 3.54MV/cm to 4.0MV/cm, the Qbd decreases by a factor of about 5 whereas the TTF decreases by a factor of 20. The increase in Qbd with decreasing electric field may indicate that at low fields there is a probability of a defect reverting back to its original state. As a result, at low fields it takes longer to accumulate the same amount of defect density for the dielectric to fail. It is also conceivable that the Qbd depends upon the leakage mechanism at the test conditions.

There is also the issue of field enhancement at the top interfacial corners due to protrusion of copper between the hard mask and the capping layer. Also other breakdown mechanisms may be occurring simultaneously with defect generation. Copper ionization at high fields is also a possibility, although at RT

conditions there is unlikely to be any ionic diffusion. Nevertheless, copper ionization can further weaken the interface and hasten the failure of the dielectric at a lower Qbd.

6.3.6 Failure Analysis

Failure analysis was performed on these wafers. Cross-sectional SEM micrographs were obtained for multiple failure sites for all temperatures. Fig 6.34 shows a typical failure site. All the analyzed failure sites exhibited similar characteristics. Delamination of the top interface between the low- κ and the capping layer is always observed. In many cases copper penetration into the trench dielectric is also observed.

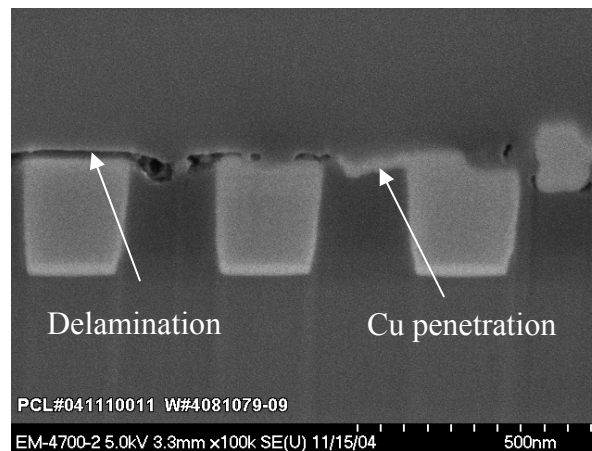


Figure 6.34 Cross-sectional SEM of TDDDB failure site show delamination and copper penetration at the interface

Failure analysis did not show any difference between the failure sites of the chemically treated or control samples. For the samples that were cross-sectioned, the failure analysis did not show breakdown inside the dielectric as percolation modeling would have predicted. It should be noted that time intervals of less than a second would have to be used to stop the test at the first hint of failure. The limitations of the instrument make it impossible to prevent secondary breakdown events occurring within a fraction of a second. Visible burn marks are generally observed on the lines. The inability to observe a percolation type of failure does not mean it is not the actual mechanism of failure.

Allers (2004) made a calculation of the energy of the capacitor and showed that the energy density ($\sim 2 \text{ J/m}^2$) between the fingers of the comb is very near to the typical adhesion energies ($\sim 4\text{-}12 \text{ J/m}^2$) of the top surfaces (SiN, SiCN, SiOx) to the low- κ material and copper.

A similar calculation can be made from the current just before failure. From the current versus time plots we can obtain the current before failure and calculate the charge in the capacitor just before failure. The energy can then be calculated by

$$E = Q V / 2$$

The calculated energy density is $3\text{-}9 \text{ J/m}^2$ for voltages ranging from 62V to 70V. The calculated value of the energy density just before failure is very close to the adhesion energies of the capping or hard mask materials (SiN, SiCN, SiOx) with the low- κ material and copper.

The observed failure regions are secondary effects caused by the initial breakdown of the dielectric. The energy released at the instant of failure is enough to cause delamination of the top interface. The observed copper penetration may be due to copper extrusion after the delamination.

A different measurement set-up will have to be used to determine the failure site before catastrophic failure occurs. One type of method is using liquid crystal to determine local hot spots [Burgess (1999)]. This technique could be used in interconnect dielectric failure. At the first sign of heating, the voltage could be turned off and the spot could be then analyzed by cross-sectional SEM. Although this method would not give a failure time, it can be used along with traditional reliability testing methods to determine the statistics as well as mechanism of dielectric failure.

6.3.7 Discussion

As line widths continue to shrink it is becoming increasingly important to reduce etching and ashing damage to the trench sidewalls. Post ash chemical treatments can be used to recover the κ value as well as improve the reliability of the Cu/low- κ structures. HMDS followed by an anneal treatment successfully reduced the capacitance, and as a result the effective k , by about 3%. Although this does not seem very significant, it will become more significant as κ values continue to be lowered. The leakage and breakdown characteristics are also improved by this treatment. The improvement in reliability lifetime is as much as a factor of 9 and the reduction in interfacial defect density is as much as a factor of 5.

The activation energies and field acceleration parameters are similar for both the treated and untreated structures. This indicates that the failure mechanism is similar for both cases. The dielectric failure occurs in a fraction of a second and it is not possible to prevent additional effects, like delamination and localized heating, from destroying the dielectric and the metal lines. The failure analysis shows that failure occurs at the top interface, which indicates that it is the weakest interface. Stronger adhesion between capping and hard mask materials with low- κ and copper may yield better reliability lifetimes. Liquid crystal failure analysis technique would give a clearer picture of the actual failure mechanism. Nevertheless, post ash chemical treatments are a useful process step that can not only improve the reliability of the Cu/low- κ structure but also help achieve the effective κ target.

Chapter 7: Conclusions and Suggestions for Future Work

The purpose of this study was to determine the conduction mechanism in different porous low- κ films, to analyze the effect of pore size and distribution on the reliability characteristics of porous low- κ blanket films and to evaluate and understand the correlation of compositional changes in the low- κ dielectric material, due to post-ash cleaning and chemical treatments, to the dielectric properties and reliability of Cu/low- κ damascene structures.

Different low- κ dielectric can have widely different conduction mechanism processes at different ranges of electric fields. The conduction mechanism must be considered when making a valid comparison of reliability lifetimes.

The pore-size and distribution of the low- κ dielectric determines the state of the interface. The leakage and conduction and subsequent reliability depend largely on the interface. Large pore sizes give higher interfacial roughness, which causes localized field enhancements and higher defect densities, which ultimately results in poor electrical performance. Etching and ashing can cause further damage to the interface. The gases and chemicals used in etching, ashing and cleaning can enter into the pores and poison the dielectric. Smaller pore-size can reduce these effects to an extent. Pore sealing is another way to protect the exposed interface of the porous dielectric.

Surface processing techniques, like etching and ashing, damage the trench dielectric interface. The hydroxyl concentration increases and carbon is depleted in the damaged dielectric. Annealing is useful in reducing the κ value and the

leakage to an extent. But annealing by itself, cannot remove the silanol bonds. A chemical treatment like HMDS vapor increases the carbon content and reduces the silanol content of the film. Thermo-chemical treatments can ameliorate the damage by recovering the κ value and reducing the leakage to an extent.

Post ash thermo-chemical treatments can be used to recover the κ value as well as improve the reliability of the Cu/low- κ structures. HMDS followed by an anneal treatment successfully reduces the capacitance, and as a result the effective k , by about 3%. Although this does not seem very significant, it will become more significant as κ values continue to be lowered. The leakage and breakdown characteristics also improve by this treatment. The reliability lifetime is improved by a factor of about 9 and the interfacial defect density is reduced by a factor of 5. Post ash chemical treatments are a useful process step that can improve the reliability of the Cu/low- κ structure and also help in achieving the effective κ target.

Future work should investigate the effect of pore sealants on the dielectric reliability. Pore sealing could reduce the deleterious effects of etching and ashing and decrease the defect density and hence improve the reliability of the Cu/low- κ structures. Future work should also investigate capping and hard-mask materials. The top interface between the capping layer and the copper and low- κ is generally weak. Chemical and thermal treatments before capping may improve the dielectric reliability of the Cu/low- κ structures.

References

- Alers, G.B.; Jow, K.; Shaviv, R.; Kooi, G.; IEEE Transactions on Device and Materials Reliability, vol.4, no.2, p. 148-52, (2004).
- Allers, K.H.; Microelectronics Reliability, vol.44, no.3, p. 411-23, (2004).
- Apte, P.P.; Saraswat, K.C.; IEEE Transactions on Electron Devices, vol.41, no.9, p. 1595-602, (1994).
- Av-Ron, M.; Shatzkes, M.; DiStefano, T.H.; Gdula, R.A.; Journal of Applied Physics, vol.52, no.4, p. 2897-908, (1981).
- Azrak R. G. and Angell C. L.; J. Phys. Chem., vol. 77, pp. 3048-3052, (1973)
- Bashara, N.; IEEE Transactions on Component Parts, Vol. 11, Issue 1, p.4-9, (1964).
- Biberger, M.A., Schilling, P., Frye, D., & Mills, M.E., Semiconductor Fabtech, 12, 239-243, (2000).
- Blatt, Frank J. "Physics of electronic conduction in solids"; New York, (1968).
- Bozano, L.; Carter, S.A.; Scott, J.C.; Malliaras, G.G.; Applied Physics Letters, vol.74, no.8, p. 1132-4, (1999).
- Brar, B.; Wilk, G.D.; Seabaugh, A.C.; Applied Physics Letters, vol.69, no.18, p. 2728-30, (1996).
- Braun, Alexander E., "Dielectric Etch Looks for Processing, Metrology Solutions".Semiconductor International, (2002).
- Burgess, D.; Test & Measurement World, vol.19, no.15, p. 53-4, 56, 58, (1999).
- Carbone, M.; Larsson, K.; Journal of Physics: Condensed Matter, vol.17, no.8, p. 1289-300, (2005).
- Chen, I.C.; Holland, S.; Hu, C.; 23rd Proceedings of the International Reliability Physics Symposium p. 24-31, (1985).
- Chen, I.C.; Choi, J.Y.; Chan, T.Y.; Ong, T.C.; 26th Proceedings of the International Reliability Physics, p. 1-7, (1988).

- Chiu-Chih Chiang; I-Hsiu Ko; Mao-Chieh Chen; Zhen-Cheng Wu; In: Proceedings of the IEEE 2003 International Interconnect Technology Conference, IEEE, p. 201-3, (2003).
- Chiu-Chih Chiang; I-Hsiu Ko; Mao-Chieh Chen; Zhen-Cheng Wu; Journal of the Electrochemical Society, vol.151, no.9, p. G606-11, (2004).
- Cho, A.T.; Tsai, T.G.; Yang, C.M.; Chao, K.J.; Electrochemical and Solid-State Letters, vol.4, no.4, p. G35-8, (2001).
- Clark P. G., Schwab B. D. and Butterbaugh J. W., Martinez H. J. and Wolf P. J., "Cleaning and Restoring κ Value of Porous MSQ Films", Semiconductor International, (2003)
- Colburn, M.; Nitta, S.; Zinter, J.; Chakrapani, N.; In: Advanced Metallization Conference, Mater. Res. Soc, 2004. p. 489-93,(2003).
- Degraeve, R.; Groeseneken, G.; Bellens, R.; Ogier, J.L.; IEEE Transactions on Electron Devices, vol.45, no.4, p. 904-11, (1998).
- Fink D. and Christiansen D. ed., *Electronics Engineers' Handbook*, New York, McGraw-Hill, (1989)
- Gao, T.; Gray, W.D.; Van Hove, M.; Rosseel, E.; In: Proceedings of the IEEE International Interconnect Technology Conference, IEEE, p. 53-5, (1999).
- Grill, A.; Neumayer, D.A.; Journal of Applied Physics, vol.94, no.10, p. 6697-707, (2003).
- Grinberg A. A.; Luryi S.; Pinto M.; and Schryer N. L.; IEEE Transactions on Electron Devices, Vol. 36, No. 6, p. 1162-1170, (1989).
- Grubb W. T.; J. Amer. Chem. Soc., vol. 76, pp 3408-3414, (1954)
- Hamann, Claus; "Electrical conduction mechanisms in solids." Berlin (1988).
- Hare, R.W.; Hill, R.M.; Journal of Physics D (Applied Physics), vol.24, no.3, p. 398-406, (1991).
- Helms C. R. and Poindexter E. H., Reports on Progress in Physics, Vol. 57, No. 8, (1994).

- Hsiao-Show Tseng; Purtell, R.; Rothman, L.; Processing of Advanced Materials, vol.4, no.4, p. 197-202, (1994).
- Hu J. R., Uesato W., Schoenborn P., Clark P., Boumerzoug M. and Xu H.; AVS First International Conference on Microelectronics and Interfaces, (2000).
- Iacopi, F.; Travaly, Y.; Stucchi, M.; Struyf, H.; Materials Research Society Symposium Vol.812, Materials Research Soc, 2004. p.19-24, (2004).
- Jow, K.; Alers, G.B.; Sangneria, M.; Harm, G.; In: IEEE International Reliability Physics Symposium Proceedings 41st Annual, IEEE, 2003. p.598-9, (2003).
- Kaatze, U.; Uhlendorf, V.; Zeitschrift fur Physikalische Chemie. Neue Folge, vol.126, no.2, p. 151-65, (1981).
- Kao, Kwan-Chi, "Electrical transport in solids: with particular reference to organic semiconductors", Oxford, (1979).
- Keiss H.; Rehwald W.; Colloid & Polymer Science, Vol. 258, No.3, p. 241-251, (1980).
- Kondoh, E.; Baklanov, M.R.; Bender, H.; Maex, K.; Electrochemical and Solid-State Letters, vol.1, no.5, p. 224-6, (1998).
- Korn M., Killmann E., Eisenlauer J.; Journal of Colloid and Interface Science, Vol 76, Issue 1, p 7-31, (1980)
- Krieger, G.; Swanson, R.M.; Journal of Applied Physics, vol.52, no.9, p. 5710-17, (1981).
- Lamy, S.; Louveau, O.; Fanget, G.; Fayolle, M.; In: Proceedings of the IEEE International Interconnect Technology, IEEE, 2002. p.30-2, (2002).
- Lee, J.C.; Chen Ih-Chin; Hu Chenming; IEEE Transactions on Electron Devices, vol.35, no.12, p. 2268-78. (1988).
- Lee S.; Moosung Chae; Heondo Kim; Taekyung Kim; In: Proceedings of the IEEE International Interconnect Technology Conference, IEEE, p. 137-9, (2000).
- Lenzlinger, M.; Snow, E.H.; Journal of Applied Physics, vol.40, no.1, p.278-83, (1969).

- Lin, S.; Changming Jin; Lui, L.; Minghsing Tsai; In: Proceedings of the IEEE International Interconnect Technology, IEEE, p. 146-8, (2001).
- Liu P.; Chang, T.C.; Mor, Y.S.; Chen, C.W.; Electrochemical and Solid-State Letters, vol.5, no.3, p. G11-14, (2002).
- Loke, A.L.S.; Wetzel, J.T.; Stankus, J.J.; Angyal, M.S.; IEEE Electron Device Letters, vol.19, no.6, p. 177-9, (1998).
- Lu X., Qianer Zhang and M. C. Lin, Phys. Chem. Chem. Phys., 3(11), 2156, (2001)
- Mabboux Pierre-Yves and Gleason Karen K., J. Electrochem. Soc. 152, F7 (2005)
- Martin, S.J.; Godschalx, J.P.; Mills, M.E.; Shaffer, E.O., II.; Advanced Materials, vol.12, no.23, p. 1769-78, (2000).
- McPherson, J.; Reddy, V.; Banerjee, K.; Huy Le; In: International Electron Devices Meeting, IEEE, p. 171-4, (1998).
- McPherson, J.W.; International Journal of High Speed Electronics and Systems, vol.11, no.3, p. 751-87, (2001).
- McPherson, J.; Kim, J.-Y.; Shanware, A.; Mogul, H.; Applied Physics Letters, vol.82, no.13, p. 2121-3, (2003).
- McPherson, J.W.; Journal of Applied Physics, vol.95, no.12, p. 8101-9, (2004).
- Michalka, T.L.; Varshney, R.C.; Meindl, J.D.; IEEE Transactions on Semiconductor Manufacturing, vol.3, no.3, p. 116-27, (1990).
- Mor, Y.S.; Chang, T.C.; Liu, P.T.; Tsai, T.M.; Journal of Vacuum Science & Technology B (Microelectronics and Nanometer Structures), vol.20, no.4, p. 1334-8, (2002).
- Mosig, K.; Jacobs, T.; Kofron, P.; Daniels, M.; In: Proceedings of the IEEE International Interconnect Technology Conference, IEEE, p. 292-4, (2001).
- Nagano, S.; Tsukiji, M.; Ando, K.; Hasegawa, E.; Journal of Applied Physics, vol.75, no.7, p. 3530-5, (1994).

- Nakamura, N.; Higashi, K.; Matsunaga, N.; Miyajima, H.; 7th International Symposium on Plasma- and Process-Induced Damage, American Vacuum Soc, p. 162-5, (2002).
- Nguyen T., Byrd E., Bentz .; Journal of Adhesion, Vol. 48, p 169-194, (1995).
- Noguchi, J.; Ohashi, N.; Jimbo, T.; Yamaguchi, H.; IEEE Transactions on Electron Devices, vol.48, no.7, p. 1340-5, (2001).
- Noguchi, J.; Saito, T.; Ohashi, N.; Ashihara, H.; In: IEEE International Reliability Physics Symposium Proceedings. 39th, IEEE, p.355-9, (2001).
- O'Dwyer, John J. "The theory of electrical conduction and breakdown in solid dielectrics". Oxford (1973).
- Ogawa, E.T.; Jinyoung Kim; Haase, G.S.; Mogul, H.C.; In: 2003 IEEE International Reliability Physics Symposium Proceedings 41st Annual, IEEE, p. 166-72, (2003).
- Peters L., "Low- κ Drives New Stripping Solutions", Semiconductor International, (2002).
- Purtell, R.; Rothman, L.; Eldridge, B.; Chess, C.; Journal of Vacuum Science & Technology A (Vacuum, Surfaces, and Films), vol.11, no.4, pt.2, p. 1696-701, (1993)
- Reiser, A.; Lock, M.W.B.; Knight, J.; Transactions of the Faraday Society, vol.65, pt.8, p. 2168-85, (1969).
- Rose A.; Physical Review, Vol. 97, No. 6, p.1538-1544, (1955).
- Schuegraf, K.F.; Chenming Hu; Semiconductor Science and Technology, vol.9, no.5, p. 989-1004, (1994).
- Schuegraf, K.F.; Chenming Hu; IEEE Transactions on Electron Devices, vol.41, no.5, p. 761-7, (1994).
- Shi, J.; Rounds, S.; Noble, T.; DeSarno, M.; Inter. Symp. on Plasma Process-Induced Damage, American Vacuum Soc, p. 124-6, (1996).
- Silvestrelli, P.L.; Surface Science, vol.552, no.1-3, p. 17-26, (2004).
- Simmons J. G.; Physical Review, vol. 155, No. 3, pp 657-660, (1967).

- Solis, R.; Harvey, I.R.; Gabriel, C.T.; IEEE Int. Symp. on Semiconductor Manufacturing Conference Proceedings, IEEE, p. F25-8, (1997).
- Sprung M. M.; Guenther F. O.; J. Organic Chemistry, vol. 26, pp. 552-557, (1961).
- Strittmatter, R.J.; Niu, Q.J.; Waeterloos, J.; Meyers, G.F.; Advanced Metallization Conference, Mater. Res. Soc, p. 159-63, (2004).
- Sze S. M., Physics of Semiconductor Devices, 2nd edition, New York, Wiley, (1981).
- Tada, M.; Harada, Y.; Ohtake, H.; Saito, S.; In: Proceedings of the International Interconnect Technology Conference, IEEE, p. 256-8, (2003).
- Tanaka, H.; Uchida, H.; Ajioka, T.; Hirashita, N.; IEEE Transactions on Electron Devices, vol.40, no.12, p. 2231-6. (1993).
- Tsai, M.H.; Tsai, W.J.; Shue, S.L.; Yu, C.H.; In: Proceedings of the International Interconnect Technology Conference, IEEE, p. 214-16, (2000).
- Weinberg, Z.A.; Hartstein, A.; Solid State Communications, vol.20, no.3, p. 179-82, (1976).
- Weinberg, Z.A.; Solid-State Electronics, vol.20, no.1, p. 11-18, (1977).
- Weinberg, Z.A.; Journal of Applied Physics, vol.53, no.7, p. 5052-6, (1982).
- Wu W.; Xiaodong Duan; Yuan, J.S.; In: IEEE International Reliability Physics Symposium Proceedings 41st Annual, IEEE, p. 282-6, (2003).
- Wu, Z.C.; Chiang, C.C.; Wu, W.H.; Chen, M.C.; Proc. of the Int Interconnect Technology Conference, IEEE, p. 42-4, (2001).
- Xie B.; Muscat, A.J.; IEEE Transactions on Semiconductor Manufacturing, vol.17, no.4, p. 544-53, (2004).
- Yiang, K.Y.; Yoo, W.J.; Guo, Q.; Krishnamoorthy, A.; Applied Physics Letters, vol.83, no.3, p. 524-6, (2003).
- Zeller, H.R.; IEEE Transactions on Electrical Insulation, vol.EI-22, no.2, p. 115-22, (1987).

Vita

Swarnal Borthakur was born on January 31st, 1976 in Jorhat, India. He is the second son of Mr. Tarun Borthakur and Mrs. Gitanjali Borthakur. He completed his high school from Don Bosco High School and junior college from Cotton College in Guwahati. He then joined the Regional Engineering College in Nagpur and graduated with an undergraduate degree in Metallurgical Engineering (B.E) in 1999. In the fall of the same year, he joined The University of Texas at Austin as a graduate student in Materials Science and Engineering. He graduated with a Master of Science in Engineering (M.S.E) degree in 2001. He then entered the doctoral program in Materials Science and Engineering.

Permanent Address: C/O Mr. Tarun Borthakur, House No. 3, Senduri Ali, Guwahati, Assam, India -781007.

This dissertation was typed by the author.